

**TECHNISCHE
UNIVERSITÄT
DRESDEN**

Preparation and Characterization of Nanoscopic Solid State Hydrogen Storage Materials

Dissertation
zur Erlangung des wissenschaftlichen Grades
Doctor rerum naturalium
(Dr. rer. nat.)

vorgelegt
der Fakultät Mathematik und Naturwissenschaften
der Technischen Universität Dresden

von
Dipl.-Phys. Alexander Surrey
geboren am 02.12.1986 in Gießen

Matrikelnummer:	3212347
Verantwortlicher Hochschullehrer:	Prof. Dr. Ludwig Schultz
2. Gutachter:	Prof. Dr. Oliver Gutfleisch
Eingereicht am:	25.07.2016
Verteidigt am:	30.09.2016

Kurzfassung

Die Speicherung von Wasserstoff in Form von Hydriden im festen Aggregatzustand hat den Vorteil einer hohen volumetrischen und gravimetrischen Wasserstoffspeicherdichte, die sowohl für die stationäre als auch die mobile Anwendung nötig ist. Um die Anforderungen dieser Anwendungen erfüllen zu können, müssen die Speichereigenschaften dieser Materialien weiter verbessert werden. Als zentrales Konzept dieser Dissertation wird die Nanostrukturierung verfolgt, die eine vielversprechende Strategie zur Modifizierung der thermodynamischen und kinetischen Eigenschaften von Hydriden darstellt. Die Transmissionselektronenmikroskopie (TEM) stellt dabei eine unverzichtbare Untersuchungsmethode solcher nanoskopischer Materialien dar. Als problematisch erweist sich dabei die durch Radiolyse hervorgerufene Zersetzung der meisten Hydride bei der Beleuchtung mit dem abbildenden Elektronenstrahl.

Im ersten Teil dieser Arbeit wird eine Methodik entwickelt um dieses Phänomen quantitativ mit Hilfe von Valenzelektronenenergieverlustspektroskopie zu untersuchen. Hierzu kommt kugelmahlendes MgH_2 als Modellsystem zum Einsatz. Die Dehydrierung kann quantitativ durch die inelastische Streuung der hochenergetischen Elektronen am MgH_2 -Plasmon erklärt werden. Eine Lösung dieses grundlegenden Problems wird theoretisch an Hand von Multislice TEM-Kontrastsimulationen untersucht. Hierbei wird ein TEM-Experiment unter Wasserstoff bei Umgebungsdruck anstatt unter Vakuum simuliert, was mit Hilfe eines speziellen TEM Halters, in dem das Gas durch elektronentransparente Fenster eingeschlossen ist, realisiert werden kann.

Im zweiten Teil wird der Einfluss des Nanoconfinements (Nanoeinschließung), einer speziellen Form der Nanostrukturierung, des komplexen Hydrids LiBH_4 auf dessen Wasserstoffspeichereigenschaften untersucht, wofür eine neuartige nanoporöse aerogel-ähnliche Kohlenstoff-Gerüststruktur zum Einsatz kommt. Diese wird durch Salt Templating synthetisiert – einer simplen und nachhaltigen Methode zur Herstellung nanoporöser kohlenstoffbasierter Materialien mit großen Porenvolumina. Es wird gezeigt, dass durch das Nanoconfinement die Wasserstoffdesorptionstemperatur, die für makroskopisches LiBH_4 bei über 400 °C liegt, auf 310 °C sinkt und die Desorption bereits bei 200 °C einsetzt. Eine teilweise Rehydrierung ist unter moderaten Bedingungen (100 bar und 300 °C) möglich, wobei die Reversibilität durch eine partielle Oxidation des amorphen Bor gehemmt ist. Im Gegensatz zu Beobachtungen einer aktuellen Veröffentlichung von in hoch geordnetem, nanoporösen Kohlenstoff eingebetteten LiBH_4 deuten die in-situ TEM-Heizexperimente der vorliegenden Arbeit darauf hin, dass beide Reaktionsprodukte (B und LiH) in den Poren des aerogel-ähnlichen Kohlenstoffs verbleiben.

Abstract

Storing hydrogen in solid hydrides has the advantage of high volumetric and gravimetric hydrogen densities, which are needed for both stationary and mobile applications. However, the hydrogen storage properties of these materials must be further improved in order to meet the requirements of these applications. Nanostructuring, which represents one of the central approaches of this thesis, is a promising strategy to tailor the thermodynamic and kinetic properties of hydrides. Transmission electron microscopy (TEM) is an indispensable tool for the structural characterization of such nanosized materials, however, most hydrides degrade fast upon irradiation with the imaging electron beam due to radiolysis.

In the first part of this work, a methodology is developed to quantitatively investigate this phenomenon using valence electron energy loss spectroscopy on ball milled MgH_2 as a model system. The dehydrogenation can be quantitatively explained by the inelastic scattering of the incident high energy electrons by the MgH_2 plasmon. A solution to this fundamental problem is theoretically studied by virtue of multislice TEM contrast simulations of a windowed environmental TEM experiment, which allows for performing the TEM analysis in hydrogen at ambient pressure rather than vacuum.

In the second part, the effect of the nanoconfinement of the complex hydride LiBH_4 on its hydrogen storage properties is investigated. For this, a novel nanoporous aerogel-like carbon scaffold is used, which is synthesized by salt templating – a facile and sustainable technique for the production of nanoporous carbon-based materials with large pore volumes. It is shown that the hydrogen desorption temperature, which is above 400 °C for bulk LiBH_4 , is reduced to 310 °C upon this nanoconfinement with an onset temperature as low as 200 °C. Partial rehydrogenation can be achieved under moderate conditions (100 bar and 300 °C), whereby the reversibility is hindered by the partial oxidation of amorphous boron. In contrast to recent reports on LiBH_4 nanoconfined in highly ordered nanoporous carbon, in-situ heating in the TEM indicates that both decomposition products (B and LiH) remain within the pores of the aerogel-like carbon.

Contents

List of Figures	vii
1. Introduction	1
2. Fundamentals	5
2.1. Solid state hydrogen storage	5
2.2. Thermodynamics	7
2.3. Magnesiumhydride, MgH ₂	9
2.4. Lithiumborohydride, LiBH ₄	10
2.5. Nanoconfinement	12
2.5.1. Nanoconfinement of MgH ₂	13
2.5.2. Nanoconfinement of LiBH ₄	15
2.6. Radiation damage of hydrides in the TEM	17
3. Theoretical and Experimental Methods	19
3.1. Ball milling	19
3.2. X-ray diffraction analysis	19
3.3. Thermal Characterization	20
3.3.1. Differential Scanning Calorimetry	20
3.3.2. Coupled Thermogravimetry and Mass Spectroscopy	21
3.4. Melt infiltration of LiBH ₄	21
3.5. Solid State Nuclear Magnetic Resonance	21
3.6. Transmission Electron Microscopy	23
3.6.1. In-situ TEM Heating	25
3.6.2. Environmental TEM	26
3.6.3. Electron Energy Loss Spectroscopy	28
3.6.4. Multislice Simulations	33
4. Electron Beam induced Dehydrogenation of MgH₂	39
4.1. Microscopic Model of Hydrogen Release	39

4.2.	Determination of Characteristic Electron Doses	40
4.3.	Beam Damage Mechanism	43
4.4.	Thickness Dependence of the Electron Dose	44
4.5.	Conclusions for the Electron Beam Induced Dehydrogenation	48
4.6.	Multislice Simulations for ETEM Studies	48
4.6.1.	Methods of the Multislice Simulations	49
4.6.2.	Results and Discussion of the Multislice Simulations	51
4.6.3.	Conclusions of the Multislice Simulations	55
5.	Nanoconfinement of LiBH₄ in Aerogel-Like Carbon	57
5.1.	Nanoporous Carbon Scaffolds	57
5.2.	DSC Analysis of Melt Infiltration	59
5.3.	XRD Analysis	60
5.4.	Thermogravimetry and Mass Spectrometry Analysis	61
5.4.1.	Hydrogen Desorption Properties of Nanoconfined LiBH ₄	61
5.4.2.	Rehydrogenation of Nanoconfined LiBH ₄	64
5.5.	In-situ STEM Analysis	64
5.6.	Solid State ¹¹ B NMR	68
6.	Conclusions	71
A.	Appendix	73
A.1.	Derivation of the Fourier-Log Deconvolution	73
A.2.	Derivation of Equation 4.2	75
	Bibliography	77

List of Figures

2.1. Hydrogen storage densities	6
2.2. Stability of hydrides vs. hydrogen density	9
3.1. Debye-Scherrer geometry	20
3.2. FEI Titan ³ 80-300	24
3.3. TEM heating holder.	26
3.4. Design of a windowed environmental cell TEM holder.	28
3.5. Monochromated zero loss peaks.	33
4.1. TEM image of dehydrogenated MgH ₂ particle and VEEL spectra.	40
4.2. Decay of MgH ₂ plasmon.	42
4.3. Electron doses	42
4.4. Interrupted dehydrogenation.	44
4.5. Raw and deconvolved VEEL spectrum of MgH ₂	46
4.6. Modeled supercell of the nanoreactor	50
4.7. Simulated Mg nanocrystal inside the nanoreactor.	52
4.8. Contrast map of Mg inside the nanoreactor	53
4.9. Simulated HRTEM contrast of free Mg and Mg inside the nanoreactor.	53
4.10. Simulated MgH ₂ nanocrystal inside the nanoreactor.	54
4.11. Contrast of MgH ₂ inside the nanoreactor depending on thickness	54
4.12. Contrast of Mg in nanoreactor depending on pressure.	55
5.1. Salt templating	59
5.2. DSC curve of meltinfiltration of LiBH ₄	60
5.3. XRD analysis of nanoconfined LiBH ₄	61
5.4. Thermogravimetry and mass spectrometry of nanoconfined LiBH ₄	62
5.5. Elemental maps of nanoconfined LiBH ₄	65
5.6. In-situ TEM heating of nanoconfined LiBH ₄	66
5.7. ADF STEM image at 400 °C and particle size distribution.	67
5.8. NMR analysis of nanoconfined LiBH ₄	69

1. Introduction

The world's energy supply heavily relies on fossil fuels such as oil, gas and coal, which are needed for electricity, heat and mobility. However, converting the stored chemical energy into the latter forms requires burning those resources, which releases the greenhouse gas CO₂. Over the last 100 years, this has led to the anthropogenic global warming and will continue to change the climate. If one does not want to risk a climate catastrophe, the burning of fossil fuels should stop immediately. Another drawback of fossil fuels is simply that their deposits are finite. The next and successive generations will not have easy access to these resources anymore. Mainly because of these two reasons there is an urgent need to replace fossil fuels by an environmentally friendly energy carrier in order to maintain the standard of living or even improve it in developing and emerging countries.

Hydrogen produced from renewable energies has the potential to become this carrier. It can be produced by electrolysis and can be burned either in fuel cells, in future hydrogen turbines or modified petrol engines to make use of the stored energy for electricity, heat or mobility. The lack of a safe, efficient and economical storage of hydrogen remains the main obstacle impeding a future hydrogen economy [Jia et al., 2015]. Especially for hydrogen-powered vehicles the storage is challenging, because hydrogen as the lightest of all gases has a too small volumetric energy density. The most mature technology for hydrogen storage is the compression to 700 bar to increase this density. For this compression, however, already 15% of the energy stored in the hydrogen is needed [Felderhoff et al., 2007]. Furthermore, such high hydrogen pressures have safety concerns. An alternative way of hydrogen storage is the chemical binding of hydrogen in solid hydrides, thereby increasing the volumetric energy density to values above that of compressed or even liquified hydrogen, which is especially promising for hydrogen-powered vehicles. Hydrogen can be released from a hydride by heating it above its decomposition temperature. Ideally, readily available waste heat, e.g. from the fuel cells, are used for this heating. This scenario specifies the decomposition temperature of the hydride, which should be below the operating temperature of a proton exchange membrane (PEM) fuel cell. This type of fuel cell is typically used in vehicles and has an operating temperature of roughly 100 °C at a hydrogen pressure of approximately 1 bar. For stationary applications, where waste heat is available at higher temperature,

a higher decomposition temperature is in principle also acceptable. Here, the gravimetric hydrogen density is less important, while it is a very critical parameter for mobile applications. For this, the gravimetric hydrogen density of a hydride should be at least 6 wt.% to be compatible with compressed hydrogen [Felderhoff et al., 2007]. The ultimate goal for a wide spread commercialization and for being compatible with conventional combustion engines is set to 10 wt.% by the US Department of Energy (DOE) [Stetson, 2012]. These two constrains, decomposition temperature and hydrogen density, mainly hinder the practical application of hydrides for on-board hydrogen storage so far, because no known material can fulfill both at the same time. While interstitial metal hydrides such as LaNi_5H_6 can desorb hydrogen below 100 °C, they have a far too low gravimetric density. Ionic hydrides such as MgH_2 or complex hydrides such as LiBH_4 , on the other side, offer high densities of 7.6 wt.% or even 18.5 wt.%, respectively, but they suffer from too high thermodynamic stabilities and sluggish reaction kinetics requiring too high decomposition temperatures of more than 350 °C. Such high temperatures are unwanted on-board a vehicle, both from a practical and from an energy-efficiency point of view [de Jongh and Adelhelm, 2010]. Apart from that, further problems exist with many materials that have to be overcome. E.g., the hydrogen desorption has to be reversible at moderate hydrogen pressure (below ≈ 100 bar) and it needs to take place fast to allow for acceptable refueling times.

Therefore, new strategies have been explored to tailor the hydrogen storage properties of hydride materials in the last decades. The discovery of the catalytic activity of Ti compounds for the hydrogen sorption properties of NaAlH_4 making the dehydrogenation reversible under moderate conditions [Bogdanovic et al., 2000] has raised the interest also in other complex hydrides. Other approaches are the synthesis of a complex double-cation borohydride $\text{Al}_3\text{Li}_4(\text{BH}_4)_{13}$ [Lindemann et al., 2010] or mixtures of metal borohydrides such as $\text{LiBH}_4\text{-Mg}(\text{BH}_4)_2$ [Bardají et al., 2011]. Another strategy is the nanostructuring of hydrides. A change of thermodynamic properties of hydrides at the nanoscale has first been reported for the Pd-H system by Eastman et al. [1993]. The first proof-of-concept and the positive effect of nanoconfinement of hydrides in nanoporous scaffolds has been reported by Gutowska et al. [2005] for ammonia borane. A thermodynamic destabilization of MgH_2 nanoclusters with respect to bulk MgH_2 has been predicted from density functional theory (DFT) simulations [Wagemans et al., 2005], which could later be experimentally confirmed for thin films [Mooij et al., 2011] and nanoconfined MgH_2 nanoparticles in a nanoporous carbon scaffold (CMK3), where an onset decomposition temperature as low as 50 °C has been found [Jia et al., 2013].

The present work begins with a short overview about the most important hydrogen storage methods, followed by an introduction to solid state hydrogen storage in general

(Section 2.1) and the here studied hydrides, MgH_2 and LiBH_4 (Section 2.3 and 2.4, respectively). Then, the concept of nanoconfinement, which is one of the central approaches of this thesis, is presented in Section 2.5.

For nanostructured materials, transmission electron microscopy (TEM) is considered as the technique of choice for the structural and chemical characterization at highest resolution [Wang, 2003]. This also applies for the development of nanostructured hydrides. Accordingly, this technique plays an essential role in the present work, and its fundamentals are explained in Section 3.6. In the first part of this work, the focus lies on a methodological approach rather than on material properties. The general behavior of hydrides in the TEM is studied on the example of MgH_2 in Chapter 4, and possibilities as well as limitations of a recently emerged environmental TEM technique are investigated in Section 4.6. In the second part of this work (Chapter 5), TEM is used for revealing important structural and chemical information at the nanoscale of the complex hydride LiBH_4 .

As already mentioned, MgH_2 is chosen as a reference system in Chapter 4. A summary about the hydrogen storage properties of MgH_2 and important studies about the nanoconfinement of MgH_2 are discussed in Sections 2.3 and 2.5.1, respectively. It is unlikely that MgH_2 based materials will ever fulfill the requirements for fuel cell driven vehicles due to the limited gravimetric hydrogen density of 7.6 wt.% of MgH_2 , which makes it impossible to meet the ultimate DOE target of 10 wt.%. Nevertheless, MgH_2 may be valuable for stationary applications because of its high volumetric hydrogen density, low cost, high abundance, reversibility and non-toxicity. Knowledge about the nanoconfinement of MgH_2 could also contribute to the development of other hydrides with higher gravimetric densities. Therefore, MgH_2 is still a material of high interest in the field of solid state hydrogen storage, and it is an ideal system to study its behavior in the TEM. The obtained results can also be transferred to other hydrides, most of which show the phenomenon that they degrade fast upon irradiation with the electron beam in the TEM due to radiolysis (see Section 2.6). Underestimating this phenomenon has recently even led to the erroneous interpretation of an in-situ TEM experiment on MgH_2 [Nogita et al., 2015]. It could be shown that in this study MgH_2 has actually never been investigated in the TEM, since it has been already dehydrogenated by virtue of the imaging electron beam [Surrey et al., 2016b]. This strengthens the importance of appropriately considering the electron beam induced dehydrogenation for planning and correctly interpreting TEM investigations of nanostructured hydrides. In Section 3.6.4 the capabilities of environmental TEM investigations at elevated hydrogen pressures rather than under vacuum are studied by multislice simulations. It is expected that at higher pressures the hydride phase can be stabilized

and radiolysis can be avoided.

Another promising material is the complex hydride LiBH_4 due to its high theoretical gravimetric hydrogen capacity of 18.5 wt.%, however, only 13.9 wt.% are practically usable. It is mainly the high thermodynamic stability and the poor reaction kinetics that prevent its application as hydrogen storage material. A detailed description of the properties of this hydride can be found in Section 2.4. Following the approach of nanoconfinement, the decomposition temperature of LiBH_4 has been reduced to 100 °C by confining it in carbon nanotubes (CNT) or porous CuS nanospheres. Additionally, full reversibility of the dehydrogenation reaction has been achieved [Lai et al., 2014]. This demonstrated that, in principle, nanoconfinement allows to tune the properties of LiBH_4 in order to match the requirements of mobile applications. However, for this a nanoporous scaffold is needed in order to provide for and maintain the nanoconfinement. As a trade off, the dead weight of the scaffold strongly reduces the gravimetric hydrogen capacity. E.g., in the case of CNT or CuS nanospheres as scaffolds, only a LiBH_4 loading of 1 wt.% could be obtained. Although other carbon scaffolds such as highly ordered nanoporous carbon (NPC) [Liu et al., 2011], CMK3 [Cahen et al., 2009] or zeolite-templated carbon [Shao et al., 2015] allow for LiBH_4 loadings as high as 20 to maximal 50 wt.% in these materials, the nanoconfinement resulted only in decomposition temperatures that lie still above 300 °C and that are therefore still far too high for on-board hydrogen storage. Studies about the nanoconfinement of LiBH_4 are described in more detail in Section 2.5.2. Today, it is, however, difficult so see how the production of the above mentioned scaffolds could ever be scaled up to produce large quantities in a cost efficient manner [Fechler et al., 2013]. Therefore, a scaffold with large pore volumes is needed that would allow for LiBH_4 fillings of at least 50 wt.%. Using this scaffold must at the same time result in a decomposition temperature of LiBH_4 that is lowered to the desired level, and its production must be scalable.

In Chapter 5 the use of a for the purpose of nanoconfinement novel and promising carbon scaffold material is studied. The nanoporous carbon is prepared by salt templating, a facile and sustainable technique, which has the advantage of being scalable to large production quantities [Fechler et al., 2013]. It offers large pore volumes, which would in turn allow to reach the aspired high hydride loadings. The material is provided by our collaborator Dr. Nina Fechler from the group of Prof. Markus Antonietti at the Max Planck Institute of Colloids and Interfaces in Golm. The TEM investigations on LiBH_4 nanoconfined in this carbon scaffold are presented and discussed in Section 5.5. The results contribute essentially to the understanding of the nanoconfined LiBH_4 , which turns out to be a promising material candidate for solid state hydrogen storage.

2. Fundamentals

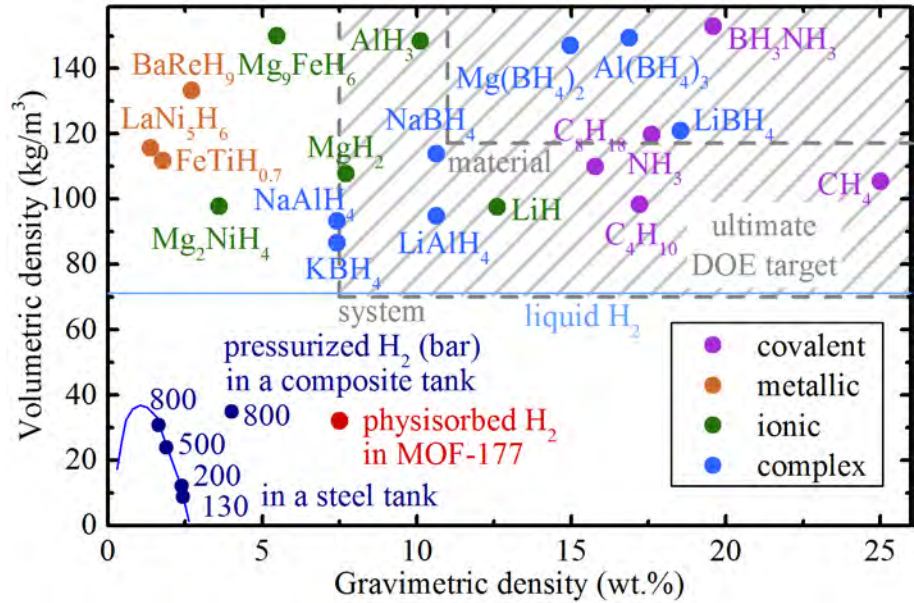
In this chapter, the basic idea of solid state hydrogen storage and the thermodynamic principle will be explained. After discussing MgH_2 and LiBH_4 as two attractive hydrides and how nanoconfinement improves their hydrogen sorption properties, the radiation damage these materials suffer upon structural characterization in the TEM is highlighted.

2.1. Solid state hydrogen storage

Hydrogen can be stored in various forms. Figure 2.1 gives an overview of some selected hydrogen storage methods, whose volumetric hydrogen density is plotted as function of the gravimetric density. The most obvious method may seem to be the storage in the gaseous phase. However, hydrogen is the lightest of all gases with a density of only 90 g/m^3 at 1 bar, and huge volumes would be needed to store sufficient amounts of energy, which is impracticable both for stationary and mobile applications. For example, a fuel cell vehicle with a range of 500 km would require 5 kg of hydrogen, which would have a volume of 55 m^3 . Therefore, the gas must be compressed to higher pressures in order to increase the volumetric density. However, the higher the pressure the thicker the walls of the gas tank have to be, which in turn compromises the gravimetric density. At pressures of up to 800 bar, a volumetric and gravimetric density of 35 kg/m^3 and 4 wt.%, respectively, can be realized with multi-layered cylinders made of composite materials that are reinforced with carbon fibers [Züttel et al., 2015]. As this way of hydrogen storage is the technologically most mature, it is already implemented in the first commercially available cars. However, it is a fact that roughly 15 % of the energy stored in the hydrogen is needed for the compression to 700 bar [Felderhoff et al., 2007], and that such high hydrogen pressures have safety concerns. A big advantage though is the possibility of fast refuelling the tank with gaseous hydrogen.

The volumetric density can be further increased to 71 kg/m^3 by liquefying hydrogen at its boiling point of 21 K. Then, however, already more than 30 % of the stored energy is consumed for the liquefaction, and a continuing loss of hydrogen due to its evaporation cannot be avoided completely.

Figure 2.1 Volumetric and gravimetric hydrogen densities for selected storage methods and materials (adapted from Züttel [2003]). The ultimate DOE targets for the system and the hydride are shaded in grey [Stetson, 2012].



An alternative approach is the physisorption of hydrogen in porous materials with a large surface area. The molecular hydrogen is relatively weakly bound to the surface by the Van-der-Waals interaction (<10 kJ/mol). As a result, the hydrogen uptake and desorption are fast processes, but the storage requires low temperatures. For physisorption, one of the highest hydrogen densities has been achieved with a metal organic framework (MOF-177) with gravimetric and volumetric densities of 7.5 wt.% and 32 kg/m³, respectively, at 77 K and 70 bar hydrogen [Wong-Foy et al., 2006].

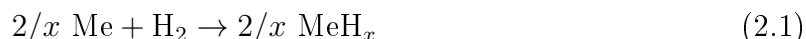
A stronger binding of hydrogen can be realized by chemisorption in the form of hydrides. These materials can be divided in metallic (or interstitial) hydrides, ionic hydrides, complex hydrides, and covalent hydrides. The latter are compounds of hydrogen with non-metals, where the chemical bonding is formed by electron pairs. Most of them are fluid or gaseous at standard conditions, e.g. methane (CH₄), which in fact has the highest gravimetric hydrogen density of all fuels. The other hydrides are generally referred to as solid state hydrogen storages. Common to all of them is, that they have a large volumetric hydrogen density, which exceeds that of liquid hydrogen. In metallic hydrides the hydrogen is located interstitially in the lattice of metals or alloys in the form of protons and the electrons are delocalized. A well known example is LaNi₅H₆ with 1.4 wt.%, which shows excellent reaction kinetics as well as cyclability. However, the gravimetric density of metallic hydrides is limited to about 2 wt.%. Higher gravimetric densities can be found in ionic hydrides. They include all binary hydrides of the alkali and alkaline earth metals, which are extremely electropositive and therefore the hydrogen is negatively charged. A well-studied ionic hydride is magnesium hydride (MgH₂) with hydrogen densities of 7.6 wt.%

and 110 kg/m^3 . Another class are the complex hydrides, that offer even higher gravimetric densities of up to 18.5 wt.% for lithiumborohydride (LiBH_4). In these hydrides, the hydrogen is covalently bound to either Al, B or N forming a negatively charged anion. Together with positively charged metal cations they form salt-like compounds, which are either called alanates $(\text{AlH}_4)^-$, borohydrides $(\text{BH}_4)^-$ or amides $(\text{NH}_2)^-$, respectively.

The U.S. Department of Energy (DOE) has set technical targets for an efficient and economical on-board vehicular hydrogen storage, which are often used as benchmarks. The ultimate DOE targets beyond 2020 for the gravimetric and volumetric densities of the system are 7.5 wt.% hydrogen and $70 \text{ kg hydrogen/m}^3$, respectively, where all parts such as fittings, regulators, the pressure vessel etc. are taken into account. The material capacity of the hydride itself, that constitutes only about 2/3 of the total system weight and volume, must exceed the system target [Stetson, 2012]. These targets arise from the need that, in future, hydrogen-powered vehicles will have to be competitive to the existing technology based on fossil fuels. Some ionic and complex hydrides can in principle meet or come close to these requirements regarding the storage density (cf. Figure 2.1). However, the main shortcoming of chemisorbed hydrogen is usually requiring high temperatures for hydrogen de- or absorption due to high binding and activation energies, and suffering from poor cyclability.

2.2. Thermodynamics

Whereas physisorbed hydrogen is bound too weakly, in chemisorption high temperatures are required for hydrogen release due to a high thermodynamic stability. Whether a hydride is thermodynamically stable under given conditions depends on the sign of the Gibbs free energy change for the decomposition reaction ΔG_r . Generally, a chemical reaction, e.g. hydride formation or decomposition, only takes place spontaneously, if ΔG_r is negative. If ΔG_r is positive, the reaction is disfavoured, and if $\Delta G_r = 0$, the thermodynamic equilibrium is reached. Considering the hydride formation of a metal according to the reaction



the Gibbs free energy change for the reaction is equal to:

$$\Delta G_r = \sum G_{\text{products}} - \sum G_{\text{reactants}}. \quad (2.2)$$

With the definition of the Gibbs energy $G = H - TS$, and using the standard values of enthalpy and entropy, H_0 and S_0 , respectively, equation 2.2 can be written as:

$$\Delta G_r = \Delta H_0 - T\Delta S_0 + RT \ln \left(\prod a_{\text{products}} \right) - RT \ln \left(\prod a_{\text{reactants}} \right), \quad (2.3)$$

where R is the universal gas constant and a_i are the activities of the chemical species. Solids have an activity of unity and the activity of real gases is given by the fugacity f_i/p_0 with the standard pressure $p_0 = 1$ bar [Paskevicius et al., 2010]. For ideal gases at low pressures the fugacity can be approximated by the partial pressure p_i . Then Equation 2.3 can be written as [Aguey-Zinsou and Ares-Fernandez, 2010]:

$$\Delta G_r = \Delta H_0 - T\Delta S_0 + RT \ln \frac{p_0}{p_{\text{H}_2}}. \quad (2.4)$$

At equilibrium $\Delta G_r = 0$, which directly gives the van't Hoff relationship:

$$\ln \frac{p_{eq}}{p_0} = \frac{\Delta H_0}{RT_{eq}} - \frac{\Delta S_0}{R}, \quad (2.5)$$

where p_{eq} is the equilibrium hydrogen pressure and T_{eq} the equilibrium temperature, at which hydrogen de- or absorption can take place (assuming there are no kinetic barriers). Hydrogen is desorbed at $p_{\text{H}_2} < p_{eq}$ and absorbed at $p_{\text{H}_2} > p_{eq}$. At higher temperatures, p_{eq} is higher. The material specific quantities ΔH_0 , which is a measure for the stability of the hydride, and ΔS_0 , which is dominated by the change of state of hydrogen transforming from a diatomic gas to atomic hydrogen in the solid hydride, can be determined by measuring the equilibrium conditions through pressure-composition-isotherms.

Usually proton exchange membrane (PEM) fuel cells operating at 50 – 100 °C or high temperature PEM fuel cells operating at up to 200 °C can be used for fuel cell vehicles, because of their cold-start abilities. Ideally, the resulting waste heat is used to increase the temperature of the hydride storage to release the hydrogen. The hydrogen back pressure needed for PEM fuel cells is 1 – 5 bar. From these boundary conditions and $\Delta S_0 \approx -130$ J/mol/K, which is valid for most hydrides, the standard enthalpy of formation for an ideal hydride can be calculated using Equation 2.5 to be in the range of –60 to –38 kJ/mol, whereas even less stable hydrides with $\Delta H_0 = -10$ kJ/mol are sought to allow for quick desorption. Another technical aspect is, that during hydrogen absorption, which is an exothermic reaction, the heat of formation has to be compensated for. A thermal load of 100 MJ would result from 5 kg hydrogen absorbed by a hydride with $\Delta H_0 = -40$ kJ/mol during refuelling, which should not take longer than 5 min. This would lead to a necessary heat exchanger power of more than 300 kW, which would not be practicable on-board a

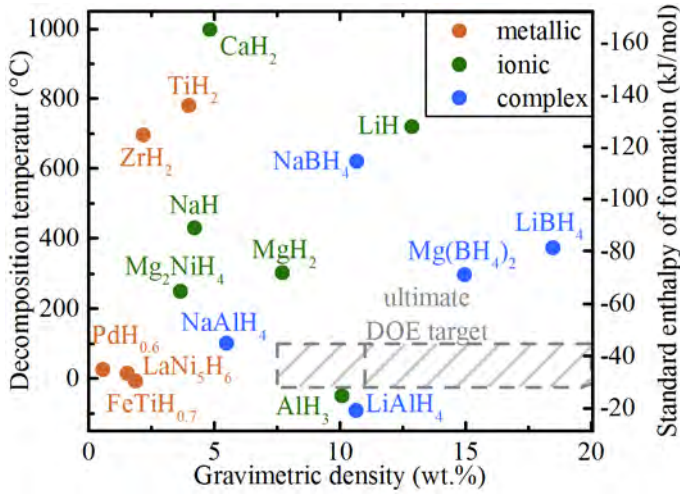


Figure 2.2 Overview of some selected hydrides showing the decomposition temperature at 1 bar hydrogen and standard enthalpy of formation versus the gravimetric hydrogen density (figure adapted from [de Jongh and Adelhelm, 2010]). None of the known hydrides meets the DOE targets.

vehicle. Typically, values less than 100 kW would be reasonable [Felderhoff et al., 2007], and hence hydrides with small absolute enthalpies of formation are favourable. Figure 2.2 gives an overview of some selected hydrides by plotting the decomposition temperature at 1 bar hydrogen and the standard enthalpy of formation as a function of the gravimetric hydrogen density. Unfortunately none of the known hydrides can meet the requirements specified by the DOE [Jia et al., 2015].

2.3. Magnesiumhydride, MgH_2

MgH_2 is considered to be a promising candidate for solid state hydrogen storage due to its relatively high hydrogen storage capacity of 7.6 wt.%, earth abundance, non-toxicity and low cost. However, its thermodynamic stability hampers the practical application. The standard enthalpy and entropy of decomposition are $\Delta H_0 = 75$ kJ/mol and $\Delta S_0 = 130$ J/mol, respectively, which means that temperatures in excess of 300 °C are needed to reach an equilibrium pressure of 1 bar hydrogen. The dehydrogenation follows this simple, reversible reaction



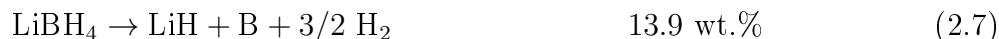
Additionally, poor sorption kinetics with high activation energies for MgH_2 formation and dehydrogenation lead to higher sorption temperatures around 400 °C to achieve reversibility. The origin of the sluggish kinetics is mainly attributed to the slow diffusivity of the hydrogen atoms through the hydride and the metal [Zaluski et al., 1997; Jia et al., 2015]. $Mg(H_2)$ also shows a high reactivity towards oxygen and moisture. Even under an argon atmosphere, the formation of a thin and nanocrystalline/amorphous passivating oxide or hydroxide layer is observable, which also acts as a diffusion barrier for hydrogen [Friedrichs

et al., 2006].

For metal hydrides, the stability can be changed by partial substitution of the consisting metal atoms with other metals, because the delocalized electrons influence the overall stability of the interstitial hydrogen atoms. This is not possible for ionic hydrides, such as MgH_2 or LiBH_4 . Here, the electrons are strongly localized. Therefore, other routes have been developed to destabilize ionic hydrides [Züttel et al., 2003]. One of these is nanoconfinement, which will be discussed in Section 2.5

2.4. Lithiumborohydride, LiBH_4

The complex hydride LiBH_4 is a white, salt-like, hygroscopic and crystalline material with an orthorhombic crystal structure. The four hydrogen atoms are located at the corners of a strongly deformed tetrahedron and are covalently bound to boron in the center of the tetrahedron forming a $(\text{BH}_4)^-$ anion. The Li^+ cation compensates the negative charge of the anion [Züttel et al., 2003]. In total, LiBH_4 has a hydrogen content of 18.5 wt.%, which is the highest among the solid hydrides. However, it decomposes in the following two main reaction steps:



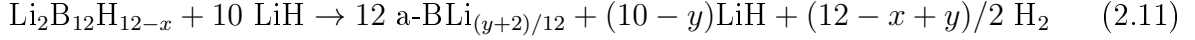
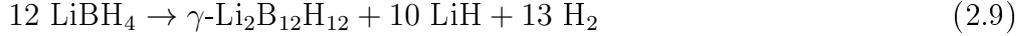
Because the decomposition of LiH according to reaction 2.8 requires very high temperatures around 700 °C, which is unrealistic for any application, only 13.9 wt.% hydrogen according to equation 2.7 is accessible, which is more than sufficient for the automotive application. However, also LiBH_4 is too stable: The standard decomposition enthalpy and entropy are $\Delta H_0 = 74 \text{ kJ/mol}$ and $\Delta S_0 = 115 \text{ J/mol}$ [Mauron et al., 2008], which would translate to a decomposition temperature of 420 °C at 1 bar hydrogen. This temperature is too high to be considered for onboard hydrogen storage. Apart from these unfavourable thermodynamic properties, the hydrogen evolution is further limited by slow kinetics, which results in even higher decomposition temperatures well above the melting point of 278 °C also for lower hydrogen partial pressures .

By means of thermal analysis of LiBH_4 in an argon atmosphere several endothermic effects can be observed in the thermogram [Fedneva et al., 1964]: At 110 °C the reversible, polymorphic phase transformation from the orthorhombic to the hexagonal phase takes place. At 280 °C LiBH_4 is melting, which can be accompanied by a slight evolution of hydrogen. The main hydrogen evolution starts at 380 °C according to reaction 2.7.

This reaction is reversible only at 155 bar hydrogen and 600 °C [Mauron et al., 2008], even though the hydrogen absorption of LiH and B forming LiBH_4 should take place at 1 bar hydrogen and room temperature from a thermodynamic point of view. Hence, the formation is kinetically hindered. The rate limiting step is believed to be the formation of the covalent B–H bond. Indeed it has been shown, that the synthesis of LiBH_4 is possible under mild conditions (room temperature and 1 bar) using LiH and gaseous diborane, B_2H_6 , where the B–H bond is already formed [Friedrichs et al., 2010a]. However, diborane is problematic, because it is toxic and leads to poisoning of the fuel cell. Depending on the experimental conditions, it can also be emitted during the thermal decomposition of LiBH_4 which causes a loss of boron and hence a reduced hydrogen capacity [Kostka et al., 2007]. However, experimentally only small traces or impurities of diborane have been detected, which are even less when LiBH_4 decomposes under hydrogen back pressure [Borgschulte et al., 2011]. It has been observed, that diborane or its monomer borane (BH_3) may react with LiBH_4 at 200 °C producing the crystalline and very stable closoborane salt lithium dodecaborane ($\text{Li}_2\text{B}_{12}\text{H}_{12}$) [Friedrichs et al., 2010b]. At temperatures ≥ 300 °C diborane is unstable and difficult to detect.

As for the role of $\text{Li}_2\text{B}_{12}\text{H}_{12}$ for the decomposition of LiBH_4 , which is still ambiguous and a subject to controversy, contradictory results are published. Yan et al. [2012] have reported that the direct decomposition of LiBH_4 into LiH and boron according to reaction 2.7 is only allowed at pressures below 0.1 bar hydrogen and 600 °C and at higher hydrogen pressures (up to 10 bar) a concurrence of this direct reaction and a two-step reaction via the intermediate $\text{Li}_2\text{B}_{12}\text{H}_{12}$ is observed. At even higher hydrogen pressures (up to 50 bar) LiBH_4 can only decompose via $\text{Li}_2\text{B}_{12}\text{H}_{12}$ to LiH and boron at 600 °C [Yan et al., 2012]. On the other hand Pitt et al. [2013] proposed a more complex three-step decomposition pathway that applies to the decomposition under both vacuum and hydrogen back pressure involving a new polymorph referred to as $\gamma\text{-Li}_2\text{B}_{12}\text{H}_{12}$. According to this, LiBH_4 first decomposes to LiH and boron in the form of $\gamma\text{-Li}_2\text{B}_{12}\text{H}_{12}$, releasing already 10 wt.% hydrogen. The $\gamma\text{-Li}_2\text{B}_{12}\text{H}_{12}$ polymorph decomposes then to an amorphous or nanocrystalline substoichiometric $\text{Li}_2\text{B}_{12}\text{H}_{12-x}$ phase releasing further hydrogen at temperatures between 400 and 600 °C. At 600 °C the $\text{Li}_2\text{B}_{12}\text{H}_{12-x}$ is completely dehydrogenated and LiH and amorphous boron (a-B) remain, whereas some of the Li is dissolved into the amorphous

boron (a-BLi). The decomposition sequence may be written as:



The total amount of released hydrogen depends on the amount of Li dissolved in a-BLi. Reported hydrogen losses from LiBH_4 vary between 9 and 13.8 wt.% dependent on the experimental conditions [Pitt et al., 2013].

While for another complex hydride, sodium alanate (NaAlH_4), an effective catalyst based on Ti has been found, that enables a low temperature (60 °C) hydrogen desorption and leads to full reversibility at relatively mild conditions [Bogdanovic et al., 2000], such a catalyst has not been reported for LiBH_4 . Hence, other strategies have to be explored to improve the hydrogen storage properties of this complex hydride. Nanoconfinement, which will be discussed in the following section, is a very promising approach, that lead to significant improvements not only for LiBH_4 but also for other hydrides within the last decades.

2.5. Nanoconfinement

Nanoconfinement is a strategy to prepare nanostructured materials. This can also be achieved by ball milling (see section 3.1), which allows to decrease the grain size of hydrides down to ca. 10 nm, but usually this nanostructure cannot be maintained and sintering cannot be prevented during cycling or handling. However, by embedding a hydride in a high-surface-area, nanoporous support or scaffold the preparation of particles smaller than 10 nm is possible. Since the material is confined within the nanopores of the scaffold, the particle size is stabilized during heat treatment. The nanoconfinement of hydrides can have tremendous effects on the thermodynamic and kinetic properties of hydrides, which will be explained by examples in the text below. Nanoconfinement can be realized by either melt infiltration or solution impregnation. The former works with materials which have a low melting point and whose melts are able to wet the surface of the support, i.e. show a small wetting angle $\theta < 90^\circ$. Then the melt is pulled into the nanopores by the capillary pressure p_c according to

$$p_c = \frac{2\gamma \cos \theta}{r} \quad (2.12)$$

where γ is the interfacial tension and r is the effective radius of the pore. For LiBH_4 a hydrogen pressure is generally applied during melting to prevent any possible decomposition. For the other method, solution impregnation, a precursor is dissolved in a suitable solvent, which is able to penetrate the pores also through capillary action. After solvent removal the material is highly dispersed in the nanopores.

There are also other routes to prepare nanoconfined hydrides including thin film systems or nanoparticles grown in solution or from the gas phase. Up-scaling is not possible in all cases and hence these routes are more useful for studying the fundamental effects of nanoconfinement rather than for application.

The scaffold must first off all be light, because it otherwise would compromise too much of the achievable gravimetric hydrogen density. To increase this density the scaffold must provide a high nanoporous volume allowing for a high loading of the hydride [Cahen et al., 2009]. The porous material must further be non-reactive towards the hydride or its decomposition products to avoid any irreversible formation of compounds between the hydride and the scaffold. For the purpose of an up-scaling to the production of industrial quantities the production of the scaffold has to be low-cost. Additional functionalities such as high mechanical stability or good thermal conductivity are also beneficial. Nanoporous carbon in various forms has been proven to be a promising scaffold material. [de Jongh and Adelhelm, 2010]

Changes in the thermodynamic properties at the nanoscale have first been reported for the Pd-H system [Eastman et al., 1993]. After the first proof of the impact of nanoconfinement for ammonia borane in 2005 [Gutowska et al., 2005], numerous studies have been published on the effect of nanosizing and nanoconfinement for many hydrides. In the following two paragraphs some of them will be discussed with the focus on MgH_2 and LiBH_4 .

2.5.1. Nanoconfinement of MgH_2

High energy ball milling is a widely used "top-down" approach to prepare nanostructured, $\text{Mg}(\text{H}_2)$ based materials with a grain size in the nanometer regime. Due to breaking of the oxide layer, increased surface/volume ratio, introduction of defects such as twin boundaries, short hydrogen diffusion lengths, and fast hydrogen diffusion channels along grain boundaries, the kinetics could be improved significantly. However, the stabilization of small grain sizes and potential thermodynamic improvements could not be achieved with this technique [Aguey-Zinsou and Ares-Fernandez, 2010]. A further reduction of the MgH_2 particles down to 1 nm results in a thermodynamic destabilization due to a size

effect as predicted by theoretical studies based on density functional theory and the Wulff construction [Wagemans et al., 2005; Kim et al., 2009]. But this particle size is out of reach with ball milling. In the last decade much effort has been devoted to the development of new preparation techniques to produce nanoconfined $\text{Mg}(\text{H}_2)$ with a size in the nanometer regime.

Mg has been successfully incorporated in carbon aerogels with a pore size of 6–20 nm by solution impregnation, which resulted in MgH_2 nanoparticles after hydrogenation [Paskevicius et al., 2011]. Due to the nanostructure, improved dehydrogenation kinetics with lowered desorption temperatures [Nielsen et al., 2009] as well as fast hydrogenation rates have been reported, which are stable during cycling [Zhang et al., 2009; Au et al., 2014]. A MgH_2 loading of max. 17 wt.% could be reached.

Mg nanoparticles with a size of roughly 7 nm were prepared with a higher loading of 60 or 90 wt.% in a polymer matrix grown from solution [Jeon et al., 2011] or by laser ablation [Makridis et al., 2013], respectively. The polymer polymethylmethacrylate (PMMA) not only prevents the nanoparticles from sintering during cycling, but also avoids their oxidation at air, because PMMA shows a selective gas permeability allowing only hydrogen and not oxygen or moisture to penetrate. Due to the oxide-free nanostructure much enhanced kinetics for the (de)hydrogenation were achieved at reduced temperatures of 200–250 °C. Changes in the thermodynamic properties have not been reported, because the particle sizes were still too large to show a size effect.

The MgH_2 – TiH_2 thin film system has been prepared by DC magnetron sputtering and has been studied by optical hydrogenography. Mooij et al. [2011] were able to tailor the thermodynamics by means of the interface energy for Mg thin films with a thickness down to 2 nm. They could show that the hydrogen equilibrium pressure increases for a reduced film thickness, i.e. a reduced equilibrium temperature for a reduced film thickness.

Aguey-Zinsou and Ares-Fernández [2008] have reported the full dehydrogenation already at 85 °C for surfactant-stabilized MgH_2 nanoparticles with a diameter of 5 nm prepared by electrochemical synthesis, which for the first time demonstrated a change in the thermodynamics for MgH_2 nanoparticles, however only 1 wt.% of hydrogen could be stored reversibly due to the weight of the surfactant.

So far, the lowest decomposition temperature of only 50 °C under flowing helium has been reported by Jia et al. [2013] for MgH_2 incorporated in a nanoporous carbon scaffold, called CMK3, with a pore size of 1 – 2 nm. The standard decomposition enthalpy and entropy have been measured with $\Delta H_0 = 55$ kJ/mol and $\Delta S_0 = 105$ J/mol. Similar values were reported by Konarova et al. [2013] and Zhao-Karger et al. [2010], who used CMK3 with pores of 4 nm and activated carbon fibres with pores smaller than 3 nm, respectively.

The reduction in the desorption temperature is less than that expected from theoretical studies due to the decrease in the decomposition entropy, that partially counteracts the effect from the reduced decomposition enthalpy [Paskevicius et al., 2010]. Despite these improvements in the preparation of such extremely small MgH_2 nanoparticles and the achieved thermodynamic destabilization, the materials are not suited for the onboard hydrogen storage, mainly because the decomposition temperature is still too high under hydrogen back pressure and the loading of max. 37.5 wt.% [Jia et al., 2013] is too low.

2.5.2. Nanoconfinement of LiBH_4

For the nanoconfinement of LiBH_4 similar strategies and scaffold materials have been investigated as for MgH_2 .

Gross et al. [2008] have incorporated LiBH_4 into carbon aerogels with an average pore size of 25 and 13 nm with a loading of 25 and 45 wt.%, respectively, and in activated carbon with reported pores smaller than 3 nm by melt infiltration. An increase in the dehydrogenation rate for a reduced pore size and accordingly a reduced dehydrogenation temperature down to 375 °C have been observed. The authors explained this by a shorter hydrogen diffusion distance and a lower energy barrier pathway. Rehydrogenation of the confined LiBH_4 was achieved under relatively mild conditions, 100 bar hydrogen and 400 °C. However, over three cycles, a loss of hydrogen capacity of 30 – 60 % for the 3 nm and the 25 nm pores, respectively, has been observed, which was explained by agglomerated boron and isolated LiH particles, whose formation could not be prevented, because the reaction products were not fully confined in the pores. Changes in thermodynamics could not be clearly identified. In the 13 nm aerogel, the melting point of LiBH_4 was 30 °C lower than in bulk. The evolution of diborane was not observed during the decomposition.

Similar results have been published for 33 wt.% of LiBH_4 nanoconfined in CMK3 with pores of 2 – 4 nm prepared by solution impregnation [Cahen et al., 2009]. By XRD, no long range order of the confined hydride has been observable, implying that the material could be amorphous. However, a melting transition of the nanoconfined LiBH_4 has been measured. The main hydrogen release has occurred at 335 °C with an onset temperature already around 200 °C. Although a change in the desorption enthalpy has not been observed, the authors have claimed that the decomposition has proceeded without the formation of the intermediate compound $\text{Li}_2\text{B}_{12}\text{H}_{12}$. However, rehydrogenation at mild conditions could not be achieved.

For the nanoconfinement of LiBH_4 by melt infiltration in highly ordered nanoporous carbon (NPC) with 2 nm columnar pores prepared from a soft template, it has further

been reported that the low-temperature structural phase transition and the melting transition of LiBH_4 disappeared due to its amorphous structure [Liu et al., 2010]. For LiBH_4 nanoconfined in NPC with 4 nm pores a significantly improved, though still partial, rehydrogenation at relatively mild conditions (60 bar hydrogen and 250 – 350 °C) has been reported with a gradually increasing capacity loss over cycling [Liu et al., 2011]. House et al. [2014] have investigated LiBH_4 confined in such NPC using TEM and have shown that the degradation of storage capacity during cycling is due to the ejection of LiH nanocrystals from the scaffold at high temperature. This observation has been supported by a first-principle study of LiBH_4 clusters on defective graphene sheets, where a dewetting of LiH is predicted [Mason and Majzoub, 2014]. A further cause for the capacity loss has been given by the trapping of boron, which is strongly bound to unsaturated carbon.

So far the highest loading with 40 – 50 wt.% of LiBH_4 into micropores has been reported in a recent work by melt infiltration into a zeolite-templated carbon with pores of ca. 1 – 2 nm and a pore volume of 2 cm³/g [Shao et al., 2015]. The dehydrogenation temperature and reversibility are comparable to the results listed above.

Reversibility of nanoconfined LiBH_4 at milder conditions has been promoted by additionally using nickel nanoparticles incorporated into the nanoporous carbon as catalysts [Ngene et al., 2010].

Solution impregnation of LiBH_4 into carbon nanotubes (CNT) has led to the lowest decomposition temperature of 100 °C (under Ar) reported so far [Christian and Aguey-Zinsou, 2010]. A hydride loading of 7.5 wt.% has been achieved. However, LiBH_4 lost half of its hydrogen capacity in the second desorption. This may be due to the presence of oxide and hydroxyl groups on the CNTs, which leads to a partial oxidation of LiBH_4 , and due to diffusion of LiBH_4 through the open ends of the CNTs upon cycling. This problem has been overcome by the solution impregnation of LiBH_4 in hollow and porous CuS nanospheres, which led to full reversibility (rehydrogenation at 60 bar hydrogen and 300 °C) and a hydrogen desorption temperature around 40 °C (onset) with a peak at 100 °C under Ar. However, only 0.6 wt.% reversible hydrogen capacity has been reached. At this stage, the exact mechanism behind these low decomposition temperatures is unclear [Lai et al., 2014].

The significance of this work is that, for the first time, reversible hydrogen storage by LiBH_4 at the operating temperature of a (high temperature) PEM fuel cell is demonstrated. However, the desorption has been taken place under Ar and not H_2 . The remaining challenge is finding a scaffold enabling this low temperature for cycling with a pore volume of at least 1.5 ml/g, which allows for a LiBH_4 loading of at least 50 wt.%, to meet the requirements of the mobile application, i.e. 7 wt.% hydrogen. The scaffold should also

be able to reversibly accommodate the hydride and its decomposition products within the pores and it should finally provide an environment that facilitates the reversible hydrogen desorption by a catalytically active surface in order to further improve the conditions for reversibility [Lai et al., 2014].

2.6. Radiation damage of hydrides in the TEM

In (S)TEM, the high energetic electron beam provides detailed information about the structure or chemistry of the specimen, but simultaneously it can cause temporary or permanent, desired or unwanted changes in the surface or bulk structure of a specimen. Here, the effect of the electron beam can be manifold. For example, effects such as specimen degradation, radiolysis, contamination, or amorphization as well as knock-on damage resulting in atomic displacements or sputtering, beam-induced heating of the sample, and morphology changes due to enhanced atom diffusion are well-known [Surrey et al., 2012]. Many hydrides decompose fast upon irradiation with the imaging electron beam, which has been reported for LiBH_4 [House et al., 2014], LiH [Deprez et al., 2010], AlH_3 [Ikeda et al., 2009], LiAlH_4 , NaBH_4 [Herley and Jones, 1986] or NaAlH_4 [Egerton et al., 1987]. It is best documented for the extensively studied hydride MgH_2 [Herley et al., 1985; Friedrichs et al., 2006; Danaie et al., 2008]. As already Schober and Chason [1982] stated and as it will be shown in Chapter 4 the beam damage for MgH_2 is caused by radiolysis. Here, the high energy electrons disturb the ionic metal–hydrogen bond. This phenomenon considerably hinders the phase identification and the structural characterization of hydrides at high spatial resolution, unless a cryogenically cooled liquid nitrogen sample holder is used, which limits the lateral resolution. But even at this low temperature the decomposition has been observed, however, on a longer time scale [Danaie et al., 2010]. The electron beam induced dehydrogenation has been studied by Paik et al. [2010] using in-situ electron diffraction to identify the crystallographic orientation relation between MgH_2 and Mg . This dehydrogenation has further been observed in-situ by valence electron energy loss spectroscopy (VEELS) [Paik et al., 2010; Jeon et al., 2011; Danaie et al., 2010], where both phases can be identified by their distinct plasmon energies [Zaluzec et al., 1981]. However, little is known about the mechanism governing the rate of the electron beam induced dehydrogenation and a quantitative description of this effect is lacking. Even until recently, this beam induced dehydrogenation has led to a false interpretation of TEM investigations of MgH_2 [Nogita et al., 2015]. Actually, MgH_2 has never been studied by the authors in the TEM, since it has been already dehydrogenated due to the imaging electron beam [Surrey et al., 2016b]. Especially, with respect to the nanoconfinement of hydrides, the precise knowledge

2. *Fundamentals*

of the nanostructure is mandatory for the understanding and further development of these materials, where TEM is an indispensable tool.

3. Theoretical and Experimental Methods

3.1. Ball milling

Ball milling is a technique used for grinding and blending materials. In a planetary ball mill, the material is placed with the grinding balls in a grinding jar arranged eccentrically on a rotation sun wheel. The grinding jar rotates in the opposite direction. As a consequence, the grinding balls experience a Coriolis force, which causes high impact forces and different speeds between the balls and the jar wall. The material in between undergoes a reduction of particle and grain size, and an increase in defect density.

In this work, ball milling of MgH₂ powder (purchased from Goldschmidt) was performed under argon atmosphere in a Retsch PM400 planetary ball mill using hardened steel balls and vials. The powder was milled for 80 h at a ball-to-powder mass ratio of 10:1 at a milling intensity of 200 revolutions per minute. All sample preparation and handling was performed in a MBraun argon filled glove box with water and oxygen levels below 2 ppm to prevent oxidation and contaminations of the sample.

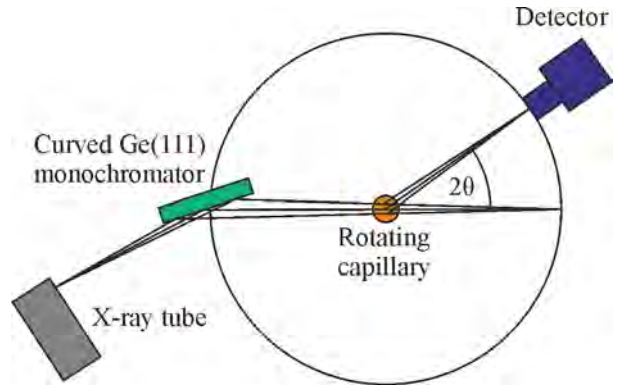
3.2. X-ray diffraction analysis

X-ray diffractometry (XRD) is a technique to determine the three-dimensional atomic structure of a crystalline sample. The X-rays with a wave length λ in the order of Å are scattered elastically on the periodic crystal lattice, which results in a material specific diffraction pattern. Angles θ , at which strongest constructive interference can be observed, are given by Bragg's law [Gross and Marx, 2012]:

$$2d \sin \theta = n\lambda. \tag{3.1}$$

Here, d is the distance between atomic lattice planes and n is a positive integer, indicating the order of the diffraction. Polycrystalline materials are usually studied by powder

Figure 3.1 Schematic illustration of the Debye-Scherrer geometry (figure adapted from [STOE, 2016]).



diffraction, where the Debye-Scherrer geometry is used (see Figure 3.1).

In this work, XRD measurements were performed on a Stoe Stadi P with Mo- $K\alpha_1$ radiation with a wavelength of 0.7093 Å in Debye-Scherrer geometry. The diffractometer is equipped with a curved Ge (111) monochromator and a 6° linear position sensitive detector. The sample powders were filled in glass capillaries with an outer diameter of 0.7 mm in an argon filled glove box and then sealed to prevent an oxidation of the samples.

3.3. Thermal Characterization

3.3.1. Differential Scanning Calorimetry

Differential Scanning Calorimetry (DSC) is a thermoanalytical technique to investigate phase changes or reactions of a material at different temperatures or gas environments. In a heat flux DSC instrument, which functions according to the principle of the differential thermal analysis (DTA), the sample and an inert reference are heated in a furnace with in general a constant heating rate. As a consequence, the temperature of the reference, T_R , is increasing linearly in time as well as the sample temperature T_S , but with a different rate due to a different heat capacity, which leads to a temperature difference $\Delta T = T_S - T_R$ between sample and reference. If the sample undergoes an endo- or exothermic reaction in the form of a phase change or a chemical reaction, ΔT will change as function of time, because T_R does not follow the linear temperature increase anymore. This ΔT is proportional to the difference between the heat flow rates Φ to the sample and to the reference [Höhne et al., 2013]:

$$\Phi_S - \Phi_R \propto \Delta T. \quad (3.2)$$

After suitable calorimetric calibration, this difference in heat flow rates can be directly measured and enthalpies of phase changes or chemical reactions can be determined by integration of the peaks in the $\Delta T-T_R$ -curve.

The DSC measurements presented in this work were conducted in a Netzsch 204 HP DSC, which is operated within an argon filled glove box.

3.3.2. Coupled Thermogravimetry and Mass Spectroscopy

Measuring the weight of a hydride upon heating is essential for the characterization of the hydrogen desorption. The thermogravimetry (TG) measurements presented in this work were conducted using a Sensys evo from SETARAM, which is a combined TG-DSC integrated in an argonfilled glovebox. The measurements were carried out under an argon flow at 1 bar with a heating rate of 1 K/min up to max. 550 °C. The TG-DSC system is coupled to a mass spectrometer (MS) from Pfeiffer Vacuum (Omnistar GSD 320 O1), which is located outside the glove box and connected via a heated stainless steel capillary (length of 1 m and temperature of 423 K). The MS uses an yttriated iridium filament for the ionization of the gas and a QMG 220 quadrupole for separation of the gas ions according to their mass to charge ratio m/q . The ration of $m/q = 2$ (H_2^+ ions) corresponding to the hydrogen released from the sample was monitored. For the detection of diborane, B_2H_6 , the ion current was measured at $m/q = 24$ [Liu et al., 2010]. The collected masses were monitored by an integrated continuous secondary electron multiplier (C-SEM) detector.

The unique experimental setup of coupled TG–DSC–MS was build and installed by Dr. Inge Lindemann and the IFW Research Technology [Lindemann, 2014].

3.4. Melt infiltration of LiBH_4

Physical mixtures of ca. 20 to 50 mg with 40 and 50 wt.% of the LiBH_4 powder (purity of $\geq 95.0\%$, purchased from Aldrich) and the aerogel-like carbon scaffolds were prepared by mixing with a pestle in a mortar. The melt infiltration was conducted in a DSC using a Netzsch 204 HP DSC. The mixture of typically 10 mg was heated to 300 °C at 5 K/min with a dwell time of 30 min under a constant pressure of 60 bar hydrogen and then cooled to room temperature. All sample preparation and handling was performed in a MBraun argon filled glove box with water and oxygen levels below 2 ppm to prevent oxidation and contamination of the samples.

3.5. Solid State Nuclear Magnetic Resonance

Many nuclei have a spin angular momentum and therefore possess a magnetic moment μ . In the classical model, μ precesses around an external magnetic field \mathbf{B}_0 with the Larmor

frequency

$$\omega = \gamma \mathbf{B}_0, \quad (3.3)$$

where γ is the gyromagnetic ratio, which is characteristic for all nuclei. The Larmor frequency can be measured by applying an electromagnetic wave to the sample and varying the frequency until maximal absorption at the resonant frequency ω is detected [Jacobsen, 2007]. In the quantum mechanical description, this corresponds to the transition of the nuclear spins between different nuclear magnetic energy levels, which are separated by the Zeeman splitting of $\Delta E = \hbar\omega$ [Mason, 1987].

Each nucleus is surrounded by electrons. Due to the external magnetic field \mathbf{B}_0 electric currents are produced surrounding the nuclei. These currents themselves produce a magnetic field at the nucleus. The nucleus then experiences an effective field

$$\mathbf{B}_{\text{eff}} = \mathbf{B}_0(1 - \boldsymbol{\sigma}), \quad (3.4)$$

where the tensor $\boldsymbol{\sigma}$ is the nuclear magnetic shielding and depends on the chemical environment of the nucleus. This leads to a chemical shift δ of the resonant frequency ω , which is defined as

$$\delta = \frac{\omega - \omega_{\text{ref}}}{\omega_{\text{ref}}} \quad (3.5)$$

relative to the resonant frequency ω_{ref} of a reference material [Mason, 1987]. In general these shifts are relatively small and expressed in parts per million (ppm). By measuring ω , the nuclei present in a sample can be identified, and measuring δ allows to investigate the chemical bonds of the nuclei.

Magic Angle Spinning

All nuclei with a spin $> 1/2$ behave as magnetic dipoles, which can couple to each other. This magnetic dipole coupling leads to a broadening of the resonant line in a NMR spectrum and is proportional to $1 - 3 \cos^2 \theta$, where θ is the time average of the angle between the external magnetic field and the connection line, or the internuclear vector between two interacting nuclei. If the entire sample is rotated rapidly around an angle $\theta' = 54.74^\circ$, whereby the term $1 - 3 \cos^2 \theta'$ is zero, the time averaged dipolar coupling will vanish, because then, averaged over time, *every* internuclear vector makes this angle θ' with the external magnetic field. This method is called magic angle spinning (MAS) and leads to a narrowing of the resonant peaks [Slichter, 1990].

The solid state MAS NMR spectra presented in the present work for ^{11}B were measured in a wide bore 7 T magnet using a Tecmag Apollo NMR spectrometer and a NMR Service

Eagle H-X 4 mm CP/MAS probe. The reported NMR shifts are given relative to an external reference, $\text{BF}_3\text{Et}_2\text{O}$, for which the chemical shift of 0 ppm is defined for the ^{11}B nuclei. The powder materials were packed into 4 mm ZrO_2 rotors in an argon-filled glove box. The vials were sealed with tight fitting Kel-F caps. The sample spinning was performed using dry nitrogen gas. The MAS spinning rate was 10 kHz, and the applied radio frequency was 96.29075 MHz. Pure LiBH_4 , which has a reported resonance at -41 ppm [Hwang et al., 2008], was used as a reference. The measurements were carried out by Dr. Hans-Joachim Grafe at the IFW Dresden.

3.6. Transmission Electron Microscopy

In this chapter only the basic principle of a transmission electron microscope (TEM) and the experimental setup will be explained. Theoretical details on the image formation due to the elastic scattering of the electron wave with the atoms of the specimen are given in Section 3.6.4. Spectroscopic information of the specimen can be obtained by electron energy loss spectroscopy due to inelastic scattering, which will be explained in Section 3.6.3.

The functional principle of a TEM is similar to that of a conventional light microscope with the main difference that high energetic electrons instead of photons are used for imaging. According to Abbe, the resolution of any microscope is determined by the wavelength λ of the imaging wave with $\approx \lambda/2$. Hence, the resolution of a microscope using visible light is limited to ≈ 200 nm. However, de Broglie discovered that also massive particles, such as electrons, possess properties of a wave with a wavelength $\lambda = h/p$, where h is Planck's constant and p is the momentum of the particles. Therefore, electrons with an energy of 300 keV have a wavelength of only 2 pm, which is small enough to resolve atomic structures in the regime of Ångströms. The modulation of electron waves by magnetic lenses is technically more difficult than refracting light by glass lenses, which results in aberrations that can partially be corrected for. These aberrations and the partial coherence of the electron wave limit the resolution of TEMs to ca. 0.8 \AA .

For this work, a FEI Titan³ 80-300 has been used. The schematic structure is depicted in Figure 3.2(a). The microscope is equipped with a Schottky emitter, from which the electrons are extracted through a highly negative potential due to field electron emission from a heated tungsten tip coated with zirconium oxide. This type of emitter combines the advantages of high emission currents and good temporal and spatial coherence. The electron source is followed by a monochromator, which will be described in Section 3.6.3. The electrons are injected into the microscope column by virtue of acceleration voltages of

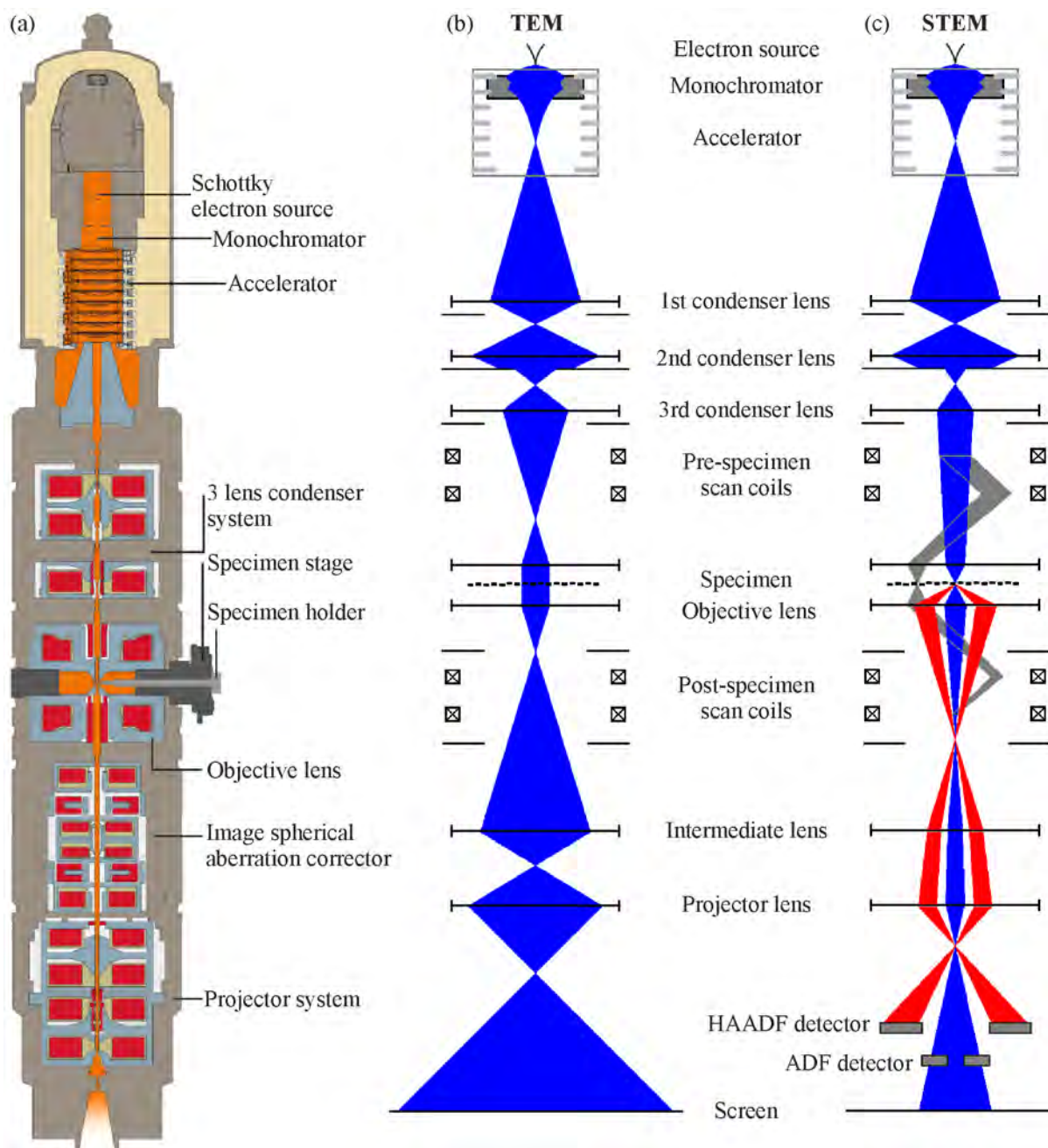


Figure 3.2. (a) Schematic structure of a FEI Titan³ 80-300 (©FEI). (b) Path of the electron beam through the microscope in TEM mode and (c) in STEM mode [Hartmann, 2010]. The beam along the optical axis is coloured in blue, an off-axis scanning beam in grey and a high angle scattered beam in red.

80 kV or 300 kV. A triple electromagnetic condenser lens system forms a close to parallel electron beam illuminating the specimen in TEM mode (see Figure 3.2(b)). After the interaction with the specimen the scattered electron beam is brought to a point focus on the back focal plane of the objective lens, which is the main lens for the image formation. Aberrations of this lens, mainly the spherical aberration, can be corrected using the image spherical aberration corrector. The following projector lens system magnifies the image onto a fluorescent viewing screen or a charged couple device (CCD) camera. The FEI Titan³ 80-300 is equipped with a 2048x2048 pixel CCD camera of the type Gatan UltraScan 1000.

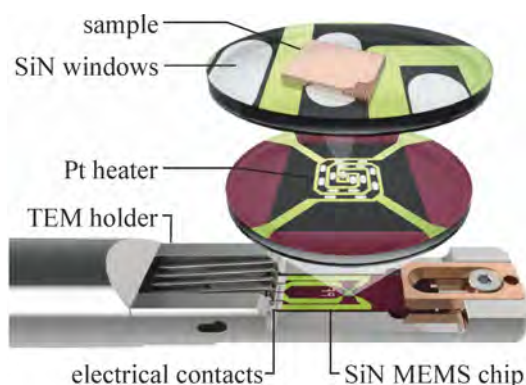
For scanning TEM (STEM) mode, the condenser system and the objective lens form a convergent electron beam, which can be focused to a size of ca. 1 Ångström (see Figure 3.2(c)). This fine electron probe is scanned over the specimen using the pre- and post-specimen scanning coils. The scattering of electrons to high angles is described by Rutherford-scattering rather than Bragg scattering. These electrons with scattering angles >50 mrad are detected by the High Angle Annular Dark Field (HAADF) detector [Williams and Carter, 2009]. HAADF images show a Z-contrast, because the elastic scattering cross section to high angles is proportional to Z^2 . For low-Z elements it is also useful to use an annular dark field (ADF) detector, that detects electrons with scattering angles of 10 – 50 mrad. The (HA)ADF STEM image is generated by recording the intensity of the scattered electrons for each scanned pixel.

The imaging system is followed by an electron energy loss spectrometer (EELS) of the type Gatan Tridiem 865ER, which allows to measure low-loss as well as core-loss spectra for the chemical analysis of the specimen (see Section 3.6.3).

3.6.1. In-situ TEM Heating

In the present work, the in-situ heating of samples inside the TEM is carried out using a MEMS (micro-electro-mechanical system) based TEM heating holder (DENS Solutions Wildfire). The heating is achieved by an electrical current through a spiraled thin-film Pt wire with a size of 0.3 mm x 0.3 mm (see Figure 3.3) on a 1.2 μm thick SiN membrane, which is 1 mm² in size. The temperature is derived by measuring the electrical resistance of the Pt wire via a four point measurement. The specimen is placed on electron transparent SiN windows, which are located in between the Pt spiral path with a thickness of 20 nm. The Pt heater is covered with SiN for electrical insulation. The setup is integrated on a 3 mm x 10 mm Si chip with four electrical contacts. This chip is placed in the Wildfire TEM holder instead of the usually used TEM grids. [DENS Solutions, 2016; Creemer

Figure 3.3 Illustration of the DENS Solutions Wildfire TEM holder for in-situ heating. The SiN membrane supporting the Pt heater is magnified twice to clearly show the heater spiral and the SiN windows [DENS Solutions, 2016].



et al., 2008]

Due to the small size and the very low mass of the heated element, only minimal power of a few mW is consumed. Therefore very fast heating and cooling rates of 200 K per millisecond are possible. The heater is further characterized by a small spatial drift, which allows to easily follow individual nanoparticles upon heating. Due to the high stability atomic resolution can be achieved even at temperatures of up to 1000 °C.

In Section 5.5 the nanoporous aerogel-like carbon is studied with this heating holder. Under the electron beam the substrate and sample become electrostatically charged, because the entire heater is insulating. This leads to the immediate detachment of the carbon particles from the substrate due to electrostatic repulsion. The attachment of the carbon particles and the substrate is too loose due to a small contact area between them, which results in Van der Waal forces that are too small to counteract the electrostatic repulsion forces. To avoid this the heater chip was covered with a 5 nm thin amorphous and conductive carbon film by RF sputtering without covering the electrical contacts, which would otherwise result in a shortcut.

3.6.2. Environmental TEM

Usually a TEM is operated under high vacuum, the FEG is even under ultra high vacuum, because the electrons must pass through the microscope without being scattered by gas atoms too much, which would reduce the resolution. However, scientific topics dealing with gas-solid interactions, such as heterogeneous catalysis [Hansen et al., 2006], require in-situ measurements at higher pressure. This technique is called environmental TEM (ETEM). A gas environment around the sample can be realized via a differentially pumped vacuum system, with which the achievable pressure is limited to approximately 10 mbar, because in the rest of the microscope, especially at the electron source a high vacuum level must be maintained. By this approach the hydrogenation and dehydrogenation of individual

Pd nanocrystals could be studied at pressures up to 6 mbar [Baldi et al., 2014]. A TEM cryo holder has had to be used for cooling the sample to $-27\text{ }^{\circ}\text{C}$ to be able to reach the equilibrium conditions of PdH_x . Matsuda et al. [2014] also used ETEM to observe the initial stage of the hydrogenation of Mg-Ni films at a pressure of up to 1 mbar. These experimental conditions are still far away from the technological application conditions of these hydrides, i.e. pressure ≥ 1 bar and temperature $\geq 100\text{ }^{\circ}\text{C}$. Another approach for ETEM uses special TEM holders with a windowed environmental cell, e.g. the so-called nanoreactor [Yokosawa et al., 2012], that is able to bridge this pressure gap and allows for pressures up to 4.5 bar, while heating the sample in-situ up to $400\text{ }^{\circ}\text{C}$. For this, the specimen in the gas environment is enclosed between thin and electron transparent membrane windows, typically composed of amorphous SiN. With this setup the hydrogenation and dehydrogenation of Pd could be followed and no influence of the electron beam on the (de)hydrogenation was noticed [Yokosawa et al., 2012]. A point resolution of 1.8 \AA has been demonstrated experimentally for Cu nanocrystals [Creemer et al., 2008] at $500\text{ }^{\circ}\text{C}$ and 1.2 bar H_2 in the nanoreactor.

With a windowed environmental cell, a higher pressure than with a differentially pumped vacuum system can be realized still enabling atomic resolution, because the number of gas atoms along the path of the electron beam, i.e. the areal atom density projected on the basal plane of the gas layer, is smaller for a windowed cell. E.g. in a differentially pumped ETEM, a gas layer at 25 mbar with a thickness of 5 mm corresponds to a gas density of 3×10^3 atoms/nm² [Hansen et al., 2006]. In a windowed cell each window already contains 2×10^3 atoms/nm², but due to the much thinner gas layer of $19\text{ }\mu\text{m}$ only 1×10^3 atoms/nm² are added to the total density of gas and window atoms of 5×10^3 atoms/nm². This is comparable to the value calculated for the differentially pumped ETEM, however, at *ambient* pressure [Creemer et al., 2008]. A further advantage of windowed type ETEM is that it also allows for liquid cells, where samples can be studied in solutions [Woehl et al., 2012].

The nanoreactor uses a design similar to the in-situ heating holder described in Section 3.6.1 with the difference that two Si MEMS chips are placed on top of each other and are sealed with O-rings. A micrometer-sized gas-flow channel is embedded in between the chips. The design of the tip of the TEM holder is shown in the schematic diagram in Figure 3.4(a). If pressurized the top and bottom SiN windows are separated by $19\text{ }\mu\text{m}$. The gas volume enclosed in between the top and bottom SiN windows is illustrated in Figure 3.4(b) with a Mg or MgH_2 nanocrystal as specimen.

So far, only few studies have investigated ETEM theoretically. For example, de Jonge et al. [2010] have calculated the broadening of the electron probe due to its interaction with

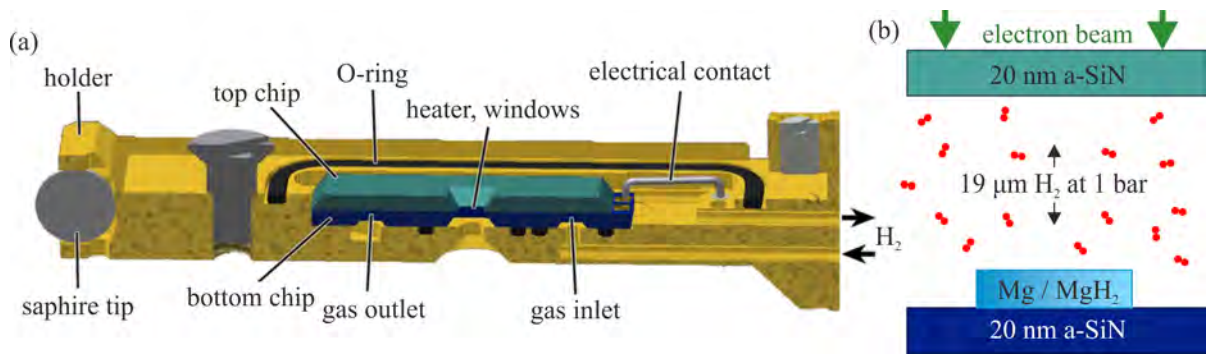


Figure 3.4. (a) Schematic diagram of the tip of TEM holder with a windowed environmental cell [Yokosawa et al., 2012]. (b) Magnification of the enclosed gas volume in between the top and bottom SiN windows.

the SiN window of an environmental cell in a STEM experiment, thereby, however, not considering the gas contained in the cell at atmospheric pressure. A quantitative theory for phase contrast HRTEM imaging has been developed by Suzuki et al. [2013], where the authors have estimated the information limit for window-based ETEM by calculating the contrast transfer function under the effect of the membrane windows and the enclosed gas. A multislice approach has been used by Yoshida and Takeda [2005], who have modeled HRTEM imaging of a single-walled carbon nanotube in a gaseous environment of 7 mbar of ethanol by simply compressing the 3 mm thick gas layer to only 100 nm, however, without taking into account any membrane windows. Another elaborate multislice study has been undertaken by Welch et al. [2013] for HAADF STEM in a liquid contained in an environmental cell. Again, however, the simulated fluid path length of 50 – 500 nm has been much smaller than the typical thickness of 19 μm of windowed gas cells, which is a significant difference for multislice simulations.

3.6.3. Electron Energy Loss Spectroscopy

The contents of this chapter have mainly been adapted from the textbook on electron energy loss spectroscopy (EELS) by Egerton [1989]. In EELS the energy distribution of the electrons that are transmitted through the specimen are analyzed. Most electrons undergo no inelastic interaction, i.e. have zero energy loss, but those electrons that are scattered inelastically transfer a certain amount of energy to the specimen, and they experience an energy loss, which can be measured in the energy spectrum. Inelastic scattering of the incident high energy electrons occurs as a result of the Coulomb interaction with the electrons of the atomic shell.

Inner-Shell Excitation

Inner-shell electrons are bound typically by some hundreds or thousands of electron volts. If they absorb an amount of energy similar to or greater than this binding energy, which is characteristic for the element, the electrons can make an upward transition above the Fermi energy, where unoccupied electron states exist. The incident electron loses exactly this amount of energy, which is referred to as a core-loss, and is scattered through an angle of typically smaller than 10 mrad. The highly excited or ionized target atom quickly releases the excess energy through a de-excitation process, in which an outer-shell electron or a lower bound inner-shell electron undergoes a downward transition filling the vacant hole in the inner-shell. The excess energy is liberated by the emission of either a X-ray photon or an Auger electron depending on the atomic number Z of the target atom. Because the electron beam can be focused to a fine probe of less than an Ångström in STEM and all inelastic scattering events occur only in the small volume of the transmitted electron beam, chemical information of the specimen with high spatial resolution up to the atomic level can be achieved. Comparable information can also be acquired using STEM in combination with energy dispersive X-ray spectroscopy (EDX), however, the probability of the de-excitation via characteristic X-rays decreases for low Z elements. Therefore, EELS is especially useful for the investigation of light elements, where the count rate of core-loss electrons is still high for low Z atoms. Therefore EELS rather than EDX is used for the investigation of the distribution of boron in nanoporous carbon scaffolds in the present work, which is presented in Chapter 5, Section 5.5.

Plasmon Excitation

The incident electrons can also interact with the outer-shell electrons, i.e. the valence electrons. Then the transmitted electrons lose energies typically of up to 50 eV, which is called the low-loss region of the energy loss spectrum. If only such energy losses are considered the technique is termed valence electron energy loss spectroscopy (VEELS). The inelastic scattering can be caused by inter band transitions or the excitation of plasmons, among others. A plasmon is a pseudoparticle and describes the collective oscillation of the valence electrons. In the Drude model for quasi-free electrons the displacement of the valence electrons is treated as a damped harmonic oscillator, which is driven by the incident electron beam. The resonant frequency ω_p for the plasma oscillation is given by:

$$\omega_p = \sqrt{\frac{ne^2}{\epsilon_0 m}}, \quad (3.6)$$

where e is the elementary charge, ϵ_0 is the electric constant, m is the effective electron mass, which can be approximated by the rest mass, and n is the number of valence electrons per unit volume, which depends on the material and gives rise to characteristic plasmon frequencies. The plasmon has the characteristic energy $E_p = \hbar\omega_p$, with \hbar being the reduced Planck constant. The agreement between measured and calculated plasmon energies is good for most elemental materials. The energy-loss spectrum $I(E)$ for the excitation of a plasmon can be calculated from the imaginary part of the dielectric function $\epsilon(\omega)$ and is given by:

$$I(E) = \frac{E_p^2 E \hbar / \tau}{(E^2 - E_p^2)^2 + (E \hbar / \tau)^2}, \quad (3.7)$$

where τ is the relaxation time representing the time for the plasmon to decay due to the dampening of the oscillation. Equation 3.7 can be approximated by a Lorentz function

$$L(E) = \frac{2A}{\pi} \frac{w}{4(E - E_c)^2 + w^2}, \quad (3.8)$$

where A is the area under the Lorentz curve, w is the width and E_c is the center of the curve. For sharp plasmon losses typical for metals with $\hbar/\tau \approx 1$ eV the energy spectrum $I(E)$ is equal to a Lorentz function and $E_c \equiv E_p$.

VEELS is especially useful for the detection of hydrogen in the specimen, which is not possible by EDX. If hydrogen atoms enter the metal lattice, either occupying interstitial lattice sites or leading to a formation of a new ionic hydride phase, one valence electron per hydrogen atom is added, which increases the valence electron density n . This leads to an upward shift in plasmon energy, which has been observed for many metallic and ionic hydrides. This technique is used in the present work to study the electron beam induced dehydrogenation of MgH_2 , which is presented in Chapter 4.

Plasmon Scattering Cross Section

The probability of the inelastic scattering of an incident electron with the specimen up to an angle β is given by the energy-differential cross section:[Egerton, 2011]

$$\frac{d\sigma(\beta)}{dE} \approx \frac{I(E)}{\pi a_0 m_0 v^2 n_a} \ln(1 + \beta^2 / \theta_E^2) \quad \text{with } n_a = \frac{x \rho N_A}{M} \quad \text{and } \theta_E = \frac{E}{\gamma m_0 v^2}. \quad (3.9)$$

Here a_0 is the Bohr radius, m_0 is the electron rest mass, v is the electron velocity, n_a represents the volume density of the atoms in the medium given by the mass density ρ and the molecular mass M (N_A is the Avogadro constant), x is the number of atoms per molecule, e.g. $x = 3$ for MgH_2 , and $\gamma^2 = (1 - v^2/c^2)^{-1}$ is the Lorentz factor. $I(E)$ is the

energy-loss spectrum of a plasmon given by Equation 3.7. Equation 3.9 is only valid for scattering up to angles β smaller than the plasmon cutoff angle θ_c of typically 10 mrad. In practice, plasmon excitations can cause also some inelastic scattering to angles above $\theta_c \approx 10$ mrad. So the total inelastic scattering cross section can be typically 10 – 20% larger. To get the total inelastic scattering cross section Equation 3.9 must be integrated over the energy loss E . But since both quantities $S(E)$ and θ_E depend on E , a simple analytical expression is not possible, but the integration has to be done numerically.

Fourier-Log Deconvolution

It is mandatory to remove the effects of plural scattering from the energy loss spectrum for a spectral analysis to obtain quantitative information about the chemical composition of the specimen. The Fourier-log deconvolution is an accurate and powerful technique to remove the plural scattering and the zero-loss beam from a low-loss spectrum, which results in the pure single loss spectrum $S(E)$. It can be calculated according to:

$$S(E) = FT^{-1} \left[I_0 \ln \frac{m(\nu)}{z(\nu)} \right], \quad (3.10)$$

where $m(\nu)$ and $z(\nu)$ are the Fourier transforms of the the measured energy loss spectrum $M(E)$ and the spectrum of the zero-loss peak $Z(E)$, respectively. The derivation of Equation 3.10 can be found in Section A.1 in the appendix.

For the quantitative analysis of the Mg(H₂) VEEL spectra presented in Section 4.2, the Fourier-log deconvolution implemented in the software DigitalMicrograph is used. For this, the experimentally measured zero-loss peak without the specimen is chosen as the re-convolution function.

Measurement of Specimen Thickness

Low-loss spectra can be used to estimate the thickness of a specimen. According to Equation A.1 the intensity of the zero-loss peak is given by:

$$I_0 = I \exp(-d/\lambda), \quad (3.11)$$

where I is the total incident electron intensity, and d is the thickness of the specimen. In an experimental spectrum, I_0 is represented by the area under the zero-loss peak, which has a certain energy spread. The total intensity I is given by the area of the entire loss-loss spectrum including the zero-loss peak up to some suitable energy loss Δ , where the intensity should ideally fall to zero. λ is the mean free path for inelastic scattering with

energy losses less than Δ . From Equation 3.11 the relative thickness can be obtained:

$$d/\lambda = \ln(I/I_0), \quad (3.12)$$

which provides a simple way of estimating the specimen thickness. If λ is known, also the absolute thickness d can be calculated. However, already d/λ is very useful for comparing specimens composed of the same material. It has been found that the relationship in Equation 3.12 yields results with an accuracy of 10 % for thicknesses in the range of $0.2 < d/\lambda < 5$. For smaller thicknesses surface excitations may be significant leading to an overestimation of the thickness.

Monochromator

The energy resolution of an EEL spectrum is mainly limited by the energy spread of the incident electron beam. The electrons are not monoenergetic, because they are emitted from a thermionic source and their energies follow a Maxwellian distribution. Another cause for the energy spread is the Boersch effect, which describes the Coulomb interaction of the electrons among each other in the beam. The resulting energy spread depends on the path length of the electrons and on the current density, which is highest already within the electron gun. Further broadening occurs at gun cross overs, where the electrons are focused into a small volume.

The energy spread of the electron beam can be reduced using a Wien filter as a monochromator. It consists of a homogeneous magnetic and electric field which are perpendicular to each other and perpendicular to the electron beam. This leads to a dispersion of the electron beam with respect to its energy. From this dispersed beam a fraction of the electrons having a narrower energy distribution can be selected using a slit or hole aperture before the beam enters the condenser system.

Figure 3.5 shows the result of the monochromation of the zero loss beam at acceleration voltages of 80 kV and 300 kV at the FEI Titan³ 80-300 microscope. As a result the full width half maxima are reduced to 0.26 eV and 0.44 eV, respectively. In addition to the improved energy resolution, this has the advantage that the overlap of the narrower zero loss peak with the to be measured low loss spectrum at small energy losses < 5 eV is reduced. This is beneficial for the quantitative analysis of deconvoluted low loss spectra, which is presented in Section 4.2.

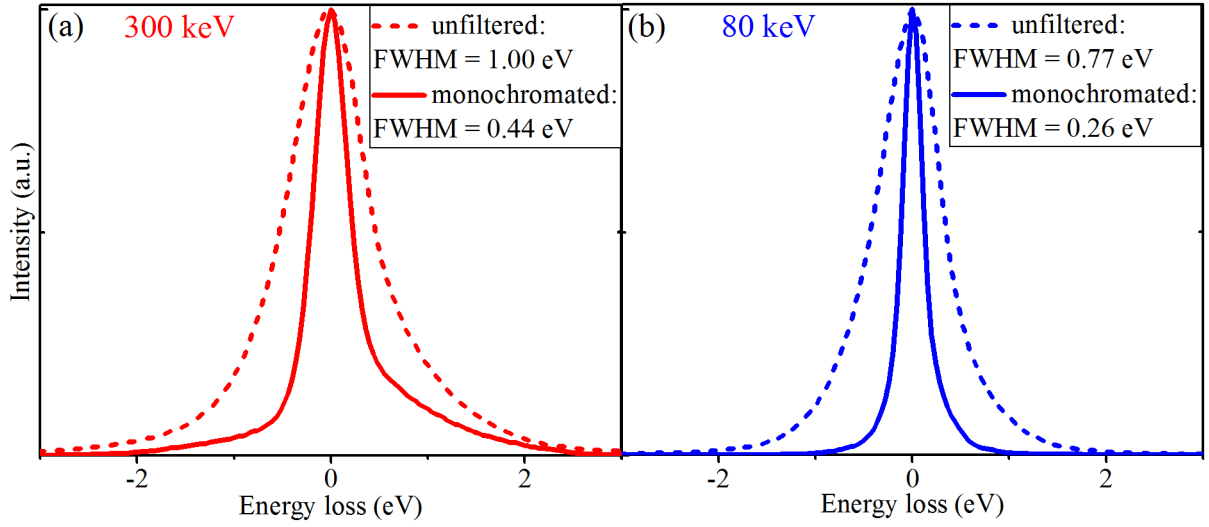


Figure 3.5. Comparison of the normalized zero loss peaks in the unfiltered and monochromated mode for electron energies of (a) 300 keV and (b) 80 keV. The full width half maximum (FWHM) can be reduced to 0.44 eV and 0.26 eV, respectively, which improves the energy resolution of the spectra. The 5 mm entrance aperture of the spectrometer is used.

3.6.4. Multislice Simulations

The multislice method is a numerical technique for the simulation of the interaction of the electron wave with the specimen. The electrons are described by a complex wave function with phase and amplitude. The term multislice originates from the ansatz of approximating the three-dimensional specimen by many two-dimensional slices, for which the quantum-mechanical scattering problem is solved separately. The interaction of the relativistic electron wave with the atoms of the specimen is described by the Schrödinger equation with the relativistically correct wavelength λ and mass m :

$$\left[-\frac{h^2}{8\pi^2m} \nabla^2 - e\phi \right] \Psi = E_0 \Psi, \quad (3.13)$$

where h is the Planck constant, e the elementary charge, ϕ the atomic potential and E_0 the energy of the incident high energy electron [Humphreys, 1979]. However, an analytical solution for this equation is difficult to obtain for non-periodic three-dimensional potentials. Therefore, the problem needs further simplification. For very thin objects with a thickness d , it can be assumed that an incoming plane electron wave is modulated by the atomic potential only by a phase shift and the amplitude remains constant, which is the so-called phase object approximation (POA) [Thust, 2007]. Further, the specimen is approximated by a three-dimensional slice with the thickness d , where the electron wave is diffracted only at the exit plane at a two-dimensional potential $V_p(x, y)$, which results from the projection

of the potential $V(r)$ into the exit plane with

$$V(r) = \frac{8\pi^2 m}{h^2} e\phi. \quad (3.14)$$

The incident plane electron wave is described by $\Psi_0(\mathbf{r}) = e^{ik_0 \mathbf{r}}$, which is propagating in z -direction with the wave vector \mathbf{k}_0 of the length $k_0 = 2\pi/\lambda$. Here, symbols printed in bold denote three-dimensional vectors. At $z = 0$ the wave has the value 1 and after passing the specimen at the position (x, y, d) the exit wave function (EWF) is:

$$\Psi(x, y, d) = e^{-i\sigma V_p(x,y)d} \Psi_0(\mathbf{r}) =: \Psi_{POA}(x, y, d) \quad (3.15)$$

with $\sigma = \frac{2\pi}{h^2} m e \lambda (1 + \frac{E}{m_e c^2})$. The measurable intensity $I = |\Psi(x, y, T)|^2 = 1$ of this EWF would not contain any information about the specimen, and obviously, a more elaborate model is required.

In the multislice algorithm, the specimen is not approximated by only one slice but is subdivided into many slices with a thickness δz corresponding to atomic planes. The crystal potential in each slice is projected into the x - y -exit plane of each slice. An incoming electron wave is then diffracted at each two-dimensional projected potential $V_p(x, y, \delta z)$. In the volume between these potentials, no interaction takes place and the electron wave propagates freely through vacuum over the distance δz . This is described by the vacuum propagator:

$$p(x, y, \delta z) = e^{-i\sigma \delta z \nabla_{xy}^2}, \quad (3.16)$$

also known as Fresnel propagator, where ∇_{xy} is the Nabla operator with respect to the x - and y -direction. Hence, the electron wave function after passing a slice with the projected potential $V_p(x, y, \delta z)$ is given by [Kilaas, 2011]:

$$\Psi(x, y, z + \delta z) = e^{-i\sigma \delta z \nabla_{xy}^2} \otimes \left(e^{-i\sigma V_p(x,y,\delta z) \delta z} \Psi_0(x, y, z) \right) \quad (3.17)$$

$$\equiv p(x, y, \delta z) \otimes \Psi_{POA}(\mathbf{r}, \delta z). \quad (3.18)$$

This equation can be applied slice by slice until the end of the specimen is reached. The exit wave function of one slice is the entrance wave function for the next one. It can be shown, that this multislice method converges to the analytical solution of the Schrödinger equation for the theoretically extreme case of $\delta z \rightarrow 0$. However, the slice thickness should not fall below 1 Å in practice. Equation 3.18 can easily be solved in Fourier space, where

the convolution transforms into a multiplication [Ishizuka and Uyeda, 1977]:

$$FT[\psi(x, y, z + \delta z)] = FT[p(x, y, \delta z)] \cdot FT[\Psi_{POA}(\mathbf{r}, \delta z)] \quad (3.19)$$

$$\psi(\mathbf{k}, z + \delta z) = e^{-i\pi \lambda \delta z \mathbf{k}^2} \psi_{POA}(\mathbf{k}, z, \delta z) \quad (3.20)$$

$$\equiv p(\mathbf{k}, \delta z) \psi_{POA}(\mathbf{k}, z, \delta z), \quad (3.21)$$

where \mathbf{k} is the reciprocal scattering vector in Fourier Space in the x - y -plane.

The atomic potential $\phi(r)$ used in Equation 3.13 can be expressed as a Fourier series [Humphreys, 1979]:

$$\phi(r) = \sum_g \phi_g e^{2\pi i \mathbf{g} \cdot \mathbf{r}}, \quad (3.22)$$

where \mathbf{g} is a vector in reciprocal space. The Fourier coefficients ϕ_g are given by:

$$\phi_g = \frac{1}{V_s} \int_{\text{specimen}} dr \phi(r) e^{-2\pi i \mathbf{g} \cdot \mathbf{r}}, \quad (3.23)$$

where V_s is the volume of the entire specimen. These coefficients are exactly related to structure amplitudes for electrons as determined from the first Born approximation. They can be calculated using the theoretical free-atom scattering factors as an approximation ignoring any solid-state bonding effects. Doyle and Turner [1968] have used the relativistic Hartree-Fock theory and parameterized free-atom values, which can be found in various tables and are widely used by most HRTEM image simulation programs.

In order to take into account the thermal excitation of the atoms, an additional term, $\exp(-B\mathbf{g}/4\pi)$, is included in the Fourier coefficients of the potential. Here, B is the temperature dependent Debye-Waller factor, which is tabulated for most solids over a wide range of temperatures [Peng et al., 1996]. It is related to the mean square thermal displacement u of an atom from its equilibrium position:

$$B = 8\pi^2 \langle u^2 \rangle, \quad (3.24)$$

where $\langle \dots \rangle$ denotes the thermal average.

For this work, HRTEM contrast simulations have been performed using the commercial software MacTempas from Total Resolution, written by Kilaas [2011]. It offers the advantage of simulating non-periodic structures with arbitrary arrangements of atoms. After calculating the EWF following the multislice algorithm according to Equation 3.18 the software generates HRTEM contrast images in dependence of the given microscope parameters. The resolution of the image is mainly governed by the point spread function

$h(\mathbf{r})$, which describes the ability of the microscope to image one point of the object into the image plane. This transfer of the EWF is erroneous due to lens aberrations and the partial spatial and temporal coherence of the electron beam. In real space, the wave function transferred by the microscope to the image plane is given by:

$$\Psi_I(\mathbf{r}) = \Psi(\mathbf{r}) \otimes H(\mathbf{r}). \quad (3.25)$$

In Fourier space one gets;

$$\psi_I(\mathbf{k}) = \psi(\mathbf{k}) \cdot h(\mathbf{k}), \quad (3.26)$$

where $h(\mathbf{k})$ is the so-called modulation transfer function (MTF), which is the Fourier transform of $H(\mathbf{r})$. It is given by the aberration function $\chi(\mathbf{k})$ according to:

$$h(\mathbf{k}) = e^{-i\chi(\mathbf{k})} \quad \text{with} \quad \chi(\mathbf{k}) = \pi(\Delta f \lambda \mathbf{k}^2 + \frac{1}{2} C_S \lambda^3 \mathbf{k}^4), \quad (3.27)$$

where Δf is the defocus and C_S is the coefficient of the spherical aberration [Kirkland, 2010, S .18]. Many other lens aberrations contribute to the aberration function, and they can also be taken into account by the software MacTempas used for the HRTEM contrast simulation in this work. The final image intensity $I(\mathbf{r})$ that can be acquired with the CCD camera in the image plane of a TEM is given by the square of the absolute value of the electron wave function:

$$I(\mathbf{r}) \sim |\Psi_I(\mathbf{r})|^2 = |FT^{-1}[\psi(\mathbf{k}) \cdot h(\mathbf{k})]|^2. \quad (3.28)$$

In the approximation of linear imaging, which holds for very thin specimens with light elements, and which is used for this work, where Mg is the heaviest element, the image intensity is simplified in Fourier space according to [Thust, 2007, S. C2.13]:

$$I_L(\mathbf{k} \neq 0) = \psi^*(0) \psi(\mathbf{k}) + \psi(0) \psi^*(-\mathbf{k}). \quad (3.29)$$

HRTEM images calculated in this way agree qualitatively very well with experimental ones. However, the contrast of experimental images is usually too low by a factor of roughly 3 compared to simulated ones, which is known as the so-called Stobbs-factor problem [Hýtch and Stobbs, 1994]. There are various possible explanations for this discrepancy and it is still a subject of discussion. It is meanwhile common belief, that the MTF of the CCD camera largely contributes to the Stobbs factor. Therefore, for this work, the MTF was measured for the CCD camera Gatan US1000, which is used in the FEI Titan³ 80-300, using the aperture method of Nakashima and Johnson [2003]. The aperture MTF agrees

very well with holographic measurements and these two methods are believed to be the most accurate [Boothroyd et al., 2013]. The simulated HRTEM contrast images presented in Section 4.6 are firstly superimposed by a Gaussian noise with a standard deviation of 3%. Secondly, they are convoluted with the measured MTF of the CCD camera. By this, more realistic contrast images can be obtained from the multislice simulations.

4. Electron Beam induced Dehydrogenation of MgH₂

In this chapter, a detailed quantitative analysis of the electron beam induced dehydrogenation of MgH₂ by VEELS under low dose conditions is provided. After a microscopic description of the thermally induced dehydrogenation of MgH₂ in Section 4.1, the methodology of the determination of characteristic electron doses for the quantification of the electron beam induced dehydrogenation is explained in Section 4.2. The beam damage mechanism and the dependence of the dehydrogenation on the specimen thickness are quantitatively discussed in Sections 4.3 and 4.4, respectively, and concluded in Section 4.5. The electron beam induced decomposition can be prevented by performing the TEM analysis at an elevated hydrogen back pressure rather than under vacuum. In Section 4.6, the feasibility of HRTEM investigations at ambient hydrogen pressure is studied theoretically by means of multislice simulations. Here, Mg and its hydride phase serve as model system.

Most of the following chapter has already been published in [Surrey et al., 2016c].

4.1. Microscopic Model of Hydrogen Release

Danaie et al. [2010] provided a fairly consistent phenomenology for the thermally induced dehydrogenation of MgH₂ based on their energy filtered TEM (EFTEM) observations of ball milled MgH₂, which was stabilized in the TEM using a cryogenic sample holder cooled to 90 K. They could rule out a model which assumes that the desorption starts at the surface, forms a growing metal shell and a shrinking hydride core. Instead, the heterogeneous nucleation of the Mg phase is difficult and proceeds only on exposed surfaces and on high-energy defects. Once a nucleus is formed, the metallic phase grows fast, because hydrogen diffusion is fast along grain boundaries. This leads to a grain by grain dehydrogenation. The reaction is kinetically limited by solid-state diffusion of ions or atoms towards or away from the reaction front. However, as the authors also pointed out, this applies only to the elevated-temperature driven dehydrogenation, whereas the process is different for the electron beam induced dehydrogenation at room temperature, which

will be discussed in the following sections.

4.2. Determination of Characteristic Electron Doses

A typical nanocrystalline MgH_2 particle studied by VEELS is shown in Figure 4.1(a). It is located at the edge of the holey carbon substrate. Such agglomerations of MgH_2 nanocrystals are typically 100 to 600 nm in diameter. Due to the impact of the electron beam the presented particle is already fully dehydrogenated. It is not possible to acquire a TEM bright field image of the ball milled MgH_2 in the hydrogenated phase with the CCD camera even at low magnifications, since the electron dose, that is needed for an acquisition with the CCD with a decent signal-to-noise ratio, already causes massive dehydrogenation. The red, 36 nm \times 36 nm large square in Figure 4.1(a) depicts the area of the specimens from where the VEEL spectra are acquired with the CCD camera of the energy filter system under low dose conditions.

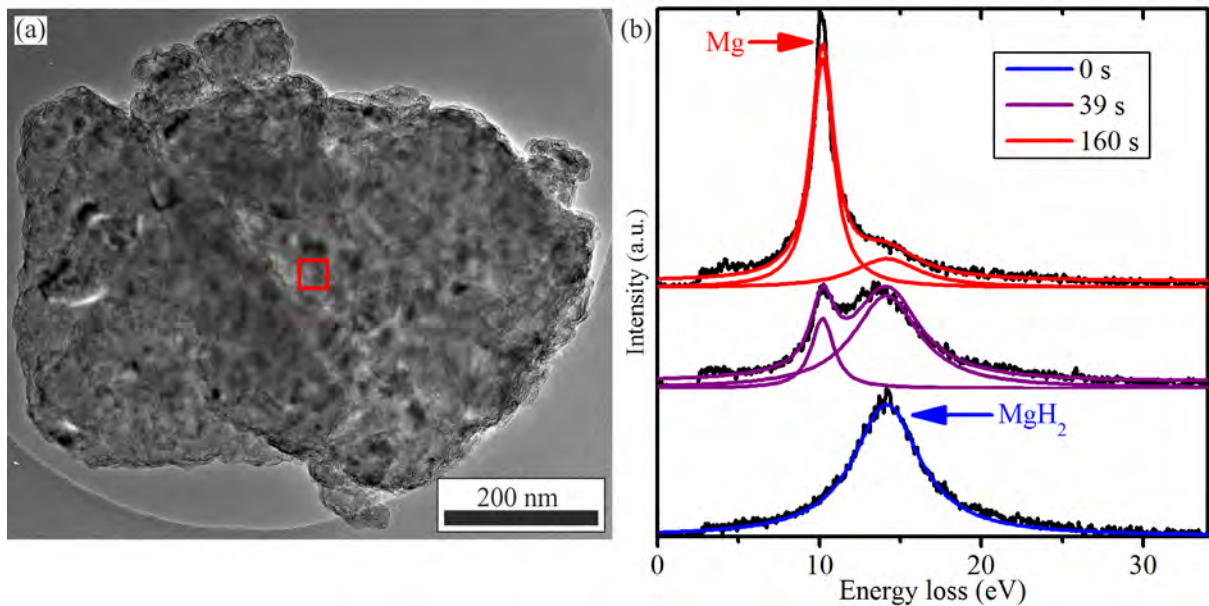


Figure 4.1. (a) TEM bright field image of a typical ball milled MgH_2 particle, which is already dehydrogenated due to the electron beam. The red square indicates an area of 36 nm \times 36 nm of the particle, from where the VEEL spectra are acquired with the CCD camera of the energy filter system. (b) Three of a series of 106 VEEL spectra acquired from a MgH_2 particle: blue at the beginning of the electron beam exposure, purple after 39 s, and red after 160 s of continuous irradiation. The MgH_2 plasmon at 14.1 eV decreases, while the Mg plasmon at 10.1 eV arises. After roughly 3 min, all hydrogen has left the specimen. The fitted Lorentz functions describing the respective plasmon contributions are overlaid on the experimental data. The adjusted coefficients of determination, \bar{R}^2 , describing the goodness of the fits are 0.99, 0.97 and 0.98 for the fits in blue, purple and red, respectively. The used current density is 818 e⁻/nm²/s at an accelerating voltage of 300 kV.

As examples, Figure 4.1(b) shows three VEEL spectra of a typical dehydrogenation of a nanocrystalline MgH_2 particle irradiated with 300 keV electrons and a current density of $818 \text{ e}^-/\text{nm}^2/\text{s}$. The initial broad MgH_2 plasmon at 14.1 eV starts to decrease in intensity, as soon as the specimen is exposed to the electron beam. At an intermediate state after 39 s, the additional sharp plasmon peak of metallic Mg at 10.1 eV is observable. After approximately 3 min, most of the hydrogen has left the specimen, and the spectrum in Figure 4.1(b) is dominated by the Mg plasmon. The amount of each phase present in the specimen is reflected by the area under the respective plasmon peak. There is no overlaid carbon plasmon, which would be centered around 20–34 eV, since the VEEL spectra of the MgH_2 particle are acquired from an area above a hole of the carbon substrate. Due to the use of the vacuum transfer holder the oxidation of the specimen can be minimized, which can be seen from the lack of any MgO volume plasmon at around 23 eV [Danaie et al., 2010]. The signals in the spectra only originate from the single inelastic scattering by the Mg and MgH_2 volume plasmons, because the spectra are corrected for plural scattering by deconvolution with the Fourier-log method, which also removes the zero-loss beam. The sum of two Lorentz functions (cf. Equation 3.8) describing the two plasmons plus an almost constant offset can be fitted to the spectra very accurately. The adjusted coefficients of determination, \bar{R}^2 , describing the goodness of the fits are generally around 0.95 or better. Only for the intermediate states, where both plasmons are present, the fit quality is occasionally worse with $\bar{R}^2 = 0.8 - 0.9$. This is mostly due to some intensity in between the plasmon peaks, because the MgH_2 plasmon not only decreases in intensity but also shifts to lower energies. The reason for this is the reduction of the density of valence electrons upon dehydrogenation, which leads to the reduced plasmon energy. If also the plasmon energies are fitted in order to take this reduction into account, the fit will not always converge. Therefore this shift in plasmon energy cannot be properly accounted for by the fitting procedure, and the plasmon energies are fixed at the cost of a slightly worse fit quality. The resulting Lorentz functions are overlaid for both plasmons on the experimental data in Figure 4.1(b).

For all spectra of the series the fitted areas of the Lorentz function corresponding to the MgH_2 plasmon are normalized to their initial value and plotted as function of time in Figure 4.2. The monotonic decay can be very precisely described by an exponential function $\exp -t/\tau_e$, where t is the time and $\tau_e = 108 \text{ s}$ is the so-called characteristic time, after which only $1/e = 37\%$ of the initial material is left. By multiplying τ_e with the current density j , the characteristic electron dose $D_e = \tau_e j = 8.8 \cdot 10^4 \text{ e}^-/\text{nm}^2$ can be determined.

This evaluation is carried out for 14 likewise conducted experiments of electron beam

Figure 4.2 The normalized area of the MgH_2 plasmon is plotted over time. An exponential decay function is fitted to the normalized areas (solid green line).

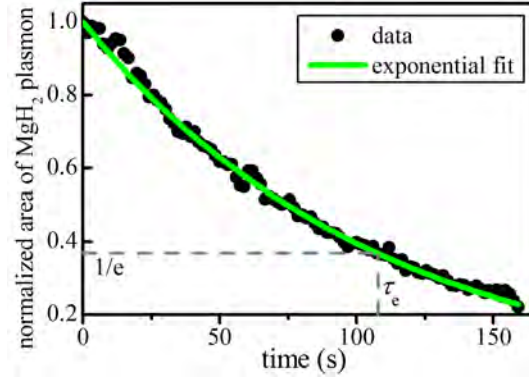
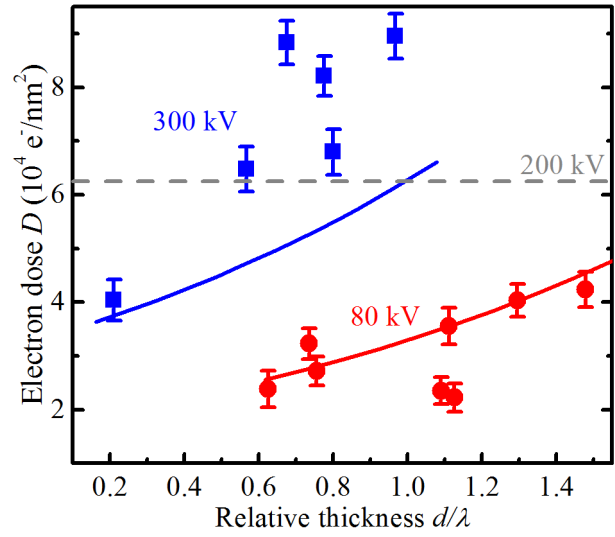


Figure 4.3 Deduced electron doses for accelerating voltages of 80 kV (red) and 300 kV (blue). The characteristic dose determined from the electron diffraction data published by Danaie et al. [2008] at 200 kV is shown as dashed gray horizontal line, since the relative thickness is not known. The red and blue solid lines are calculated characteristic doses for 80 kV and 300 kV, respectively, assuming single inelastic scattering and a protection factor of 4.



induced dehydrogenations at accelerating voltages of both 80 and 300 kV. The resulting fit values for the plasmon energies E_i and widths w_i are in the range of $E_1 = 9.99 - 10.37$ eV and $w_1 = 0.84 - 2.17$ eV for Mg and $E_2 = 13.79 - 14.47$ eV and $w_2 = 4.58 - 6.31$ eV for MgH_2 . For each investigated MgH_2 particle its relative thickness d/λ at the area, from which the VEEL spectra are acquired, is determined from these spectra according to Equation 3.12. Due to the large number of spectra for each particle this quantity can be calculated with a small uncertainty. All likewise deduced characteristic electron doses are plotted as function of the relative thickness in Figure 4.3 as solid symbols. It is apparent from this figure that the characteristic doses measured at 300 kV are generally higher than those measured at 80 kV. Furthermore, there is a clear tendency for the characteristic dose to increase with the relative thickness of the particle, though some measured values deviate from this trend.

The characteristic electron doses shown in Figure 4.3 are compared with the value, that was determined from data published by Danaie et al. [2010] for a comparable dehydrogenation experiment on ball milled MgH_2 at an accelerating voltage of 200 kV. For this,

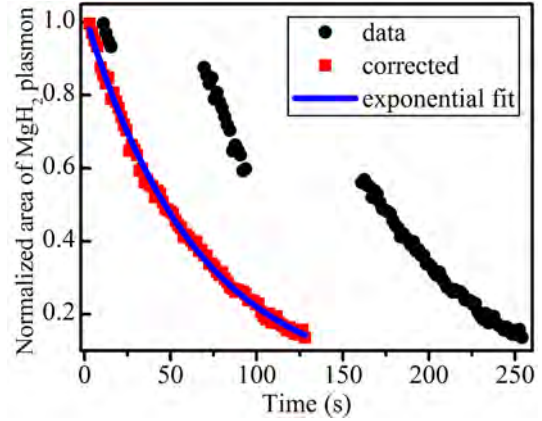
the relative thickness is unknown, but the characteristic electron dose is in good agreement with our results and fits in the range of doses measured for 80 and 300 kV.

4.3. Beam Damage Mechanism

MgH₂ is unstable in the high vacuum of a TEM (ca. 10⁻⁸ mbar) at room temperature. The equilibrium pressure for room temperature can be calculated using the Van't Hoff Equation 2.5 and the standard enthalpy of formation of -75 kJ/mol and is in the order of 10⁻⁴ mbar. The fact that the hydride phase can be detected in the TEM at all can be explained by high kinetic barriers for the dehydrogenation. This is mainly due to the difficult nucleation of Mg, which applies to elevated temperatures (cf. discussion in Section 4.1), and is even more difficult at room temperature. However, the electron beam induces a constant source of nuclei forming homogeneously and statistically distributed throughout the specimen. The diffusion of hydrogen through the particles into vacuum is very fast along the twinning planes, which result from ball milling [Danaie et al., 2010]. Another diffusion path is through the voids [Mooij and Dam, 2013], that are forming upon dehydrogenation, because of a shrinkage of the material by roughly 25%. Therefore, hydrogen diffusion away from a growing Mg nucleus cannot limit the dehydrogenation. However, without the impact of the electron beam we do not observe a further decrease in the amount of the hydride. As soon as the electron beam is switched off the dehydrogenation stops. This is illustrated in Figure 4.4, where the temporal evolution of a dehydrogenation is shown, which was interrupted twice for 55s and 68s by blanking the electron beam. After removing these dark times, the corrected course of the data points follows again a single exponential decay. This clearly shows that spontaneous dehydrogenation does not occur. Since, under the conditions in the TEM, MgH₂ is not the thermodynamic equilibrium phase, this immediately confirms the metastability of the hydride phase and the kinetic impediment of a relaxation into the metallic Mg ground state. The origin of the kinetic barrier involved, however, cannot be identified from the present experiments.

The question of the mechanism of the electron beam damage could be answered by firstly considering beam heating. According to Egerton and Malac [Egerton et al., 2004], however, the expected temperature increase for a typical TEM experiment is only 1 K or even less. Since the beam current for the here discussed dehydrogenation experiments is uncommonly small, no significant beam heating can be expected. Another well-known damage mechanism is atomic displacement or knock-on damage, which can also lead to sputtering. Here, the electron beam damage is generally larger for higher incident electron energies [Egerton et al., 2004]. This, however, is in clear contrast to our experimental

Figure 4.4 The normalized area of the MgH₂ plasmon is plotted as function of time for a dehydrogenation that was stopped twice by blanking the electron beam. The original data (black dots) is corrected for the interruptions (red squares) and then again follows a pure exponential decay (blue line).



observations, where the characteristic electron doses are higher at 300 keV than at 80 keV, i.e. the hydride can withstand a higher dose and there is less damage at 300 keV. This result rather clearly indicates that the dominating electron beam damage to the hydride is radiolysis [Schober and Chason, 1982], because it scales with the scattering cross section, which is higher for 80 keV electrons [Egerton et al., 2004]. Here, the high energy electrons disturb the ionic metal–hydrogen bond. Since MgH₂ is unstable in vacuum, all released hydrogen desorbs instantaneously from the specimen.

4.4. Thickness Dependence of the Electron Dose

For the dehydrogenation of MgH₂, some energy transfer is needed to overcome the kinetic barrier given by the activation energy E_A of 127 kJ/mol for dehydrogenation [Danaie et al., 2010]. In units of electronvolts this converts to 1.3 eV per MgH₂ *molecule*. This means that in principle every inelastically scattering electron, which excites a MgH₂ plasmon, can cause the dehydrogenation of a MgH₂ *molecule*. It is well possible that the cross sections for radiolysis and the inelastic scattering are equal, i.e. $\sigma_{\text{rad}} = \sigma_{\text{in}} = \sigma$. To validate this assumption the cross section for the inelastic scattering of an incident high energy electron by a plasmon has to be calculated. The energy-differential cross section of this process is given by Equation 3.9. The numerical integration over the energy loss is performed using the software Mathematica to obtain the total inelastic scattering cross section σ for 80 and 300 keV electrons. An energy loss of 50 eV is set as the upper bound of integration.

According to Poisson statistics, the probability P_n for n -fold inelastic scattering is given by Equation A.1. Each scattering event causes the breaking of a Mg–H bond. Therefore, the rate of dehydrogenation, i.e. the change of the number of Mg–H bonds as function of

time is given by

$$\frac{dN(t)}{dt} = - \sum_{n=0}^{\infty} nP_n I, \quad (4.1)$$

where N is the number of Mg–H bonds at time t and I is the electron beam current. It can be shown that this expression simplifies to (see Appendix)

$$\frac{dN(t)}{dt} = -3/2N\sigma j. \quad (4.2)$$

Here, j is the current density. Integration of Equation 4.2 leads to

$$N(t) = N_0 \exp(-j\sigma t), \quad (4.3)$$

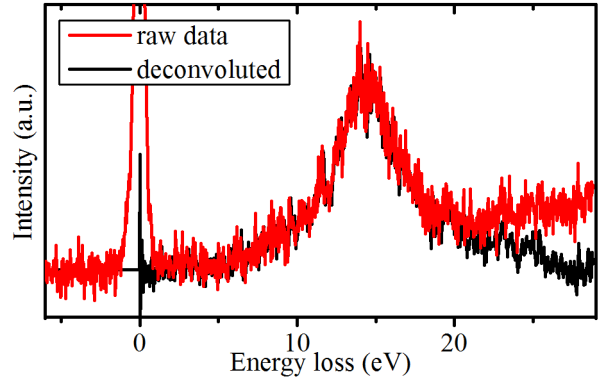
where N_0 is the initial amount of Mg–H bonds. This relation does describe the experimentally observed decay of the MgH₂ plasmon, but it *cannot* explain the observed thickness dependence of the characteristic electron dose as shown in Figure 4.3: Thinner particles show smaller characteristic electron doses, i.e. they dehydrogenate faster than thicker particles.

Equation 4.3 does not describe the experimentally determined thickness dependence, because Equation 4.1 is valid for thick specimens, where plural inelastic scattering can take place. In contrast the studied MgH₂ particles are relatively thin, so that predominantly single scattering occurs. An example VEEL spectrum of a relatively thick particle with $d/\lambda = 1.5$ is displayed in Figure 4.5. Mainly the single loss plasmon peak is present and only a small contribution from plural scattering at higher energies can be observed, which confirms that mainly single scattering occurs. Therefore, the sum in Equation 4.1 is terminated at $n = 1$ and $N(t)$ is given by the differential equation

$$\begin{aligned} \frac{dN(t)}{dt} &= -d/\lambda \exp(-d/\lambda)I \\ &= -3/2dN(t)/V\sigma \exp(-3/2dN(t)/V\sigma)jA, \end{aligned} \quad (4.4)$$

where the mean free path is written using $N(t)$ as $1/\lambda = n_a\sigma = 3/2N(t)/V\sigma$ (see Section A.2 in the Appendix). The particle morphology is approximated by a sphere of diameter d with the volume V and the projected area A . Using the initial condition $N(t = 0) = N_0 = 2\rho N_A/MV$ the differential equation 4.4 can be solved numerically and the characteristic time τ_e , for which $N(\tau_e) = N_0/e$, can be determined. In this way, the characteristic electron doses $D_e = \tau_e j$ are calculate for different thicknesses at electron energies of 80 and 300 keV using the software package Mathematica. In Figure 4.3 the

Figure 4.5 VEEL spectrum of the thickest MgH_2 particle that is investigated with a relative thickness of $d/\lambda = 1.5$ at the beginning of the dehydrogenation acquired at 80 kV. The spectrum is dominated by single scattering with the plasmon peak centered around 14.5 eV. The raw data (in red) and the deconvoluted spectrum (in black), where the small contribution from plural scattering is removed, are plotted.



calculated electron doses are compared with the experimental data. There is a good qualitative agreement between both, however, they differ by a factor of roughly 4. The good agreement between experiment and theory suggests (although it does not prove) that one plasmonic excitation per molecule is responsible for the radiolytic damage, i.e. the cross sections for radiolysis and inelastic scattering by a plasmon are indeed the same [Egerton et al., 2004].

But based on the inelastic scattering, the effective electron dose should be four times smaller than our experimental results, meaning that the hydride should be even more sensitive to the electron beam. This discrepancy can be explained by the presence of a thin nanocrystalline or amorphous MgO and $\text{Mg}(\text{OH})_x$ surface layer (3-4 nm) surrounding the MgH_2 particles, the formation of which cannot be completely avoided. Despite the usage of the vacuum transfer holder, such a thin oxide layer may have already formed during sample handling under argon inside the glove box [Friedrichs et al., 2006]. This oxide layer could act as a diffusion barrier for the hydrogen and, therefore, slow down the dehydrogenation. Such a protective effect is also known from carbon or metal coatings for organic or low Z materials, where protection factors of up to 6 are reported [Egerton et al., 2004].

Therefore, the calculated characteristic electron doses displayed in Figure 4.3 are multiplied by this protection factor of 4. As a consequence, the values also agree quantitatively very well at 80 keV. For 300 keV, the data scattering is stronger. This may be due to drift or rotation of the particles during the dehydrogenation, which would mean that during the measurement, the region of the particle for the acquisition of the VEEL spectra may change. This could result in an inaccurate thickness measurement and an erroneous measurement of the actual current density due to an inhomogeneous illumination. Furthermore, the experimental electron doses at 300 kV are still larger than the theoretical values which are already corrected by the protection factor and an even larger factor would have to be assumed, which does not make sense, because the diffusion of hydrogen through

the oxide layer should not depend on the electron energy.

Another possible interpretation, however, is that the cross sections for inelastic scattering and radiolysis are *not* equal and the difference further depends on the electron energy. A third explanation can be found considering that also in cryo TEM studies, the radiolytic decomposition of MgH_2 has been reported, although on a longer time scale of up to 15 min [Danaie et al., 2010]. This is probably due to the fact that it is more difficult to overcome the kinetic barrier at lower temperatures. At a temperature above room temperature, however, the experimental doses might coincide with the calculated ones, because the kinetic barrier would no longer slow down the dehydrogenation. This would prove that both cross sections for radiolysis and inelastic scattering are indeed equal. However, at a higher temperature, MgH_2 would easily become unstable, and spontaneous and temperature induced dehydrogenation would occur in addition to the electron beam induced dehydrogenation.

In any case, the here developed methodology can show that the cross sections have at least the same order of magnitude and that predominantly single scattering takes place, which explains the thickness dependence of the characteristic electron doses.

Danaie et al. [2010] observed strong evidence of the core-shell morphology for the electron beam induced dehydrogenation of MgH_2 at room temperature using EFTEM. Metallic Mg started to grow at the surface and forms a shell around the shrinking hydride core. This observation can be well explained by the theory based on single scattering as described above. The particles studied by Danaie et al. [2010] show sizes comparable to the particles studied by us, because the VEEL spectrum published in that reference also shows just a minor plural scattering contribution and the published EFTEM images also reveal a cross section of roughly 200–400 nm. At the shell, where the particle is thinner (in the direction of the electron beam), the dehydrogenation happens faster than in the thicker core, where too many Mg–H bonds are present to be dehydrogenated with the same rate as in the thinner regions just by single scattering. This again shows, that the diffusion of hydrogen does not play a role for this process and does not limit the speed of the dehydrogenation.

From the fact that the electron beam induced dehydrogenation goes along with an excitation of plasmons, it can be assumed that by virtue of the electrical field of the incident electron the metastable hydride becomes locally unstable. From the similarity or even equality of the cross sections, one can further conclude that not the electric field of the incident electron itself but rather the electric field of the excited plasmon causes the radiolysis. Other inelastic processes such as inner shell ionizations or secondary electron emission have cross sections which are several orders of magnitude smaller than radiolysis [Williams and Carter, 2009][p.54].

4.5. Conclusions for the Electron Beam Induced Dehydrogenation

The measured characteristic electron doses for the dehydrogenation of MgH₂ are in the order of $10^4 \text{ e}^-/\text{nm}^2$. For a typical TEM investigation, the electron dose is at least two orders of magnitude larger, especially for analytical and high resolution studies. Hence, these types of analyses can only be conducted for the dehydrogenated state and not for the hydride phase. This is in particular problematic for very thin and nanostructured specimens. This problem is not only relevant for MgH₂, but applies also to other hydrides such as LiBH₄ [House et al., 2014], AlH₃ [Ikeda et al., 2009], LiAlH₄, NaBH₄ [Herley and Jones, 1986], NaAlH₄ [Egerton et al., 1987] or LiH [Deprez et al., 2010]. The major drawback is, that upon dehydrogenation the specimen undergoes significant structural and morphological changes, that may also include phase separation, and any information gathered for the dehydrogenated state cannot be applied to the original hydride phase.

A solution might be the cryogenic cooling of the specimen, because at 77 K the equilibrium pressure of MgH₂ is reduced to 10^{-41} mbar, which is well below the hydrogen partial pressure of 10^{-10} mbar in the TEM. As a consequence, the hydride should be stable under these conditions. However, also in cryo TEM studies, the radiolytic decomposition of MgH₂ has been reported, although on a longer time scale of up to 15 min [Danaie et al., 2010]. Another possibility might be the usage of a coating with a thickness of tens of nm, that on the one hand would lead to a higher protection factor, but on the other hand would alter the properties of the specimen and reduce the TEM image contrast. A more promising approach is performing the TEM analysis at an elevated hydrogen back pressure rather than under vacuum to stabilize the hydride phase. Hydrogen pressures of up to 4.5 bar can be realized with recently developed closed environmental cell TEM holders for in-situ experiments. Such an experimental setup has already been used by Yokosawa et al. [2012] for studying the (de)hydrogenation of nanostructured Pd.

4.6. Multislice Simulations for ETEM Studies

The objective of this section is to study the feasibility of HRTEM investigations of light weight metals and metal hydrides in a windowed environmental cell at ambient hydrogen pressure by means of multislice HRTEM contrast simulations. Here, Mg and its hydride phase serve as model system. The dependence of both the spatial resolution and the HRTEM image contrast on parameters such as the defocus, the metal/hydride thickness, and the hydrogen pressure is analyzed in order to explore the possibilities and limitations of

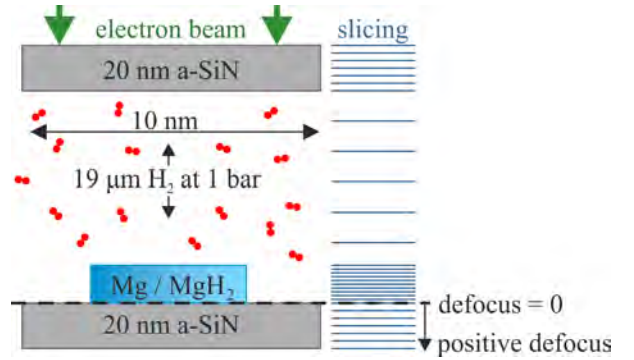
in-situ experiments with such a setup. These simulations are considered valuable in order to pre-evaluate future experimental studies. In this section, it is aimed at simulating the HRTEM image formation in an environmental cell under as realistic as possible conditions. Therefore and in contrast, e.g. to the approach of Yoshida and Takeda [2005], not only the interaction of the electron beam with the windows of the ETEM cell are taken into account, but also its propagation along the whole thickness of the gas layer in beam direction is calculated by using slices of sufficient individual thickness.

4.6.1. Methods of the Multislice Simulations

All multislice simulations are conducted with the MacTempas software package (Version 2.4.27) [Kilaas, 2016] using the Gerberg-Saxton algorithm [Gerchberg and Saxton, 1972]. The nanoreactor is implemented in a supercell with a basal area of $10\text{ nm} \times 10\text{ nm}$ perpendicular to the electron beam as displayed in Figure 4.6. In beam direction, it consists of two 20 nm thick electron transparent windows of amorphous SiN at the top and at the bottom, a $19\text{ }\mu\text{m}$ thick hydrogen gas volume in between the windows and crystalline thin films of Mg or MgH_2 positioned on top of the bottom window. The Mg and MgH_2 crystals were modeled using the CrystalKit software [Kilaas, 2016], while the amorphous SiN windows were modeled by randomly distributing Si and Ni atoms with a ratio of 3:4 and a density of 3.2 g/cm^3 in a layer with a thickness of 20 nm. Even though this simple model does not describe the atomic arrangement very accurately, it is known that the structural details of amorphous materials have no big influence on HRTEM images [Boothroyd, 2000]. Therefore, the random arrangement of atoms provides a good approximation for the purpose of the present study. In the same manner, the hydrogen atoms of the gas volume are randomly distributed as molecules with a random orientation. The density of the hydrogen gas is set for each given pressure at room temperature according to the ideal gas law. While the slice thickness is chosen to contain only a single layer of scatterers within the $\text{Mg}(\text{H}_2)$ nanocrystal, it is increased to 1 nm and 100 nm in the SiN windows and the hydrogen containing volume, respectively.

For the contrast simulation, linear imaging with a maximal scattering vector $g_{\text{max}} = 2\text{ \AA}^{-1}$ is used, since only relatively light elements are included, where non-linear effects are expected to be negligible. Further imaging parameters are chosen to model the performance of a state-of-the-art aberration corrected TEM at 300 kV, namely a FEI Titan³ 80-300, for negative spherical aberration imaging [Jia et al., 2003]. The parameters are as follows: spherical aberration = $-10\text{ }\mu\text{m}$, chromatic aberration = 1 mm, convergence angle = 0.25 mrad, spread of defocus = 2.7 nm, objective aperture radius = 1.5 \AA^{-1} , imaginary

Figure 4.6 Schematic illustration of the modeled supercell representing the nanoreactor. The three different slicings with varying thicknesses for the respective sub-cells are indicated.



potentials with an imaginary part of 10 % of the real part. For Si, N, Mg and solid H atoms, a standard Debye-Waller factor of 0.5 \AA^2 is used, while for the gaseous hydrogen atoms, it is set to 0, because the Debye-Waller approximation can only be applied to solids. Yoshida and Takeda [2005] argued that a large number of independent scattering events with a single gas molecules take place during a typical recording time of approximately 1 s. For a single scattering event, a gas molecule can be considered as being at rest, i.e. frozen. Therefore, a Debye-Waller factor of 0 is reasonable. However, each incident electron encounters a different arrangement of gas molecules due to their high thermal velocity. As a consequence, a HRTEM image is statistically averaged over many molecule arrangements. Yoshida et al. took this into account by means of a frozen phonon-like approach and found that averaging over 10 arrangements is sufficient for the multislice simulation of HRTEM images of a specimen in an ethanol gas [Yoshida and Takeda, 2005]. In the present work, this averaging is found to not significantly influence the simulated contrasts, and accordingly, for all presented results a single, frozen arrangement of hydrogen molecules is assumed.

For an effective contrast simulation, the problem is divided in four sub-cells. In the first sub-cell, the scattering of a plane electron wave with the top SiN window is simulated resulting in a disturbed exit wave function at its bottom. This is used as the entrance wave function for the calculation of the scattering within the hydrogen gas in the second sub-cell. Again, this resulting exit wave serves as the entrance wave function for the third sub-cell containing the $Mg(H_2)$. In the last step the wave function exiting from the $Mg(H_2)$ layer is propagated through the SiN bottom window. This yields the exit wave function of the whole super-cell, which is finally back-propagated to the bottom of the $Mg(H_2)$ layer using the vacuum propagator

$$p(\mathbf{k}, \delta z) = e^{-i\pi \lambda \delta z \mathbf{k}^2}, \quad (4.5)$$

where λ is the electron wavelength, \mathbf{k} is the reciprocal scattering vector in Fourier Space in the x - y -plane, and $\delta z = -20 \text{ nm}$ is the back propagated distance, which is equal to the

thickness of the bottom window. This way, the bottom of the Mg(H₂) layer is simulated to be adjusted to the eucentric height of the microscope. This final exit wave function is then used for the calculation of the HRTEM contrast images at varying defocus.

The specimen can also be placed at the bottom of the top SiN window. However, this arrangement is computationally more expensive, because the propagation of the exit wave through the gas layer and the bottom window must be calculated for every thickness of the specimen, whereas for the positioning on the bottom window, the propagation of the electron wave through the top window and the gas layer has to be calculated only once and can then be used as the entrance wave for all specimen thicknesses. For the simulation of contrast images for the sample being attached at the top window, the exit wave function leaving the bottom window is propagated back by 19.02 μm . The resulting images are comparable to those obtained for placing the specimen at the bottom window with, however, a slightly lower contrast, that is found to be reduced by roughly 5 %. Therefore and in agreement with the illustration in Figure 4.6, the specimen is placed at the bottom window for all simulations presented in this section.

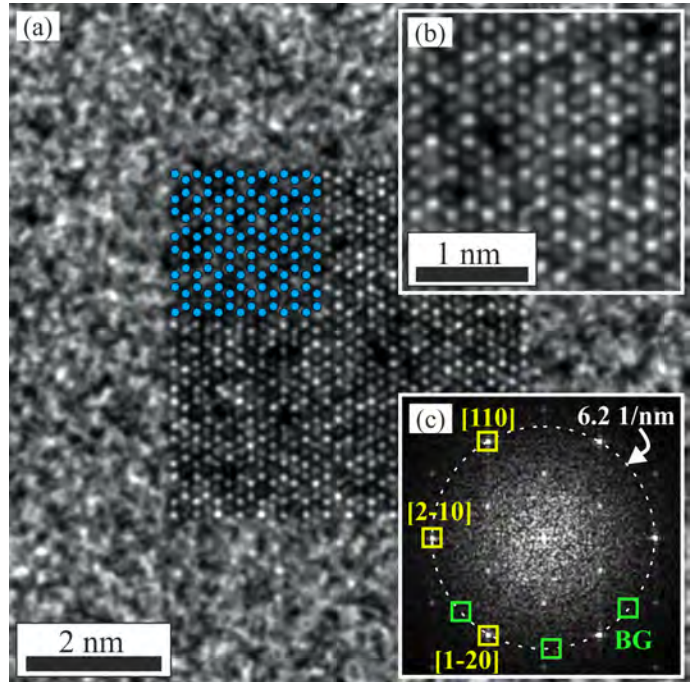
In order to obtain more realistic images, (i) Gaussian noise is added to the simulated images with a standard deviation of 3 %, and (ii) the images are convolved with the modulation transfer function (MTF) of the CCD camera. The MTF of the CCD camera (Gatan US1000) is measured using the aperture method of Nakashima and Johnson [2003]. The accordingly determined MTF agrees very well with holographic measurements and these two methods are considered to be the most accurate ones [Boothroyd et al., 2013].

The simulated images are then evaluated by determining the Weber contrast c of the main reflections from their Fast Fourier transforms (FFTs) according to $c_{hkl} = (I_{hkl} - I_{BG})/I_{BG}$, where I_{hkl} is the intensity of the respective Bragg reflection and I_{BG} is the background intensity in the close vicinity of these Bragg scattering vectors g_{hkl} , as it arises from the windows of the nanoreactor and the noise. The accordingly determined contrast is equivalent to a signal-to-noise ratio. For Mg, the [110], [2-10] and [1-20] reflections with $g = 6.2 \text{ nm}^{-1}$ are used, and for MgH₂, the [2-20] and [002] reflections at $g = 6.3 \text{ nm}^{-1}$ and $g = 6.6 \text{ nm}^{-1}$ are analyzed.

4.6.2. Results and Discussion of the Multislice Simulations

The simulated HRTEM image of the Mg crystal in [001] orientation, which is a typical growth orientation for thin films [Baldi et al., 2010], with a thickness of 17 nm and a defocus of 3 nm providing for optimal image contrast, is shown as an example in Figure 4.7(a). The atomic structure model of Mg is overlaid in blue in the top left of the crystal. The

Figure 4.7(a) Simulated HRTEM image of a 17 nm thick Mg crystal in [001] orientation inside the nanoreactor at an optimum defocus of 3 nm. The atomic structure of Mg is overlaid in the top left corner of the crystal. **(b)** Magnification of the central region of the Mg crystal shown in (a). **(c)** FFT of the image in (a). The Bragg reflections used for the determination of the Weber contrast are indicated by yellow squares, and the regions used for measuring the background (BG) intensities are marked by green squares. The dashed circle has a radius of 6.2 nm^{-1} .



inset in Figure 4.7(c) shows the FFT of the image. The Bragg reflections and background intensities used for determining the Weber contrast are indicated by yellow and green squares, respectively. At the chosen defocus, the highest contrast can be obtained for this thickness. Since the optimal defocus depends on the crystal thickness, the contrast map displayed in Figure 4.8 is generated. Here, the contrast is plotted for all crystal thicknesses up to 50 nm in steps of 5.2 \AA on the ordinate and defoci in the range from -20 nm to $+20 \text{ nm}$ in steps of 1 nm on the abscissa. Using this presentation a total of 3895 image simulations can be evaluated. It can be seen that the optimum defocus indicated by the dotted green line in Figure 4.8 decreases with an increasing crystal thickness. A slightly positive overfocus of a few nanometer generally yields the highest contrast, which is in good agreement with the Lichte defocus of least confusion [Lichte, 1991].

The dependence of the optimal contrast, i.e. at optimal defocus, of Mg inside the nanoreactor on the thickness is plotted in Figure 4.9. For comparison, the simulated contrast of freestanding Mg is also displayed. Placing the sample in the nanoreactor results in a mean contrast reduction by roughly a factor of 30. However, the contrast of Mg inside the nanoreactor is still high enough to resolve the crystalline structure, since it is still significantly higher than the maximum contrast of the background. Even for very thin Mg layers with thicknesses down to 2 nm, weak Bragg reflections are measurable in the FFT of the simulated images. However, in the real space images, the individual Mg atom columns cannot be resolved then. Only for contrast values of roughly 10, i.e. a Mg thickness of 5 nm, the Mg crystal lattice starts to become visible. For a large thickness

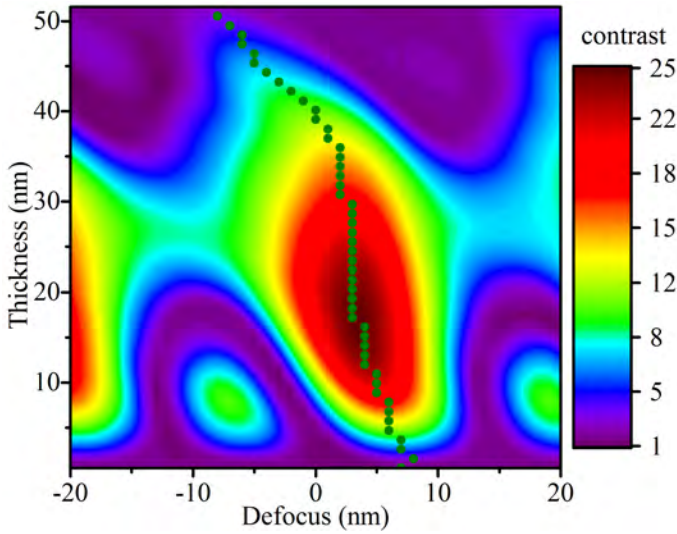


Figure 4.8 Contrast map of a Mg crystal in [001] orientation inside the nanoreactor showing the Weber contrast as function of the Mg thickness and the defocus. The optimum defocus is marked for all thicknesses by the green dots.

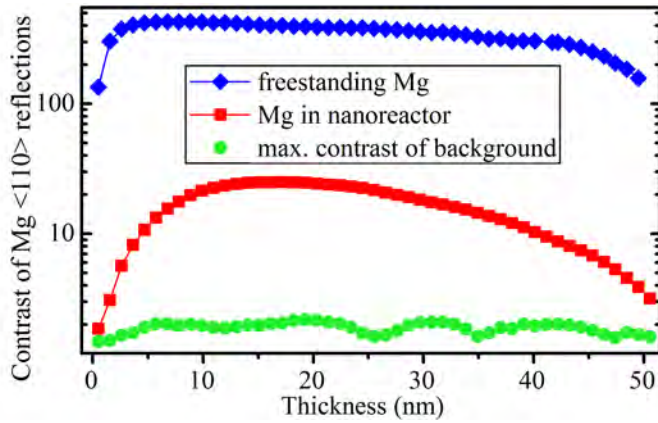


Figure 4.9 Contrast for freestanding Mg and Mg inside the nanoreactor at optimum defocus for different thicknesses. The nanoreactor leads to a mean contrast reduction by a factor of roughly 30, but the contrast is still higher than the background contrast allowing the Mg to be resolved by HRTEM.

of 50 nm the contrast is decreasing due to the Pendellösung behavior according to the channeling theory [Thust, 2007].

The contrast of a MgH_2 crystal in [110] orientation is simulated analogously. This orientation is chosen due to the orientation relation $\text{Mg}(001)[001]//\text{MgH}_2(110)[110]$ given by Fujii et al. [2002] for thin films. Therefore, one can assume that MgH_2 would form in this orientation upon hydrogenation of a Mg crystal in the nanoreactor as shown above. A simulated HRTEM image of MgH_2 inside the nanoreactor is shown as an example in Figure 4.10(a) for an optimal thickness of 12 nm and an optimal defocus of 2 nm. The atomic structure is again overlaid in the top left of the crystal. The Mg atom columns (blue) are clearly visible in the HRTEM image, whereas the H atom columns (orange) do not generate a visible contrast due to their small atomic number. The inset in Figure 4.10(c) shows the FFT of the HRTEM image. The [2-20] and [002] Bragg reflections and background intensities used for determining the Weber contrast are indicated by the yellow and green squares, respectively.

Figure 4.10(a) Simulated HRTEM image of a 12 nm thick MgH_2 crystal in [110] orientation inside the nanoreactor at a defocus of 2 nm. The atomic structure of MgH_2 is overlaid in the top left corner of the crystal. **(b)** Magnification of the central region of the MgH_2 crystal in (a). The atom columns of the (002) Mg lattice planes with a spacing of 1.51 Å are clearly distinguishable. **(c)** FFT of the image in (a). The Bragg reflections used for the determination of the Weber contrast are indicated by yellow squares and the regions for measuring the background (BG) intensities are marked by green squares. The MgH_2 [2-20] and [002] reflections are at $g = 6.3 \text{ nm}^{-1}$ and $g = 6.6 \text{ nm}^{-1}$, respectively.

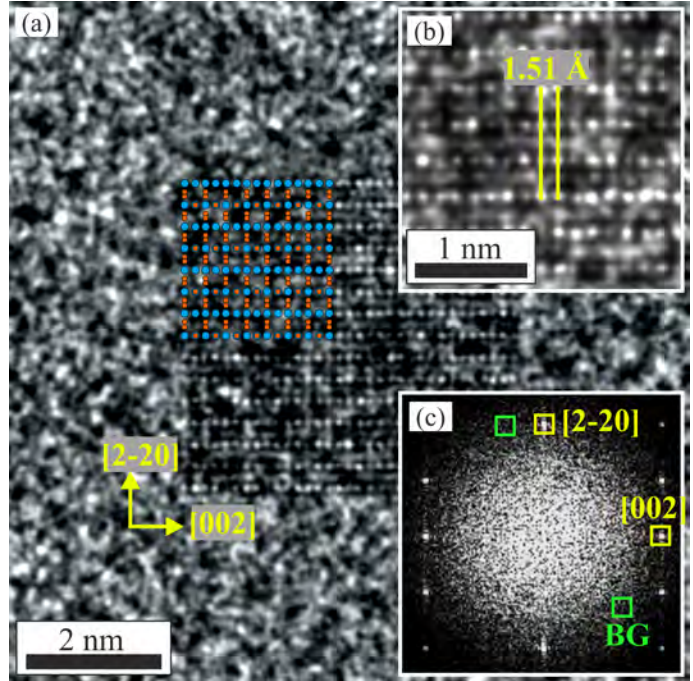
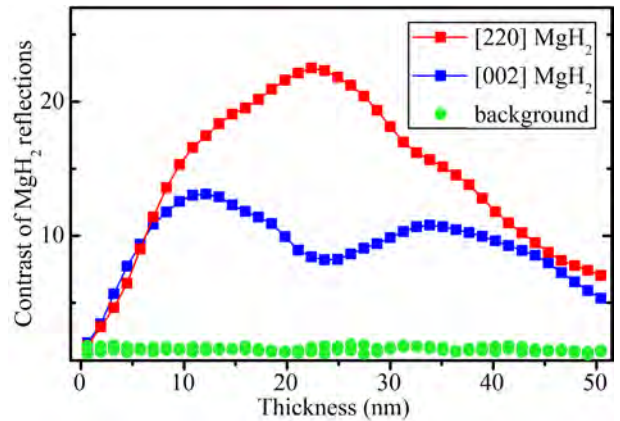


Figure 4.11 Contrast for MgH_2 inside the nanoreactor at optimum defocus as function of the thickness. Starting at a thickness of 5 nm, i.e. a contrast of 10, the Mg atom columns can be clearly resolved in the HRTEM image.



The contrast of the MgH_2 crystal at optimum defocus, which is determined from a contrast map (not shown), is plotted as function of the thickness in Figure 4.11. Also for the lighter MgH_2 , the contrast is high enough to resolve the crystal structure over a wide range of thicknesses. As in the case of Mg, weak Bragg reflections of the MgH_2 can be measured for thicknesses down to 2 nm, but the Mg atom columns become visible unambiguously only at thicknesses of 5 nm and higher in the real space images. The contrast of the [2-20] reflection is higher than that of the [002] contrast because of the larger scattering angle at [002]. Nonetheless, the (002) lattice planes of MgH_2 with a spacing of 1.51 Å are still clearly visible as can be seen in the magnification shown in the inset in Figure 4.10(b).

The influence of further parameters such as the gas pressure on the contrast can also be

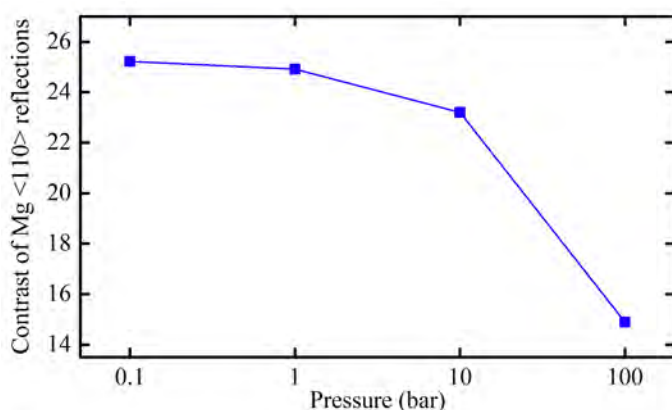


Figure 4.12 Simulated contrast for a 17 nm thick Mg crystal at optimum defocus as function of the hydrogen gas pressure.

studied using this multislice approach. In Figure 4.12 the simulated contrast of a 17 nm thick Mg crystal at optimum defocus is plotted as function of the hydrogen pressure. Only for unrealistically high pressures of 100 bar, a substantial contrast reduction is expected to occur. In consequence, the contrast is mainly limited by the SiN windows and not by the enclosed gas for pressures around 1 bar, as they are relevant for in-situ ETEM investigations. Therefore, the best way to improve the achievable contrast of the nanoreactor is using thinner windows that are still mechanically stable enough to withstand the gas pressure against vacuum. The thinnest of all thinkable substrates, graphene, can withstand a pressure of 10 kbar, which was experimentally shown by Algara-Siller et al. [2015]. Graphene would therefore be the ultimate window material, with which contrasts and resolution comparable to conventional HRTEM should be achievable.

4.6.3. Conclusions of the Multislice Simulations

The results of HRTEM multislice simulations of a $\text{Mg}(\text{H}_2)$ crystal placed inside a windowed environmental cell, such as the nanoreactor described by Yokosawa et al. [2012], which allows for in-situ HRTEM studies in hydrogen at ambient pressure, are presented. Both, the achievable resolution and contrast are sufficient to measure Bragg reflections of both the Mg and MgH_2 phase with a thickness as low as 2 nm. Thicker layers of at least 5 nm are necessary to unambiguously resolve the specimen and to localize individual atom columns of Mg. It is also shown that higher hydrogen pressures of up to 10 bar would have only a minor negative effect on the contrast. It is rather the thickness of the SiN windows that mainly limits the performance of the setup. Based on these findings, the expected spatial resolution and signal-to-noise-ratio of the nanoreactor prove valuable for the investigation of nanostructured hydrides. However, one has to keep in mind, that actual research focuses on MgH_2 nanoparticles with sizes that approach 1 nm. This reduction in size is needed for a substantial and required modification of the thermodynamic properties [Wagemans et al.,

2005]. Such small structures cannot be resolved inside the nanoreactor. The situation is expected to become increasingly difficult, if few nanometer sized Mg(H₂) crystals are embedded in a carbon scaffold [Jia et al., 2013], sandwiched between heavy Pd and TiH₂ thin films [Mooij et al., 2011], or covered by a thin oxide surface layer. This highlights the need to further improve the capabilities of such in-situ TEM technique in order to meet the challenges in the characterization of state-of-the-art and future nanostructured materials.

5. Nanoconfinement of LiBH_4 in Aerogel-Like Carbon

In this chapter, the results of the nanoconfinement of LiBH_4 in a nanoporous carbon are presented. First, in Section 5.1, the properties of selected nanoporous carbon materials, which are relevant for nanoconfinement, and their synthesis routes are described briefly and compared to the porous carbon synthesis via salt templating, which has been used for the present work. Following this, the results of the DSC analysis of the melt infiltration and the XRD analysis of the nanoconfined LiBH_4 are discussed in Sections 5.2 and 5.3. The hydrogen sorption properties studied by thermogravimetry and mass spectrometry are covered in Section 5.4. Section 5.5 deals with the investigation of the local nanostructure of the nanoconfined LiBH_4 by means of STEM-EELS. In-situ heating is utilized to examine the behavior of the reaction products at high temperatures. Finally, the results of the MAS NMR analysis, which are discussed in Section 5.6, shed light on the question of the relatively poor reversibility achieved for the nanoconfined LiBH_4 . Most of this chapter has already been published in [Surrey et al., 2016a].

5.1. Nanoporous Carbon Scaffolds

The highly ordered nanoporous carbon (NPC) with a narrow pore size distribution centred around 4 nm used by Liu et al. [2011] shows a total pore volume of $0.53 \text{ cm}^3/\text{g}$. CMK3 is another carbon scaffold, which is widely used for the nanoconfinement of hydrides and provides a relatively large total pore volume of $1.1 - 1.25 \text{ cm}^3/\text{g}$ with an average pore size of 4 nm [Cahen et al., 2009]. However, for the synthesis, the hard silica template SBA-15 is used, which itself requires a complicated multi-step preparation. After the template is filled with carbon it needs to be etched by hydrofluoric acid and is then lost. With zeolite templating a carbon scaffold with a high microporous volume of $2.0 \text{ cm}^3/\text{g}$ and an average pore size of 1.4 nm has been prepared, for which the highest loading of nanoconfined LiBH_4 of 40 – 50 wt.% has been reported by Shao et al. [2015]. However, for this scaffold also the template has to be synthesized first and then removed by hydrofluoric and hydrochloric

acids, which is a major issue making such a preparation barely scalable.

In comparison, the nanoporous carbon used in the present work has a cumulative pore volume of $0.85 \text{ cm}^3/\text{g}$ for pores up to 4 nm and increases further, if also larger pores are taken into account (cf. Figure 5.1(b)). The total pore volume of the aerogel-like carbon scaffold used for the nanoconfinement of LiBH_4 is $3.27 \text{ cm}^3/\text{g}$. The material is prepared by the salt templating technique, which is a facile and sustainable synthesis route for the production of meso- and microporous materials with high pore volumes. The details of this technique have been explained by Fechner et al. [2013] and only a brief description will be given here: An ionic liquid as carbon precursor is mixed with a salt as the porogen, which has a low melting point of $200 - 300 \text{ }^\circ\text{C}$. This mixture is heated to $1000 \text{ }^\circ\text{C}$ in nitrogen for carbonization, followed by the removal of the porogen salt with water, from which the salt can potentially be recovered afterwards. The process is illustrated in Figure 5.1(a). Heteroatom-containing carbon scaffolds can be achieved by the choice of the used ionic liquid. Accordingly, nitrogen or boron doped carbons have been synthesized. The pore sizes are governed by the used salt, e.g. sodium, potassium or lithium chloride in an eutectic mixture with zinc chloride.

In the present work the nitrogen doped aerogel-like carbon synthesized in a NaCl-ZnCl_2 salt melt from the ionic liquid 1-Butyl-3-methyl-pyridinium dicyanamide (Bmp-dca), labelled as BMP_dca_NaZn_145, is used for the nanoconfinement of LiBH_4 . The material has been provided by Dr. Nina Fechner from the Max-Planck Institute for Colloids and Interfaces in Golm. The porosity evaluation of the aerogel-like carbon has also been conducted by this collaborator. The structural nitrogen content is 4.2 wt.% and the amount of residual sodium and zinc salt is less than 1 wt.% after washing with water. Nitrogen sorption analysis reveals an apparent surface area of $1866 \text{ m}^2/\text{g}$ calculated by applying the Brunauer-Emmett-Teller (BET) model. The pore size distribution displayed in Figure 5.1(b) is calculated from nitrogen sorption data using the nonlocal density functional theory (NLDFT) equilibrium model method. Besides the mesoporosity the aerogel-like carbon exhibits a high fraction of micropores with pore sizes smaller than 2 nm. In Figure 5.1(b) the cumulative pore volume V and the corresponding loadings L with LiBH_4 according to the equation

$$L = \left(1 + \frac{1}{\rho_{\text{LiBH}_4} V}\right)^{-1}, \quad (5.1)$$

where $\rho_{\text{LiBH}_4} = 0.666 \text{ g/cm}^3$ is the density of LiBH_4 under ambient conditions, are plotted as function of the pore size.

Compared to the synthesis routes of the other porous carbons described above, salt templating has the advantage of being scalable and sustainable, requiring only inexpensive

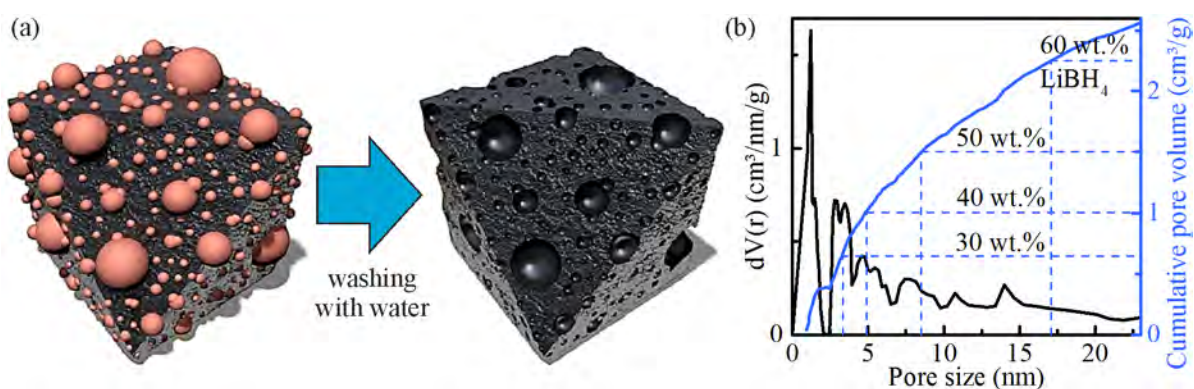


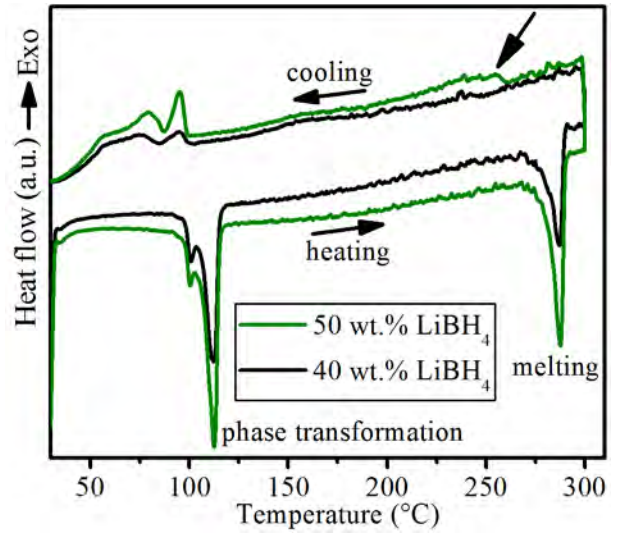
Figure 5.1.(a) Illustration of the aerogel-like carbon scaffold (drawn in black) prepared by salt templating (figure adapted from [Yang et al., 2015]) The porogen salts (drawn in orange) can be removed by simple washing with water. (b) Pore size distribution (left scale in black) and cumulative pore volume (right scale in blue) of the aerogel-like carbon scaffold. The theoretical loadings of 30, 40, 50, and 60 wt.% of LiBH₄ are indicated by the blue dashed lines for the respective pore volumes according to Equation 5.1.

salts, water, and a carbon precursor, which can be also derived from biomass instead of the relative expensive ionic liquids as shown by Yang et al. [2015].

5.2. DSC Analysis of Melt Infiltration

Prior to the melt infiltration of the aerogel-like carbon with LiBH₄ it is mandatory to carefully dry the material at 600 °C for 2 h under an hydrogen atmosphere to remove adsorbed water, which can easily amount to 10 wt.% of the carbon material. During the drying process it was observed that a whitish condensate formed at the cold end of the glass tube which is assumed to be residual salt evaporating from the porous carbon. After a repeated drying, the condensation was largely reduced and there was hardly any condensate visible any more. The physical mixtures (ca. 20 – 50 mg) are prepared by mixing 40 and 50 wt.% of LiBH₄ with the dried carbon in a mortar. These samples are referred to as PM40 and PM50, respectively. The DSC curve of the melt infiltration of sample PM40 is shown in Figure 5.2. Upon heating, there are two endothermic peaks at 112 °C and 287 °C. They correspond to the phase change from the orthorhombic to the hexagonal phase and the melting of LiBH₄, respectively. The temperature is kept constant at 300 °C for 30 min to allow the molten LiBH₄ to enter the pores. After the melt infiltration upon cooling, no exothermic peak is observed that would be attributed to the recrystallization of hexagonal LiBH₄, which indicates that the hydride remains amorphous upon cooling. Below 100 °C, there is a broad exothermic double peak, which corresponds to the crystallization into the orthorhombic phase. However, the LiBH₄ is amorphous due

Figure 5.2 DSC curves obtained during the melt infiltration of the physically mixed samples with 40 and 50 wt.% of LiBH_4 labeled as MI40 and MI50, respectively.



to the nanoconfinement, and hence the thermodynamics of this phase transformation have changed. This explains the different shape of the double peak upon cooling compared to the double peak of the transformation of the bulk LiBH_4 upon heating. The integrated areas of both double peaks are comparable. The DSC curve of the melt infiltration of the PM50 sample shows a small bulge at 255 °C upon cooling (indicated by the arrow in Figure 5.2) which points to a partial recrystallization. Furthermore the double peak below 100 °C upon cooling is sharper than the one of the PM40 sample. This means that for 50 wt.% of LiBH_4 , not all of the hydride is amorphous. The samples after melt infiltration are labeled MI40 and MI50, respectively.

5.3. XRD Analysis

XRD measurements support the findings of the DSC analysis given in the previous section. For the MI40 sample, no peaks pointing to any crystallinity can be observed in Figure 5.3. This means that the hydride has no long range order and is either nanocrystalline or amorphous. The MI50 sample, however, reveals some weak diffraction peaks which correspond to LiBH_4 in the orthorhombic phase. Hence, a small fraction of the hydride is crystalline.

BET measurements of the carbon scaffold point to a total pore volume of 3.27 ml/g, which would theoretically allow for a LiBH_4 loading of 68 wt. %. It has been reported that LiBH_4 is still crystalline, when confined in a carbon aerogel with a pore size of 9 nm, whereas it is amorphous in highly ordered NPC with a pore size of 4 nm [Liu et al., 2011]. Integrating the pore volume of the here used carbon scaffold up to the pore size of 9 nm, yields a total pore volume of 1.55 cm^3/g , which corresponds to a LiBH_4 loading of 50 wt.% (see Figure 5.1). A LiBH_4 loading of 40 wt.% requires a pore volume of 1 cm^3/g , which is

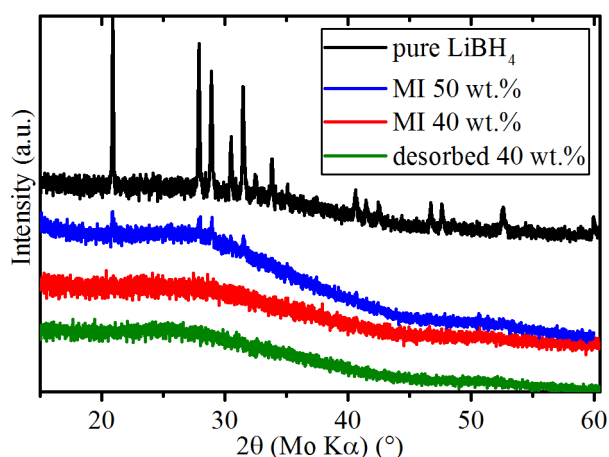


Figure 5.3 XRD measurement of pure LiBH_4 , melt infiltrated LiBH_4 with 40 and 50 wt.% LiBH_4 and the desorbed sample.

available by filling only the pores up to 5 nm in size. Apparently, the MI40 sample shows no crystallinity, because the molten hydride tends to occupy the smaller pores first, while pores larger than 5 nm remain empty. This is due to the fact, that the capillary pressure is inversely proportional to the pore size, as can be seen from Equation 2.12. The MI50 sample, on the other hand, clearly reveals some crystallinity, because in this case, LiBH_4 is present in larger pores up to 9 nm as well. The maximum loading for noncrystalline LiBH_4 that can be reached with this carbon scaffold is between 40 and 50 wt.%. This consistent picture demonstrates that the entire available pore volume can be accessed by the molten hydride without any pore blocking. For the MI50 sample, the presence of residual LiBH_4 which is not confined in the pores cannot be ruled out completely. It is, however, very unlikely, since the total available pore volume is more than twice the volume needed for 50 wt.% of LiBH_4 , i.e. 1.5 ml/g. Furthermore, residual LiBH_4 outside the carbon scaffold could not be observed in (S)TEM investigations of the MI50 sample.

5.4. Thermogravimetry and Mass Spectrometry Analysis

5.4.1. Hydrogen Desorption Properties of Nanoconfined LiBH_4

In the thermal desorption spectra shown in Figure 5.4(a), the mass change of the melt infiltrated LiBH_4 (MI40) is compared with that of physically mixed (PM40) and pure LiBH_4 by thermogravimetry. The mass ratios are obtained by dividing the measured total sample mass by the mass of LiBH_4 thereby neglecting the mass of the carbon scaffold. The calculated mass changes dm/dt are determined from the time derivative of this mass ratio and are scaled to the same level for a better comparison. Already the PM40 shows

a reduced decomposition temperature with an onset at $240\text{ }^\circ\text{C}$ and a main mass loss at $310\text{ }^\circ\text{C}$, which lies $90\text{ }^\circ\text{C}$ below the decomposition temperature of pure LiBH_4 . At this temperature, pure LiBH_4 shows only a very small mass loss due to a minor decomposition upon melting. The shoulder of the mass change peak at the melting temperature of $280\text{ }^\circ\text{C}$ implies that there are two overlapping reaction steps.

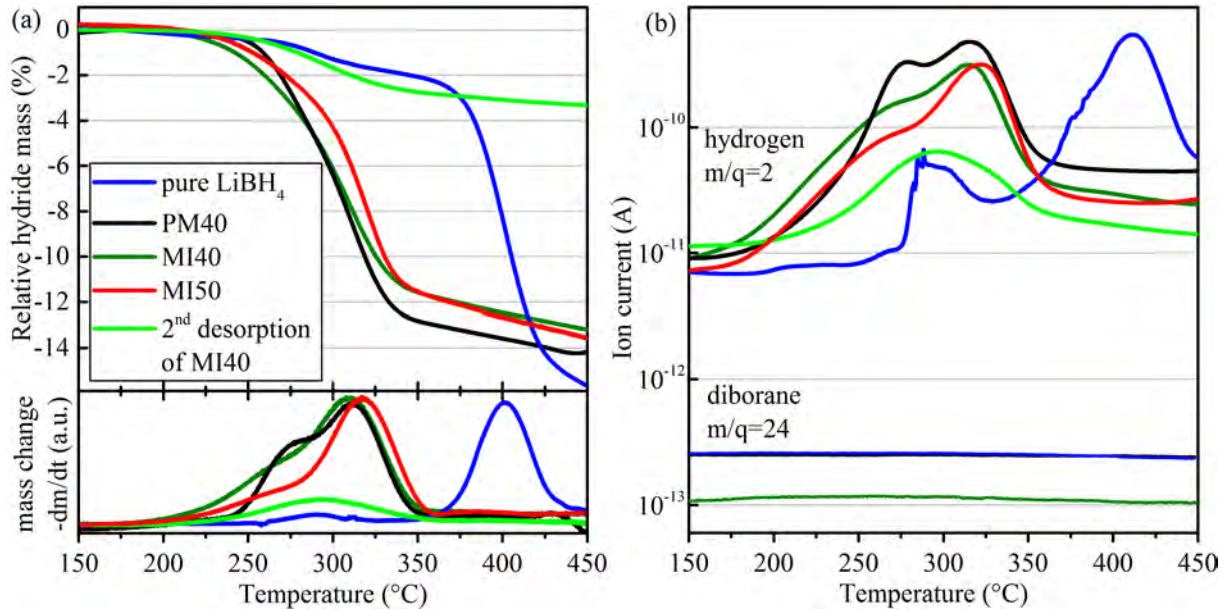


Figure 5.4. (a) Thermogravimetry of pure LiBH_4 , the physically mixed sample with 40 wt.% LiBH_4 (PM40), the melt infiltrated sample with 40 and 50 wt.% LiBH_4 (MI40 and MI50), and the desorbed MI40 sample after rehydrogenation at 100 bar hydrogen and $300\text{ }^\circ\text{C}$ for 3 h (MI40 2nd des.). (b) Simultaneous mass spectrometry of hydrogen ($m/q = 2$) and diborane ($m/q = 24$). Experiments are performed during heating the materials from room temperature to $550\text{ }^\circ\text{C}$ with $1\text{ K}/\text{min}$ under an argon flow at a pressure of 1 bar.

For the MI40, the onset temperature is further reduced to roughly $200\text{ }^\circ\text{C}$ and the main mass loss occurs at $310\text{ }^\circ\text{C}$, which is identical to the PM40. This means that above the melting point, the LiBH_4 in the PM40 also infiltrates the nanopores and is then identical to the MI40. The observed mass change of the PM40 at temperatures well below the melting point of LiBH_4 implies that there is a strong catalytic effect of the carbon as it apparently destabilizes the LiBH_4 just due to the pure Li contact. At this low temperature, it can be ruled out that LiBH_4 has melted and entered the pores of the carbon scaffold. This observation is indicative for two desorption mechanisms: (i) the catalytically promoted decomposition of solid LiBH_4 , which is enhanced for the MI40 sample through nanoconfinement and amorphization and (ii) the catalytically promoted decomposition of molten LiBH_4 within the carbon pores. It cannot be excluded, that the catalytic effect may also be due to the residual salts, NaCl or ZnCl , in the carbon scaffold, however there are no reports in

the literature that these salts could act as a catalyst for the dehydrogenation of LiBH_4 . The even lower onset temperature for the decomposition of the MI40 reveals a further destabilization of the LiBH_4 due to amorphization and a stronger interaction with the carbon inside the pores. For the MI50, the main mass loss is shifted to a slightly higher temperature of 317 °C compared to the MI40. In this sample also larger pores up to 9 nm are filled with LiBH_4 (cf. discussion in Section 5.3). This confirms that the decomposition temperature decreases with decreasing pore size as shown by Liu et al. [2011] and Gross et al. [2008]. A higher filling of the aerogel-like carbon with LiBH_4 would result in a further increase of the decomposition temperature. The onset temperature of MI50 is as low as the one of MI40, because it is due to the destabilization of the LiBH_4 confined within the smallest pores of the aerogel-like carbon.

The results of the mass spectroscopy displayed in Figure 5.4(b) are in excellent agreement with those of the thermogravimetric measurements and show clearly that the measured mass changes are due to the desorption of hydrogen. A release of diborane could not be measured in any sample under the experimental conditions used.

The observed hydrogen desorption temperature is ca. 30 °C lower than the one reported by Liu et al. [2011] for 33 wt.% LiBH_4 nanoconfined in highly ordered NPC, but still higher than the decomposition temperature of only 100 °C measured for LiBH_4 in carbon nanotubes or hollow and nanoporous CuS nanospheres by Lai et al. [2014]. However, the loadings of the aerogel-like carbon with 40 and 50 wt.% are as high as those recently published for LiBH_4 nanoconfined in zeolite-templated carbon [Shao et al., 2015], which represent the highest LiBH_4 loadings reported so far. The decomposition temperatures of 310 °C and 317 °C achieved in the present work are even slightly lower than those for LiBH_4 in zeolite-templated carbon with 332 °C and 336 °C for loadings of 40 and 50 wt.%, respectively. Furthermore, due to the large pore volume of the aerogel-like carbon scaffold, an even higher loading with LiBH_4 is possible. As mentioned above this would be at the cost of a further increase in the decomposition temperature, which however might still be lower or comparable to that for LiBH_4 in zeolite-templated carbon, where higher loadings result in the deterioration of the dehydrogenation properties due to the limited pore volume [Shao et al., 2014]. The increase in the LiBH_4 loading above 50 wt.% is outside the scope of the present work, but this discussion shows the great potential of these carbon scaffolds prepared by salt templating for the nanoconfinement of complex hydrides.

5.4.2. Rehydrogenation of Nanoconfined LiBH_4

Besides the decomposition temperature, the reversibility of the hydrogen desorption is studied. For this, the dehydrogenated sample MI40 was exposed to 100 bar hydrogen at 300 °C for 3 h in a Netzsch 204 HP DSC. During the second desorption cycle, the in this way rehydrogenated sample experiences only a comparably small mass loss at that temperature, where the desorption occurred during the first cycle (c.f. Figure 5.4). However, since for bulk LiBH_4 the rehydrogenation does not take place under the relatively mild experimental conditions used here, this partial rehydrogenation is already a significant improvement, although only 3 wt.% of hydrogen is released during this second dehydrogenation. At such mild conditions, higher rehydrogenation rates of roughly 70 – 50 % of the initial hydrogen capacity have been published for the second and up to the fifth cycle, respectively, for comparable nanoconfined LiBH_4 (see Section 2.5.2 for more details). So far, full reversibility of LiBH_4 at mild conditions has been achieved only for the nanoconfinement in CuS nanospheres [Lai et al., 2014].

The capacity losses are generally attributed either to a phase separation of the reaction products or the formation of the very stable closoborane salts, which represent thermodynamic sinks [Liu et al., 2011]. The former can be identified using TEM, while the latter can be detected by solid state ^{11}B NMR. In the following two sections the investigation of the nanoconfined LiBH_4 in aerogel-like carbon using these techniques are presented in order to answer the question of the small degree of rehydrogenation achieved.

5.5. In-situ STEM Analysis

Due to the lack of crystallinity, neither XRD (c.f. Figure 5.3) nor electron diffraction (not shown) reveal any information about the LiBH_4 in MI40 and in the desorbed sample. Therefore, the samples are further investigated by using STEM and EELS in order to study the local boron distribution in the carbon scaffold. Figure 5.5(a) shows an annular dark field (ADF) STEM image of the MI40. The atomic areal densities of boron and carbon are measured for the region marked with a black square in Figure 5.5(a) by acquiring EEL spectra at the boron and carbon K absorption edges at electron energy losses of 188 eV and 284 eV, respectively. The resulting elemental maps are displayed in Figure 5.5(b) and (c), respectively.

Most importantly, boron is detected in the entire carbon scaffold, which proves the successful melt infiltration of LiBH_4 . It can be seen from Figure 5.5(b) and (c) that regions with a high areal density of boron show a comparably small carbon content and

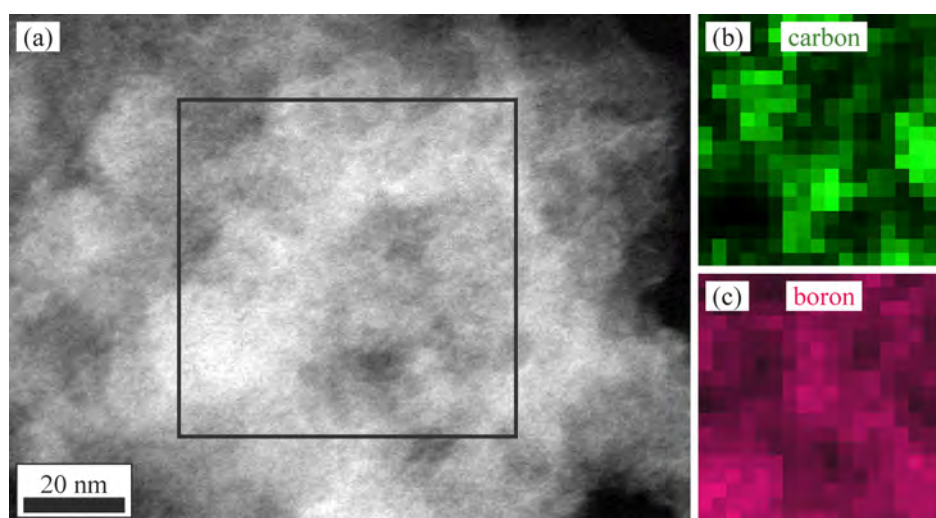


Figure 5.5. (a) ADF STEM image of the MI40. (b) Elemental map for boron of the region marked by the black square in (a) based on the EELS signal at the boron K absorption edge. (c) Elemental map of carbon from the same region based on the EELS signal at the carbon K absorption edge. The pixel size in (b) and (c) is $3.7\text{ nm}\times 3.7\text{ nm}$.

vice versa. This is indicative of a certain inhomogeneity of the carbon matrix at the nanoscale. Apparently, there are regions with higher pore densities and in turn lower carbon densities. In these areas, the finding of enhanced boron concentrations points to a successful filling of these pores with LiBH_4 . Due to the thickness of the carbon scaffold of $50 - 100\text{ nm}$ and the limited mapping resolution of $3.7\text{ nm}\times 3.7\text{ nm}$, individual pores cannot be resolved in these elemental maps. Since the lithium K edge at 55 eV overlaps with a broad plasmon resonance of carbon at 25 eV , a comparable Li mapping cannot be measured [Blanchard et al., 2009; Deprez et al., 2010].

In order to better understand the poor rehydrogenation of the MI40 sample, it is heated in-situ in the electron microscope and the boron distribution in the carbon scaffold is measured at $40\text{ }^\circ\text{C}$ and $400\text{ }^\circ\text{C}$. As an example, Figures 5.6(a) and (c) show the ADF-STEM images of the MI40 at $40\text{ }^\circ\text{C}$ and $400\text{ }^\circ\text{C}$ together with the elemental boron mappings in Figures 5.6(b) and (d) obtained with EELS from the rectangular areas marked in Figure 5.6(a) and (c), respectively. In both cases boron is present within the scaffold with a similar concentration, and, except for a small drift and rotation, the morphology of the carbon scaffold does not change upon heating. The difference in the overall amount of boron atoms in the investigated area lies well within the accuracy of the measurement. This indicates that also at $400\text{ }^\circ\text{C}$ the reaction product boron stays inside the pores of the carbon scaffold.

The ADF-STEM image in Figure 5.6(c) also reveals the presence of small spherical nanoparticles with a size of $1 - 4\text{ nm}$ at the carbon scaffold and on the substrate. The size

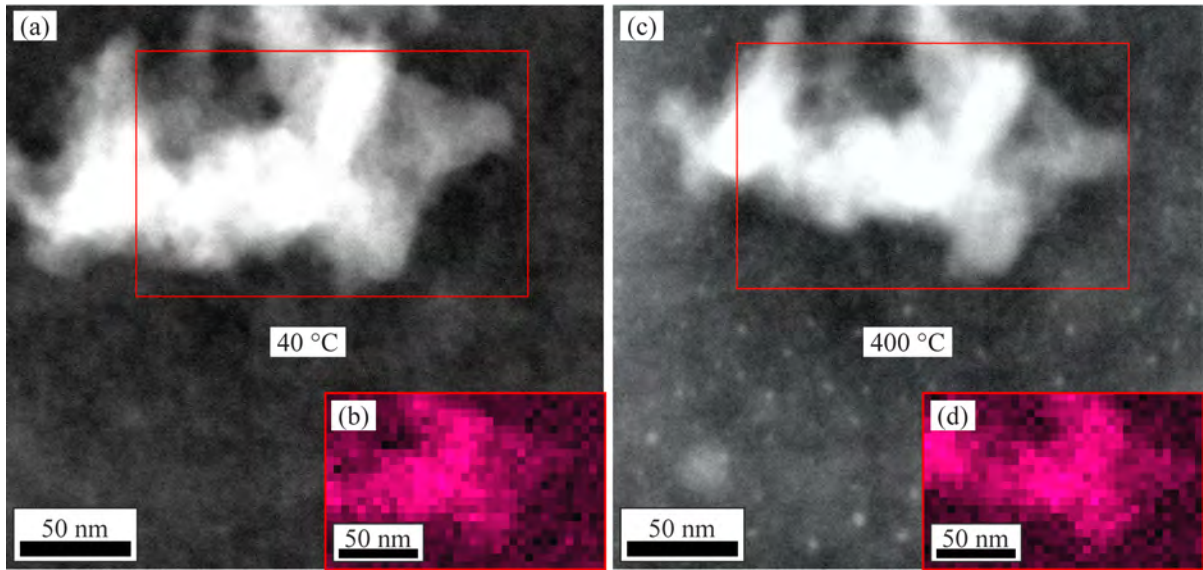


Figure 5.6. (a) ADF-STEM image of the MI40 at 40 °C on a SiN substrate covered with 5 nm amorphous carbon. (b) Elemental map for boron of the region marked by the red rectangle in (a) based on the EELS signal at the boron K absorption edge. (c) ADF-STEM image of the same specimen as in (a) at 400 °C. (d) Elemental map for boron of the same region at 400 °C.

distribution of these nanoparticles is shown in Figure 5.7(b). For this, 400 nanoparticles that are present on the substrate next to the carbon scaffold as shown in the ADF-STEM image in Figure 5.7(a) are analysed. Recently, House et al. [2014] have also reported the observation of nanoparticles which appear upon heating of LiBH_4 nanoconfined in highly ordered NPC. Here, the cubic nanocrystals with a size of 8 – 15 nm were identified by electron diffraction as LiH nanocrystals. The authors have explained the poor reversibility of the nanoconfined LiBH_4 with the ejection of the LiH from the pores of the scaffold. This finding was also supported by a first-principles study using density functional theory [Mason and Majzoub, 2014]. However, House et al. [2014] have also observed smaller spherical nanoparticles with a size of 2 – 5 nm which were due to precipitations from the carbon substrate at high temperatures. The nanoparticles observed in the present work match the size distribution of the latter carbon precipitates. Furthermore, neither electron diffraction of in-situ and ex-situ heated samples (not shown) nor XRD measurements reveal any crystallinity. In principle, this could be due to the nanoscopic size of the particles and would not necessarily allow to exclude LiH nanoparticles. However, the particles are also present at a large distance (some μm) from the carbon scaffold and show no concentration gradient towards the scaffold (cf. Figure 5.7(a)). Therefore, it can be concluded that the nanoparticles in the ADF-STEM images in Figures 5.6(c) and 5.7(a) are amorphous carbon precipitates and that no ejection of LiH nanocrystals from the carbon pores occurs. This is an important finding, since the presence of the desorption products inside the pores is a

precondition for a good reversibility.

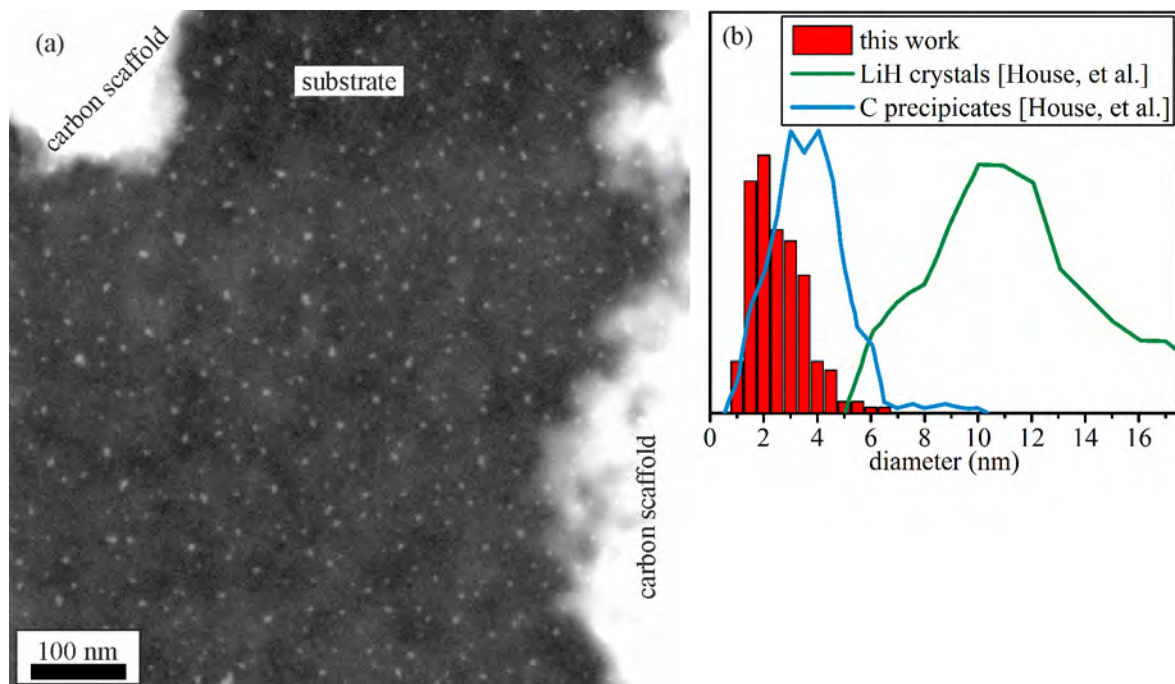


Figure 5.7. (a) Annular darkfield STEM image at 400 °C. (b) particle size distribution of the nanoparticles compared to those of LiH nanocrystals and carbon precipitates as observed by House et al. [2014].

The experimental findings, however, do not shed any light on the small amount of hydrogen reversibly stored. Despite the high chemical inertness of the carbon scaffold, reactions with the LiBH_4 cannot be ruled out completely. For example, the formation of Li_2C_2 is known to start at around 400 °C [Adelhelm and de Jongh, 2011]. However, a melt infiltrated sample with 40 wt.% LiBH_4 heated to 350 °C instead of 550 °C also shows just a small hydrogen desorption of 4.5 wt.% during the second dehydrogenation. Therefore, in Section 5.6, a ^{11}B MAS NMR study is presented that allows to shed some light on the question of the poor reversibility.

Electron Beam Damage

In Chapter 4 the electron beam induced dehydrogenation of MgH_2 due to radiolysis is studied in detail. This effect occurs also for LiBH_4 [Deprez et al., 2010]. Therefore, it can safely be assumed that also the LiBH_4 studied here by STEM is suffering from this beam damage and it is not in the LiBH_4 phase anymore, because the STEM images at high magnification and moreover the acquisition of EEL spectra at every pixel of the images require much larger electron doses than those used for MgH_2 in Chapter 4. However, this degradation is not directly observable, since the hydride is amorphous, in which case the

phase cannot be investigated. STEM EELS is rather carried out to study the distribution of boron in the carbon scaffold, which can be expected not to change significantly when LiBH_4 is decomposing upon irradiation by the electron beam. The encapsulation of the hydride in the aerogel-like carbon further reduces other forms of beam damage such as atomic displacement, knock-on damage, or sputtering of the hydride material. The carbon scaffold itself does not suffer from beam damage, because an incident electron energy of 80 keV is used, which is below the threshold of knock-on damage for carbon.

Also a decomposition of LiH in the TEM has been reported by Deprez et al. [2010]. This sheds some doubts on the detection of crystalline LiH by House et al. [2014] using electron diffraction. The authors have not even mentioned any observation of beam damage in their TEM study for LiH. However, it is possible that the applied electron dose has been small enough to avoid the decomposition of LiH, because the electron dose needed for electron diffraction is generally smaller than for high resolution studies like those presented in Section 5.5. Even if LiH was ejected from the aerogel-like carbon, it can be expected that it would decompose to Li or more like form Li_2O . These decomposition products should also be observable by STEM or electron diffraction. However, no evidence for their presence outside the aerogel-like carbon can be found in the in-situ STEM investigation.

5.6. Solid state ^{11}B NMR

Figure 5.8 shows the ^{11}B MAS NMR spectra for pure LiBH_4 as a reference, the MI40, and the dehydrogenated sample, which was heated to 350 °C. Both the pure LiBH_4 and the MI40 sample present sharp peaks belonging to the boron atoms of the $(\text{BH}_4)^-$ anion which is known to occur at -41 ppm [Hwang et al., 2008]. Due to the small amount of material (20 mg) and the broad resonance peak the dehydrogenated sample has a relatively low signal-to-noise ratio. The measurement required 15 times more scans compared to the pure LiBH_4 or the MI40 sample and the spectrum is multiplied by a factor of 3 in Figure 5.8.

The broad peak that is centered around 15 ppm overlaps with a small peak at -41 ppm, which represents a small amount of unreacted LiBH_4 . The broadening of the signal is typical for disordered materials that isotropically distribute their chemical shifts [Hwang et al., 2008]. The spectrum matches that of amorphous boron, which presents a chemical shift around 0 ppm [Hwang et al., 2008; Bonatto Minella et al., 2011]. The shift towards positive values indicates the presence of minor oxide contaminations known to fall at roughly 14 and 9 ppm as well as boron hydroxide at 1 ppm [Au et al., 2008]. Formation of oxides can take place considering the high reactivity of tetrahydroborates towards moisture, which could not be entirely avoided [Choi et al., 2011]. The formation of $\text{Li}_2\text{B}_{12}\text{H}_{12}$, which

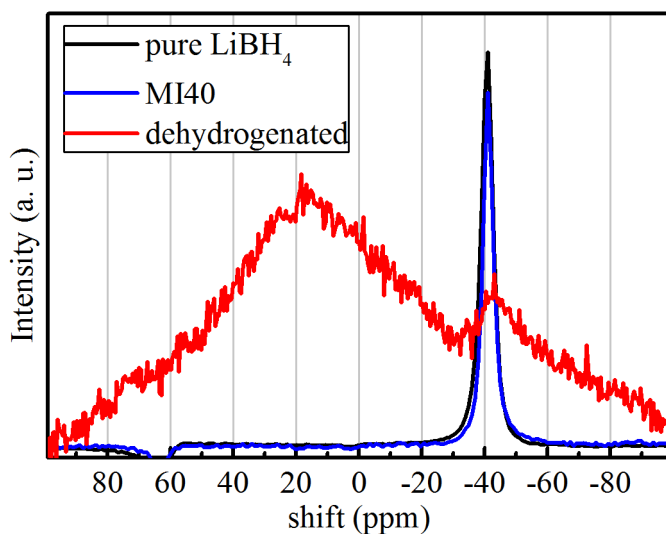


Figure 5.8 ^{11}B MAS NMR spectra of pure LiBH_4 (black line) and the MI40 sample (blue line) with peaks at -41 ppm. The dehydrogenated sample (red line) shows a broad peak centered at 15 ppm indicating amorphous partially oxidized boron. An additional peak at -41 ppm arises from residual unreacted LiBH_4 .

would show a peak at -16 ppm [Au et al., 2008; Choi et al., 2011], cannot be excluded completely, because the signal could be superimposed by the broad boron peak. However, the quantity of $\text{Li}_2\text{B}_{12}\text{H}_{12}$ is negligible.

The oxide formation can explain the low reversibility achieved. It may be caused by impurities in the argon, the as-purchased materials or the carbon scaffold. Covering the nanoconfined LiBH_4 with the polymer PMMA could reduce the oxidation due to the selective gas permeability of the polymer [Jeon et al., 2011]. The reversibility at mild conditions could further be improved by the addition of Ni nanoparticles as catalysts embedded in the carbon scaffold [Ngene et al., 2010].

6. Conclusions

In the first part of the present work, a detailed and quantitative analysis of the electron beam induced dehydrogenation of nanocrystalline MgH_2 is presented. VEELS is used to investigate this phenomenon in-situ in a monochromated TEM under low dose conditions. MgH_2 is metastable in high vacuum and only kinetically stabilized, because the nucleation of Mg is difficult, especially at room temperature. The electron beam, however, generates nucleation sites for the Mg phase throughout the particle, but the metal phase does not grow by itself at the accessible time scale of minutes due to slow reaction kinetics. Hence, the observed dehydrogenation is solely induced by the electron illumination. Based on the derived characteristic electron doses for acceleration voltages of 80 kV and 300 kV it is shown that the radiolytic decomposition is caused by the inelastic scattering of the incident electrons by the MgH_2 plasmon. The rate of the dehydrogenation increases with increasing electron current density and decreasing specimen thickness. A discrepancy between the experimental doses and from the inelastic scattering cross section calculated doses by a factor of roughly 4 points to a kinetic barrier for the dehydrogenation due to the thin native surface oxide layer. The sensitivity of the MgH_2 to the electron beam is so high that a high resolution TEM study of unprotected nanostructured MgH_2 with large electron doses is not feasible. The obtained insight of this work is also applicable to other hydrides, which are relevant for solid state hydrogen storage. The results will help to perform and correctly interpret TEM investigations of such nanostructured hydrides in future.

Multislice HRTEM contrast simulations are conducted to theoretically study the feasibility of HRTEM investigation of light weight metals and metal hydrides at ambient hydrogen pressure rather than under vacuum. At these elevated pressures the hydride can be stabilized and the decomposition of the sample can be prevented. It is shown for Mg and MgH_2 as a model system that atomic resolution can be achieved for only few nanometer thin specimens placed inside a windowed environmental cell, which is expected to prove valuable for the research of nanostructured hydrides. However, the capabilities of this in-situ ETEM technique need to be further improved in order to meet the challenges in the characterization of state-of-the-art and future nanostructured materials. Thinner membrane windows such as graphene are necessary to investigate hydride nanoparticles

that approach 1 nm or nanoconfined hydrides at elevated hydrogen pressures.

In the second part of this thesis, the results of the nanoconfinement of LiBH_4 by melt infiltration in an aerogel-like nitrogen-doped carbon scaffold prepared by salt templating are presented. The benefits of this scaffold are a facile and sustainable synthesis, tunable micro- and mesoporosity, large pore volumes and high chemical stability. DSC, XRD and STEM EELS investigations show that, for a loading of 40 wt. %, the LiBH_4 is contained exclusively within the pores of the carbon scaffold smaller than 5 nm and it is amorphous. Combined TG and MS confirm that the hydrogen desorption temperature of 310 °C is reduced by 90 °C with respect to the bulk value and this reaction shows a low onset temperature of 200 °C. A partial rehydrogenation is achieved under moderate conditions of 60 bar hydrogen and 300 °C. ^{11}B MAS NMR analysis reveals the presence of amorphous partially oxidized boron in the dehydrogenated sample, which can explain the relatively small degree of rehydrogenation achieved. In-situ STEM EELS at temperatures of up to 400 °C proves the presence of boron inside the carbon scaffold also for the dehydrogenated state. In contrast to what was reported recently for nanoconfined LiBH_4 in highly ordered NPC, an ejection of LiH from the carbon pores is not observed neither for the in-situ nor for the DSC heated sample. This leads to the conclusion that both decomposition products, B and LiH, remain inside the pores of the carbon scaffold. Although the attained hydrogen storage properties need to be considerably improved in order to meet the targets of the stationary or on-board vehicular hydrogen storage, the significance of this work is that LiBH_4 is successfully confined in a new promising carbon scaffold. This class of nanoporous materials prepared by salt templating opens the possibility to reach these targets using nanoconfinement.

A. Appendix

A.1. Derivation of the Fourier-Log Deconvolution

Since the inelastic scattering of incident electrons in a specimen are “rare” and independent events, the electron intensity I_n , which is integrated over the full energy loss range, follows a Poisson distribution:

$$I_n = IP_n = \frac{I}{n!} \left(\frac{d}{\lambda}\right)^n \exp\left(-\frac{d}{\lambda}\right), \quad (\text{A.1})$$

where d is the thickness of the specimen, I is the incident electron current, P_n is the probability of n inelastic scattering events, and λ is the mean free path for inelastic scattering. For $n = 0$, no scattering takes place and all incident electrons would show a zero loss with the intensity $I_0 = I \exp(-d/\lambda)$. However, in reality the incident electron beam is not monochromatic, but has a certain energy distribution $R(E)$, whose integral is normalized to one. Therefore, the measurable energy spectrum of the zero-loss peak is given by:

$$Z(E) = I_0 R(E). \quad (\text{A.2})$$

For a single scattering event ($n = 1$), i.e. the single interaction of an incident electron with a plasmon, the energy distribution $S(E)$ (as given by Equation 3.7) has an integrated intensity I_1 :

$$\frac{I_0}{1!I_0} \int S(E)dE = I \frac{d}{\lambda} \exp(-d/\lambda) = I_0 \frac{d}{\lambda} = I_1. \quad (\text{A.3})$$

The measurable energy spectrum for this single scattering is:

$$M_1(E) = \frac{I_0}{1!I_0} R(E) \otimes S(E). \quad (\text{A.4})$$

If one incident electron excites two plasmons ($n = 2$), this double scattering $D(E)$ has an energy distribution of the form $S(E) \otimes S(E)$ with an integrated intensity I_2 according to

the Poisson law:

$$\int D(E)dE = \frac{I_0}{2!I_0^2} \int S(E) \otimes S(E)dE = \frac{I_0}{2!I_0^2} \int S(E)dE \int S(E)dE = \frac{I_0}{2!} \left(\frac{d}{\lambda} \right)^2 = I_2, \quad (\text{A.5})$$

and the measurable energy spectrum is

$$M_2(E) = \frac{I_0}{2!I_0^2} R(E) \otimes S(E) \otimes S(E). \quad (\text{A.6})$$

Accordingly the triple scattering energy spectrum is:

$$M_3(E) = \frac{I_0}{3!I_0^3} R(E) \otimes S(E) \otimes S(E) \otimes S(E). \quad (\text{A.7})$$

The final measured energy loss spectrum is

$$\begin{aligned} M(E) &= Z(E) + M_1(E) + M_2(E) + M_3(E) + \dots \quad (\text{A.8}) \\ &= Z(E) \otimes \left\{ \delta(E) + \frac{S(E)}{1!I_0} + \frac{S(E) \otimes S(E)}{2!I_0^2} + \frac{S(E) \otimes S(E) \otimes S(E)}{3!I_0^3} + \dots \right\}, \end{aligned}$$

where $\delta(E)$ is the Dirac delta function. Taking the Fourier transform of $M(E)$, the convolutions transform into multiplications in frequency space, ν :

$$m(\nu) = z(\nu) \left\{ 1 + \frac{s(\nu)}{1!I_0} + \frac{s(\nu)^2}{2!I_0^2} + \frac{s(\nu)^3}{3!I_0^3} + \dots \right\}, \quad (\text{A.9})$$

where the Fourier transforms of $Z(E)$ and $S(E)$ are $z(\nu)$ and $s(\nu)$, respectively. The term in curly brackets is exactly the Taylor series of the exponential function with the argument $s(\nu)/I_0$:

$$m(\nu) = z(\nu) \exp \frac{s(\nu)}{I_0}. \quad (\text{A.10})$$

Hence, one simply can take the logarithm of Equation A.10 and the inverse Fourier transform to extract the energy loss spectrum of the single scattering event without the contributions of the ZLP and plural scattering, hence the term Fourier-log deconvolution:

$$S(E) = FT^{-1} \left[I_0 \ln \frac{m(\nu)}{z(\nu)} \right]. \quad (\text{A.11})$$

In principle this would allow to recover the ideal single loss spectrum without suffering from the limited resolution of the spectrometer. In reality, however, this is not possible due to the presence of noise in experimental spectra $m(\nu)$. Especially noise at high frequencies will

be over-amplified by the division with the zero loss function $z(\nu)$, which goes to zero at high frequencies. $S(E)$ obtained from the inverse Fourier transform according to Equation A.11 is then submerged in high frequency noise. This can be avoided by the re-convolution of $S(E)$ with the zero-loss peak $R(E)$, i.e. multiplying $s(\nu)$ with $r(\nu)$ in Equation A.10 before taking the inverse Fourier transform in Equation A.11. This attenuates the high frequency values of $\ln(j/z)$, and takes into account the instrumentally broadening of the spectrum by the spectrometer. For the quantitative analysis of the Mg(H₂) VEEL spectra presented in Section 4.2, the Fourier-log deconvolution implemented in the software DigitalMicrograph is used. For this, the experimentally measured zero-loss peak without the specimen is chosen as the re-convolution function.

A.2. Derivation of Equation 4.2

In order to derive Equation 4.2, it is first shown that $\sum_{n=0}^{\infty} nP_n = d/\lambda$: I.e., it is to be shown that

$$\lambda/d \sum_{n=1}^{\infty} nP_n = 1.$$

With Equation A.1 this becomes

$$\begin{aligned} \lambda/d \sum_{n=1}^{\infty} nP_n &= \lambda/d \left\{ 0 \cdot P_0 + \sum_{n=1}^{\infty} n(1/n!)(d/\lambda)^n \exp(-d/\lambda) \right\} \\ &= \sum_{n=1}^{\infty} (1/(n-1)!)(d/\lambda)^{n-1} \exp(-d/\lambda), \end{aligned}$$

with $m = n - 1$ the summation can be written as

$$= \sum_{m=0}^{\infty} (1/m!)(d/\lambda)^m \exp(-d/\lambda) = \sum_{m=0}^{\infty} P_m = 1, \text{ q.e.d.},$$

because the Poisson distribution is normalized. Inserting this in Equation 4.1 yields

$$\frac{dN(t)}{dt} = -d/\lambda I$$

and using $I = jA$ and $1/\lambda = n_a\sigma$ Egerton [1989] this can be written as

$$\frac{dN(t)}{dt} = -dn_a\sigma jA.$$

The atom density for MgH_2 is given by $n_a = 3\rho N_A/M = 3N_{\text{MgH}_2}/V$ (cf. Equation 3.9), where N_{MgH_2} is the number of MgH_2 *molecules*. Since $N(t)$ describes the number of Mg–H bonds and since each MgH_2 *molecule* contains two bonds, it follows that $N_{\text{MgH}_2} = N(t)/2$. Accordingly, the atom density can be written as $n_a = 3/2N(t)/V$, which yields

$$\begin{aligned}\frac{dN(t)}{dt} &= -3/2dN(t)/V\sigma jA \\ &= -3/2N(t)\sigma j,\end{aligned}$$

because d and A cancel with V .

Bibliography

- Adelhelm, P. and de Jongh, P. E. The impact of carbon materials on the hydrogen storage properties of light metal hydrides. *J. Mater. Chem.*, 21:2417–2427, 2011.
- Aguey-Zinsou, K.-F. and Ares-Fernandez, J.-R. Hydrogen in magnesium: new perspectives toward functional stores. *Energy Environ. Sci.*, 3:526–543, 2010.
- Aguey-Zinsou, K.-F. and Ares-Fernández, J.-R. Synthesis of Colloidal Magnesium: A Near Room Temperature Store for Hydrogen. *Chem. Mater.*, 20(2):376–378, 2008.
- Algara-Siller, G.; Lehtinen, O.; Wang, F. C.; Nair, R. R.; Kaiser, U.; Wu, H. A.; Geim, A. K.; and Grigorieva, I. V. Square ice in graphene nanocapillaries. *Nature*, 519(7544): 443–445, 2015.
- Au, M.; Jurgensen, A.; Spencer, W.; Anton, D.; Pinkerton, F.; Hwang, S.-J.; Kim, C.; and Bowman Jr., R. Stability and Reversibility of Lithium Borohydrides Doped by Metal Halides and Hydrides. *J. Phys. Chem. C*, 112(47):18661–18671, 2008.
- Au, Y. S.; Obbink, M. K.; Srinivasan, S.; Magusin, P. C. M. M.; de Jong, K. P.; and de Jongh, P. E. The Size Dependence of Hydrogen Mobility and Sorption Kinetics for Carbon-Supported MgH_2 Particles. *Adv. Funct. Mater.*, 24(23):3604–3611, 2014.
- Baldi, A.; Pálsson, G. K.; Gonzalez-Silveira, M.; Schreuders, H.; Slaman, M.; Rector, J. H.; Krishnan, G.; Kooi, B. J.; Walker, G. S.; Fay, M. W.; Hjörvarsson, B.; Wijngaarden, R. J.; Dam, B.; and Griessen, R. Mg/Ti multilayers: Structural and hydrogen absorption properties. *Phys. Rev. B*, 81(22):224203, 2010.
- Baldi, A.; Narayan, T. C.; Koh, A. L.; and Dionne, J. A. In situ detection of hydrogen-induced phase transitions in individual palladium nanocrystals. *Nat. Mater.*, 13(12): 1143–1148, 2014.
- Bardají, E.; Zhao-Karger, Z.; Boucharat, N.; Nale, A.; van Setten, M.; Lohstroh, W.; Röhm, E.; Catti, M.; and Fichtner, M. $\text{LiBH}_4\text{-Mg}(\text{BH}_4)_2$: A Physical Mixture of Metal

- Borohydrides as Hydrogen Storage Material. *J. Phys. Chem. C*, 115(13):6095–6101, 2011.
- Blanchard, D.; Shi, Q.; Boothroyd, C. B.; and Vegge, T. Reversibility of Al/Ti Modified LiBH_4 . *J. Phys. Chem. C*, 113:14059–14066, 2009.
- Bogdanovic, B.; Brand, R. A.; Marjanovic, A.; Schwickardi, M.; and Tölle, J. Metal-doped sodium aluminium hydrides as potential new hydrogen storage materials. *J. Alloys Compd.*, 302(1-2):36–58, 2000.
- Bonatto Minella, C.; Garroni, S.; Pistidda, C.; Gosalawit-Utke, R.; Barkhordarian, G.; Rongeat, C.; Lindemann, I.; Gutfleisch, O.; Jensen, T. R.; Cerenius, Y.; Christensen, J.; Baró, M. D.; Bormann, R.; Klassen, T.; and Dornheim, M. Effect of Transition Metal Fluorides on the Sorption Properties and Reversible Formation of $\text{Ca}(\text{BH}_4)_2$. *J. Phys. Chem. C*, 115(5):2497–2504, 2011.
- Boothroyd, C. Quantification of high-resolution electron microscope images of amorphous carbon. *Ultramicroscopy*, 83(3–4):159–168, 2000.
- Boothroyd, C.; Kasama, T.; and Dunin-Borkowski, R. Comparison of approaches and artefacts in the measurement of detector modulation transfer functions. *Ultramicroscopy*, 129:18–29, 2013.
- Borgschulte, A.; Callini, E.; Probst, B.; Jain, A.; Kato, S.; Friedrichs, O.; Remhof, A.; Biemann, M.; Ramirez-Cuesta, A. J.; and Züttel, A. Impurity Gas Analysis of the Decomposition of Complex Hydrides. *J. Phys. Chem. C*, 115(34):17220–17226, 2011.
- Cahen, S.; Eymery, J.-B.; Janot, R.; and Tarascon, J.-M. Improvement of the LiBH_4 hydrogen desorption by inclusion into mesoporous carbons. *J. Power Sources*, 189(2): 902 – 908, 2009.
- Choi, Y.; Lu, J.; Sohn, H. Y.; Fang, Z.; Kim, C.; Bowman Jr., R. C.; and Hwang, S.-J. Reaction Mechanisms in the $\text{Li}_3\text{AlH}_6/\text{LiBH}_4$ and Al/LiBH_4 Systems for Reversible Hydrogen Storage. Part 2: Solid-State NMR Studies. *J. Phys. Chem. C*, 115(13):6048–6056, 2011.
- Christian, M. and Aguey-Zinsou, K. F. Destabilisation of complex hydrides through size effects. *Nanoscale*, 2:2587–90, 2010.

- Creemer, J. F.; Helveg, S.; Hoveling, G. H.; Ullmann, S.; Molenbroek, A. M.; Sarro, P. M.; and Zandbergen, H. W. Atomic-scale electron microscopy at ambient pressure. *Ultramicroscopy*, 108(9):993 – 998, 2008.
- Danaie, M.; Malac, M.; and Mitlin, D. Investigation of Beam Damage Mechanism of Ball-milled MgH₂ Powder. *Microsc. Microanal.*, 14:278–279, 2008.
- Danaie, M.; Tao, S.; Kalisvaart, P.; and Mitlin, D. Analysis of deformation twins and the partially dehydrogenated microstructure in nanocrystalline magnesium hydride (MgH₂) powder. *Acta Mater.*, 58(8):3162 – 3172, 2010.
- de Jonge, N.; Bigelow, W. C.; and Veith, G. M. Atmospheric Pressure Scanning Transmission Electron Microscopy. *Nano Lett.*, 10(3):1028–1031, 2010.
- de Jongh, P. E. and Adelhelm, P. Nanosizing and Nanoconfinement: New Strategies Towards Meeting Hydrogen Storage Goals. *ChemSusChem*, 3(12):1332–1348, 2010.
- DENS Solutions. Nano-Chip Sample Carriers, 2016.
<http://denssolutions.com/products/nano-chip/>.
- Deprez, E.; Justo, A.; Rojas, T.; López-Cartés, C.; Bonatto Minella, C.; Bösenberg, U.; Dornheim, M.; Bormann, R.; and Fernández, A. Microstructural study of the LiBH₄-MgH₂ reactive hydride composite with and without Ti-isopropoxide additive. *Acta Mater.*, 58(17):5683–5694, 2010.
- Doyle, P. A. and Turner, P. S. Relativistic Hartree–Fock X-ray and electron scattering factors. *Acta Crystallogr. Sect. A*, 24(3):390–397, 1968.
- Eastman, J. A.; Thompson, L. J.; and Kestel, B. J. Narrowing of the palladium-hydrogen miscibility gap in nanocrystalline palladium. *Phys. Rev. B*, 48:84–92, 1993.
- Egerton, R. F. *Electron Energy-Loss Spectroscopy in the Electron Microscope*. Plenum Press, New York, 2nd edition, 1989.
- Egerton, R. F. *Electron Energy-Loss Spectroscopy in the Electron Microscope*. Springer New York Dordrecht Heidelberg London, 3rd edition, 2011.
- Egerton, R. F.; Li, P.; and Malac, M. Radiation damage in the TEM and SEM. *Micron*, 35(6):399 – 409, 2004.
- Egerton, R.; Crozier, P.; and Rice, P. Electron energy-loss spectroscopy and chemical change. *Ultramicroscopy*, 23(3-4):305 – 312, 1987.

- Fechler, N.; Fellingner, T. P.; and Antonietti, M. "Salt templating": a simple and sustainable pathway toward highly porous functional carbons from ionic liquids. *Adv. Mater.*, 25: 75–9, 2013.
- Fedneva, E.; Alpatova, V.; and Mikheeva, V. *Russian J. Inorg. Chem.*, 9:341–343, 1964.
- Felderhoff, M.; Weidenthaler, C.; von Helmolt, R.; and Eberle, U. Hydrogen storage: the remaining scientific and technological challenges. *Phys. Chem. Chem. Phys.*, 9:2643–2653, 2007.
- Friedrichs, O.; Snáchez-López, J.; López-Cartes, C.; Dornheim, M.; Klassen, T.; Bormann, R.; and Fernández, A. Chemical and microstructural study of the oxygen passivation behaviour of nanocrystalline Mg and MgH₂. *Appl. Surf. Sci.*, 252(6):2334–2345, 2006.
- Friedrichs, O.; Remhof, A.; Borgschulte, A.; Buchter, F.; Orimo, S. I.; and Züttel, A. Breaking the passivation—the road to a solvent free borohydride synthesis. *Phys. Chem. Chem. Phys.*, 12:10919–10922, 2010.
- Friedrichs, O.; Remhof, A.; Hwang, S. J.; and Züttel, A. Role of Li₂B₁₂H₁₂ for the Formation and Decomposition of LiBH₄. *Chem. Mater.*, 22:3265–3268, 2010.
- Fujii, H.; Higuchi, K.; Yamamoto, K.; Kajioka, H.; Orimo, S.; and Toyama, K. Remarkable Hydrogen Storage, Structural and Optical Properties in Multi-layered Pd/Mg Thin Films. *Mater. Trans.*, 43(11):2721–2727, 2002.
- Gerchberg, R. and Saxton, W. A practical algorithm for the determination of the phase from image and diffraction plane pictures. *Optik*, 35:237–250, 1972.
- Gross, A. F.; Vajo, J. J.; Van Atta, S. L.; and Olson, G. L. Enhanced Hydrogen Storage Kinetics of LiBH₄ in Nanoporous Carbon Scaffolds. *J. Phys. Chem. C*, 112(14):5651–5657, 2008.
- Gross, R. and Marx, A. *Festkörperphysik*. Oldenbourg Verlag, 2012.
- Gutowska, A.; Li, L.; Shin, Y.; Wang, C. M.; Li, X. S.; Linehan, J. C.; Smith, R. S.; Kay, B. D.; Schmid, B.; Shaw, W.; Gutowski, M.; and Autrey, T. Nanoscaffold Mediates Hydrogen Release and the Reactivity of Ammonia Borane. *Angew. Chem. Int. Ed.*, 44 (23):3578–3582, 2005.
- Hansen, P.; Helveg, S.; and Datye, A. Atomic-Scale Imaging of Supported Metal Nanocluster Catalysts in the Working State. *Adv. Catal.*, 50:77–95, 2006.

- Hartmann, A. Elektronen-Energieverlustspektroskopie an Nanopartikeln im Transmissionselektronenmikroskop bei niedriger Anregungsenergie. Master thesis, TU Dresden, 2010.
- Herley, P. J. and Jones, W. Transmission Electron Microscopy of Beam-sensitive Metal Hydrides*. *Z. Phys. Chem.*, 147:147–159, 1986.
- Herley, P.; Jones, W.; and Vigeholm, B. Characterization of the whiskerlike products formed by hydriding magnesium metal powders. *J. Appl. Phys.*, 58(1):292–296, 1985.
- Höhne, G.; Hemminger, W.; and Flammersheim, H. *Differential Scanning Calorimetry*. Springer Berlin Heidelberg, 2013.
- House, S. D.; Liu, X.; Rockett, A. A.; Majzoub, E. H.; and Robertson, I. M. Characterization of the Dehydrogenation Process of LiBH_4 Confined in Nanoporous Carbon. *J. Phys. Chem. C*, 118(17):8843–8851, 2014.
- Hýtch, M. and Stobbs, W. Quantitative comparison of high resolution TEM images with image simulations. *Ultramicroscopy*, 53(3):191 – 203, 1994.
- Humphreys, C. J. The scattering of fast electrons by crystals. *Rep. Prog. Phys.*, 42(11):1825, 1979.
- Hwang, S.-J.; Bowman, R.; Reiter, J.; Rijssenbeek, J.; Soloveichik, G.; Zhao, J.-C.; Kabbour, H.; and Ahn, C. NMR Confirmation for Formation of $[\text{B}_{12}\text{H}_{12}]_2^-$ Complexes during Hydrogen Desorption from Metal Borohydrides. *J. Phys. Chem. C*, 112(9):3164–3169, 2008.
- Ikeda, K.; Muto, S.; Tatsumi, K.; Menjo, M.; Kato, S.; Biemann, M.; Züttel, A.; Jensen, C. M.; and Orimo, S. Dehydriding reaction of AlH_3 : in situ microscopic observations combined with thermal and surface analyses. *Nanotechnology*, 20(20):204004, 2009.
- Ishizuka, K. and Uyeda, N. A new theoretical and practical approach to the multislice method. *Acta Crystallogr. Sect. A*, 33(5):740–749, 1977.
- Jacobsen, N. *NMR Spectroscopy Explained: Simplified Theory, Applications and Examples for Organic Chemistry and Structural Biology*. Wiley, 2007.
- Jeon, K.-J.; Moon, H. R.; Ruminski, A. M.; Jiang, B.; Kisielowski, C.; Bardhan, R.; and Urban, J. J. Air-stable magnesium nanocomposites provide rapid and high-capacity hydrogen storage without using heavy-metal catalysts. *Nat. Mater.*, 10(4):286–290, 2011.

- Jia, C. L.; Lentzen, M.; and Urban, K. Atomic-Resolution Imaging of Oxygen in Perovskite Ceramics. *Science*, 299(5608):870–873, 2003.
- Jia, Y.; Sun, C.; Cheng, L.; Wahab, M. A.; Cui, J.; Zou, J.; Zhu, M.; and Yao, X. Destabilization of Mg-H bonding through nano-interfacial confinement by unsaturated carbon for hydrogen desorption from MgH₂. *Phys. Chem. Chem. Phys.*, 15(16):5814, 2013.
- Jia, Y.; Sun, C.; Shen, S.; Zou, J.; Mao, S. S.; and Yao, X. Combination of nanosizing and interfacial effect: Future perspective for designing Mg-based nanomaterials for hydrogen storage. *Renew. Sustainable Energy Rev.*, 44:289–303, 2015.
- Kilaas, R. *MacTempas User Manual*. Total Resolution, 20 Florida Ave., Berkeley, CA 94707, U.S.A., mactempasx version 2.3.20 edition, 2011.
- Kilaas, R. Total Resolution LLC, Software for High Resolution Electron Microscopy, 2016. <http://www.totalresolution.com/>.
- Kim, K. C.; Dai, B.; Johnson, J. K.; and Sholl, D. S. Assessing nanoparticle size effects on metal hydride thermodynamics using the Wulff construction. *Nanotechnology*, 20(20):204001, 2009.
- Kirkland, E. J. *Advanced Computing in Electron Microscopy*. Springer New York Dordrecht Heidelberg London, School of Applied and Engineering Physics, Cornell University, 212 Clark Hall, Ithaca, NY 14853, USA, second edition edition, 2010.
- Konarova, M.; Tanksale, A.; Norberto Beltramini, J.; and Qing Lu, G. Effects of nanoconfinement on the hydrogen desorption properties of MgH₂. *Nano Energy*, 2(1):98–104, 2013.
- Kostka, J.; Lohstroh, W.; Fichtner, M.; and Hahn, H. Diborane Release from LiBH₄/Silica-Gel Mixtures and the Effect of Additives. *J. Phys. Chem. C*, 111:14026–14029, 2007.
- Lai, Q.; Christian, M.; and Aguey-Zinsou, K.-F. Nanoconfinement of borohydrides in CuS hollow nanospheres: A new strategy compared to carbon nanotubes. *Int. J. Hydrogen Energ.*, 39(17):9339–9349, 2014.
- Lichte, H. Optimum focus for taking electron holograms. *Ultramicroscopy*, 38(1):13 – 22, 1991.
- Lindemann, I. *Synthese und Charakterisierung neuartiger, gemischter Tetrahydridoborate für die Wasserstoffspeicherung*. PhD thesis, TU Dresden, 2014.

- Lindemann, I.; Domènech-Ferrer, R.; Dunsch, L.; Filinchuk, Y.; Cerný, R.; H. Hagemann, H.; D'Anna, H.; Lawson Daku, L.; Schultz, L.; and Gutfleisch, O. $\text{Al}_3\text{Li}_4(\text{BH}_4)_{13}$: a complex double-cation borohydride with a new structure. *Chem. Eur. J.*, 16(29):8707–12, 2010.
- Liu, X.; Peaslee, D.; Jost, C. Z.; and Majzoub, E. H. Controlling the Decomposition Pathway of LiBH_4 via Confinement in Highly Ordered Nanoporous Carbon. *J. Phys. Chem. C*, 114:14036–14041, 2010.
- Liu, X.; Peaslee, D.; Jost, C. Z.; Baumann, T. F.; and Majzoub, E. H. Systematic Pore-Size Effects of Nanoconfinement of LiBH_4 : Elimination of Diborane Release and Tunable Behavior for Hydrogen Storage Applications. *Chem. Mater.*, 23:1331–1336, 2011.
- Makridis, S. S.; Gkanas, E. I.; Panagakos, G.; Kikkinides, E. S.; Stubos, A. K.; Wagener, P.; and Barcikowski, S. Polymer-stable magnesium nanocomposites prepared by laser ablation for efficient hydrogen storage. *Int. J. Hydrogen Energ.*, 38(26):11530 – 11535, 2013.
- Mason, J. *Multinuclear NMR*. Springer US, 1987.
- Mason, T. and Majzoub, E. H. Effects of a Carbon Surface Environment on the Decomposition Properties of Nanoparticle LiBH_4 : A First-Principles Study. *J. Phys. Chem. C*, 118:8852–8858, 2014.
- Matsuda, J.; Yoshida, K.; Sasaki, Y.; Uchiyama, N.; and Akiba, E. In situ observation on hydrogenation of Mg-Ni films using environmental transmission electron microscope with aberration correction. *Appl. Phys. Lett.*, 105(8):083903, 2014.
- Mauron, P.; Buchter, F.; Friedrichs, O.; Remhof, A.; Biemann, M.; Zwicky, C. N.; and Züttel, A. Stability and Reversibility of LiBH_4 . *J. Phys. Chem. B*, 112:906–910, 2008.
- Mooij, L. P.; Baldi, A.; Boelsma, C.; Shen, K.; Wagemaker, M.; Pivak, Y.; Schreuders, H.; Griessen, R.; and Dam, B. Interface Energy Controlled Thermodynamics of Nanoscale Metal Hydrides. *Adv. Energy Mater.*, 1(5):754–758, 2011.
- Mooij, L. and Dam, B. Nucleation and growth mechanisms of nano magnesium hydride from the hydrogen sorption kinetics. *Phys. Chem. Chem. Phys.*, 15(27):11501, 2013.
- Nakashima, P. N. H. and Johnson, A. W. S. Measuring the PSF from aperture images of arbitrary shape—an algorithm. *Ultramicroscopy*, 94(2):135 – 148, 2003.

- Ngene, P.; van Zwienen, M. R.; and de Jongh, P. E. Reversibility of the hydrogen desorption from LiBH_4 : a synergetic effect of nanoconfinement and Ni addition. *Chem. Commun. (Cambridge, U. K.)*, 46:8201–3, 2010.
- Nielsen, T. K.; Manickam, K.; Hirscher, M.; Besenbacher, F.; and Jensen, T. R. Confinement of MgH_2 Nanoclusters within Nanoporous Aerogel Scaffold Materials. *ACS Nano*, 3(11):3521–3528, 2009.
- Nogita, K.; Tran, X. Q.; Yamamoto, T.; Tanaka, E.; McDonald, S. D.; Gourlay, C. M.; Yasuda, K.; and Matsumura, S. Evidence of the hydrogen release mechanism in bulk MgH_2 . *Sci. Rep.*, 5:8450, 2015.
- Paik, B.; Jones, I.; Walton, A.; Mann, V.; Book, D.; and Harris, I. MgH_2 – Mg phase transformation driven by a high-energy electron beam: An in situ transmission electron microscopy study. *Philos. Mag. Lett.*, 90(1):1–7, 2010.
- Paskevicius, M.; Sheppard, D. A.; and Buckley, C. E. Thermodynamic Changes in Mechanochemically Synthesized Magnesium Hydride Nanoparticles. *J. Am. Chem. Soc.*, 132(14):5077–5083, 2010.
- Paskevicius, M.; Tian, H.-Y.; Sheppard, D. A.; Webb, C. J.; Pitt, M. P.; Gray, E. M.; Kirby, N. M.; and Buckley, C. E. Magnesium Hydride Formation within Carbon Aerogel. *J. Phys. Chem. C*, 115(5):1757–1766, 2011.
- Peng, L.-M.; Ren, G.; Dudap, S. L.; and Whelan, M. J. Debye Waller Factors and Absorptive Scattering Factors of Elemental Crystals. *Acta Crystallogr. Sect. A*, 52:456–470, 1996.
- Pitt, M. P.; Paskevicius, M.; Brown, D. H.; Sheppard, D. A.; and Buckley, C. E. Thermal Stability of $\text{Li}_2\text{B}_{12}\text{H}_{12}$ and its Role in the Decomposition of LiBH_4 . *J. Am. Chem. Soc.*, 135(18):6930–6941, 2013.
- Schober, T. and Chason, M. A CTEM AND HVEM STUDY OF HYDRIDE PRECIPITATION IN MAGNESIUM. In Veziroglu, T. N., editor, *Metal-Hydrogen Systems*, pages 177 – 184. Pergamon, 1982.
- Shao, H.; Chen, C.; Liu, T.; and Li, X. Phase, microstructure and hydrogen storage properties of Mg–Ni materials synthesized from metal nanoparticles. *Nanotechnology*, 25(13):135704, 2014.

- Shao, J.; Xiao, X.; Fan, X.; Huang, X.; Zhai, B.; Li, S.; Ge, H.; Wang, Q.; and Chen, L. Enhanced hydrogen storage capacity and reversibility of LiBH_4 nanoconfined in the densified zeolite-templated carbon with high mechanical stability. *Nano Energy*, 15:244–255, 2015.
- Slichter, C. *Principles of Magnetic Resonance*. Springer Series in Solid-State Sciences 1. Springer Berlin Heidelberg, 1990.
- Stetson, N., DOE office of energy efficiency and renewable energy (EERE). An overview of US DOE's activities for hydrogen fuel cell technologies, 2012. <http://ceramics.org/wp-content/uploads/2012/02/mcare12-hydrogen-fuel-cell-tech1.pdf>.
- STOE. STOE STADI P: Best Data Quality using Transmission-/Debye-Scherrer-Geometry, 2016. <https://www.stoe.com/wp-content/uploads/2014/03/Labnote-Powder-Transmission-Debye-Scherrer-Geometry.pdf>.
- Surrey, A.; Pohl, D.; Schultz, L.; and Rellinghaus, B. Quantitative Measurement of the Surface Self-Diffusion on Au Nanoparticles by Aberration-Corrected Transmission Electron Microscopy. *Nano Lett.*, 12(12):6071–6077, 2012.
- Surrey, A.; Bonatto Minella, C.; Fechler, N.; Antonietti, M.; Grafe, H.-J.; Schultz, L.; and Rellinghaus, B. Improved hydrogen storage properties of LiBH_4 via nanoconfinement in micro- and mesoporous aerogel-like carbon. *Int. J. Hydrogen Energ.*, 41(12):5540–5548, 2016.
- Surrey, A.; Nielsch, K.; and Rellinghaus, B. Comments on “Evidence of the hydrogen release mechanism in bulk MgH_2 ” by K. Nogita et al. *Nature Sci. Rep.*, 2016. accepted.
- Surrey, A.; Schultz, L.; and Rellinghaus, B. Electron beam induced dehydrogenation of MgH_2 studied by VEELS. *Adv. Struct. Chem. Imag.*, 2(1):1–9, 2016.
- Suzuki, M.; Yaguchi, T.; and Zhang, X. F. High-resolution environmental transmission electron microscopy: modeling and experimental verification. *Microscopy*, 62(4):437–450, 2013.
- Thust, A. *Probing the Nanoworld*. Forschungszentrum Jülich GmbH, 2007.
- Wagemans, R. W. P.; van Lenthe, J. H.; de Jongh, P. E.; van Dillen, A. J.; and de Jong, K. P. Hydrogen Storage in Magnesium Clusters: Quantum Chemical Study. *J. Am. Chem. Soc.*, 127(47):16675–16680, 2005.

- Wang, Z. New Developments in Transmission Electron Microscopy for Nanotechnology. *Advanced Materials*, 15(18):1497–1514, 2003.
- Welch, D. A.; Faller, R.; Evans, J. E.; and Browning, N. D. Simulating realistic imaging conditions for in situ liquid microscopy. *Ultramicroscopy*, 135:36 – 42, 2013.
- Williams, D. and Carter, C. *Transmission Electron Microscopy A Textbook for Materials Science*. Springer, 2009.
- Woehl, T.; Evans, J.; Arslan, I.; Ristenpart, W.; and Browning, N. Direct in Situ Determination of the Mechanisms Controlling Nanoparticle Nucleation and Growth. *ACS Nano*, 6(10):8599–8610, 2012.
- Wong-Foy, A.; Matzger, A.; and Yaghi, O. Exceptional H₂ Saturation Uptake in Microporous Metal-Organic Frameworks. *J. Am. Chem. Soc.*, 128(11):3494–3495, 2006.
- Yan, Y.; Remhof, A.; Hwang, S.-J.; Li, H.-W.; Mauron, P.; Orimo, S.-i.; and Züttel, A. Pressure and temperature dependence of the decomposition pathway of LiBH₄. *Phys. Chem. Chem. Phys.*, 14:6514–6519, 2012.
- Yang, S. J.; Rothe, R.; Kirchhecker, S.; Esposito, D.; Antonietti, M.; and Fechner, N. A sustainable synthesis alternative for IL-derived N-doped carbons: Bio-based-imidazolium compounds. *Carbon*, 94:641 – 645, 2015.
- Yokosawa, T.; Alan, T.; Pandraud, G.; Dam, B.; and Zandbergen, H. In-situ TEM on (de)hydrogenation of Pd at 0.5-4.5bar hydrogen pressure and 20-400°C. *Ultramicroscopy*, 112(1):47–52, 2012.
- Yoshida, H. and Takeda, S. Image formation in a transmission electron microscope equipped with an environmental cell: Single-walled carbon nanotubes in source gases. *Phys. Rev. B*, 72:195428, 2005.
- Zaluski, L.; Zaluska, A.; and Ström-Olsen, J. Nanocrystalline metal hydrides. *J. Alloys Compd.*, 253-254:70 – 79, 1997.
- Zaluzec, N. J.; Schober, T.; and Westlake, D. G. Application of EELS to the study of metal-hydrogen systems. In *Thirty-ninth annual EMSA meeting*, 1981.
- Zhang, S.; Gross, A. F.; Van Atta, S. L.; Lopez, M.; Liu, P.; Ahn, C. C.; Vajo, J. J.; and Jensen, C. M. The synthesis and hydrogen storage properties of a MgH₂ incorporated carbon aerogel scaffold. *Nanotechnology*, 20(20):204027, 2009.

Zhao-Karger, Z.; Hu, J.; Roth, A.; Wang, D.; Kubel, C.; Lohstroh, W.; and Fichtner, M. Altered thermodynamic and kinetic properties of MgH_2 infiltrated in microporous scaffold. *Chem. Commun.*, 46:8353–8355, 2010.

Züttel, A. Materials for hydrogen storage. *Mater. Today*, 6(9):24 – 33, 2003.

Züttel, A.; Wenger, P.; Rentsch, S.; Sudan, P.; Mauron, P.; and Emmenegger, C. LiBH_4 a new hydrogen storage material. *J. Power Sources*, 118:1–7, 2003.

Züttel, A.; Callini, E.; Kato, S.; and Atakli, Z. O. K. Storing Renewable Energy in the Hydrogen Cycle. *CHIMIA Int. J. Chem.*, 69(12):741–745, 2015.

Publications

Journal papers

1. **A. Surrey**, L. Schultz, and B. Rellinghaus: Multislice simulations for in-situ HRTEM studies of nanostructured magnesium hydride at ambient hydrogen pressure, *Ultra-microscopy* (2016), under review
2. **A. Surrey**, K. Nielsch, and B. Rellinghaus: Comments on “Evidence of the hydrogen release mechanism in bulk MgH₂” by K. Nogita et al., *Nature Scientific Reports* (2016), accepted
3. **A. Surrey**, L. Schultz, and B. Rellinghaus: Electron beam induced dehydrogenation of MgH₂ studied by VEELS, *Advanced Structural and Chemical Imaging* 2 (2016) Nr. 7
4. **A. Surrey**, C. Bonatto Minella, N. Fechler, M. Antonietti, H.-J. Grafe, L. Schultz, and B. Rellinghaus: Improved hydrogen storage properties of LiBH₄ via nanoconfinement in micro- and mesoporous aerogel-like carbon, *International Journal of Hydrogen Energy* 41 (2016) Nr. 12, S. 5540-5548
5. D. Keller, S. Buecheler, P. Reinhard, F. Pianezzi, D. Pohl, **A. Surrey**, B. Rellinghaus, R. Erni, and A.N. Tiwari: Local band gap measurements by VEELS of thin film solar cells, *Microscopy and Microanalysis* 20 (2014), S. 1246-1253
6. S. Schneider, **A. Surrey**, D. Pohl, L. Schultz, and B. Rellinghaus: Atomic surface diffusion on Pt nanoparticles quantified by high-resolution transmission electron microscopy, *Micron* 63 (2014), S. 52-56
7. V. Velasco, D. Pohl, **A. Surrey**, A. Bonatto-Minella, A. Hernando, P. Crespo, and B. Rellinghaus: On the stability of AuFe alloy nanoparticles, *Nanotechnology* 25 (2014) Nr. 21, S. 215703/1-8
8. D. Pohl, **A. Surrey**, L. Schultz, and B. Rellinghaus: The impact of oxygen on the morphology of gas-phase prepared Au nanoparticles, *Applied Physics Letters* 101 (2012) Nr. 26, S. 263105/1-5
9. **A. Surrey**, D. Pohl, L. Schultz, and B. Rellinghaus: Quantitative measurement of the surface self-diffusion on Au nanoparticles by aberration-corrected transmission electron microscopy, *Nano Letters* 12 (2012), S. 6071-6077

Invited Talks

1. **A. Surrey**, C. Bonatto Minella, N. Fechler, M. Antonietti, L. Schultz, and B. Rellinghaus: Nanocrystalline MgH_2 and nanoconfined LiBH_4 for solid state hydrogen storage, ANM2015 1st International conference on Hydrogen Energy, Aveiro/ Portugal, 20.7.15 (2015)
2. **A. Surrey**, D. Pohl, E. Mohn, L. Schultz, and B. Rellinghaus: Structural peculiarities at the surface of metallic nanoparticles, Edgar Luescher Seminar 2012, Klosters, 4.-11.2.12 (2012)
3. **A. Surrey**, D. Pohl, S. Schneider, L. Schultz, and B. Rellinghaus: Atomare Charakterisierung der Oberflaechen von Nanopartikeln mittels aberrationskorrigierter Transmissionselektronenmikroskopie, Institutsseminar am Institut fuer Strukturphysik, TU Dresden, 29.5.12 (2012)

Danksagung

Zunächst möchte ich mich bei Prof. Ludwig Schultz und Prof. Oliver Gutfleisch für die Erstellung des Erst- und Zweitgutachtens bedanken. Außerdem danke ich Prof. Ludwig Schultz und Prof. Kornelius Nielsch für die Anstellung am IFW und die Möglichkeit zu Promovieren. Desweiteren gilt mein besonderer Dank meinem Betreuer, Dr. Bernd Rellinghaus. Ohne die Hilfsbereitschaft vieler netter Kollegen am IFW Dresden und all der Kooperationspartner hätte diese Arbeit nicht entstehen können. In der Hoffnung niemanden zu vergessen, möchte ich jedem einzelnen namentlich danken: Prof. Markus Antonietti, Dr. Christian Bonatto Minella, Anja Bonatto Minella, Prof. Bernard Dam, Christine Damm, Dr. Nina Fechler, Bernhard Gebel, Dr. Lars Giebeler, Dr. Hans-Joachim Grafe, Efi Hadjixenophontos, Dr. Silke Hampel, Monika Herrich, Roar Kilaas, Dr. Inge Lindemann, Milena Martine, Dr. Lennard Mooij, Dr. Robert Niemann, Dr. Darius Pohl, Dr. Diana Pohl, Almut Pöhl, Jörg Pribbenow, Dr. Lars Röntzsch, Maryam Salimian, Max Schanner, Sebastian Schneider, Frank Schmidt, Tina Sturm, und Sebastian Wicht

Außerdem gilt mein Dank den Geldgebern: der Reiner Lemoine-Stiftung, der Graduiertenakademie der TU Dresden und dem IFW Dresden bzw. den deutschen Steuerzahlern.

Zu guter letzt möchte ich mich bei meiner Familie, Caroline und Aaron bedanken.

Versicherung

Hiermit versichere ich, Alexander Surrey, dass ich die vorliegende Arbeit ohne unzulässige Hilfe Dritter und ohne Benutzung anderer als der angegebenen Hilfsmittel angefertigt habe; die aus fremden Quellen direkt oder indirekt übernommenen Gedanken sind als solche kenntlich gemacht. Die Arbeit wurde bisher weder im Inland noch im Ausland in gleicher oder ähnlicher Form einer anderen Prüfungsbehörde vorgelegt.

Die Dissertation wurde am Leibniz Institut für Festkörper- und Werkstoffforschung unter der wissenschaftlichen Betreuung von Dr. Bernd Rellinghaus angefertigt.

Dresden, den 25. Juli 2016

Unterschrift